

ADVANCED SINGLE MOLECULE LOCALIZATION MICROSCOPY FOR IMAGING CELLULAR NUCLEI

Dissertation
(kumulativ)

zur Erlangung des akademischen Grades doctor rerum naturalium
(Dr. rer. nat)

vorgelegt dem Rat der Chemisch-Geowissenschaftlichen Fakultät der
Friedrich-Schiller-Universität Jena

von M.Sc. Shih-Ya Chen
geboren am 20.01.1989 in Keelung, Taiwan

Gutachter:

1. Prof. Rainer Heintzmann, Friedrich-Schiller-Universität Jena
2. Prof. Christoph Cremer, Ruprecht-Karls-Universität Heidelberg

Tag der Verteidigung: 10.06.2020

Abstract

Fluorescence microscopy is an essential tool for biological research to study subjects such as cellular functions, spatial organization, or protein interactions. For more than a century, it is known that the resolution of conventional optical microscopy is limited to about 200 nm based on the calculation of Ernst Abbe in 1873. This resolution limitation restricted the understanding of the structural organization for many biological researches.

In the late 20th century, several super-resolution microscopy methods were developed to resolve cellular structures beyond the resolution limit. In this PhD research, single molecule localization microscopy (SMLM) was used to image nuclear structures with a resolution down to several nanometers. The optical setup for SMLM is based on a standard optical design of a fluorescence microscope equipped with lasers. The concept of this method is to induce blinking of fluorophores in a sample, resulting in sparse isolated diffraction limited spots in the images. The position of these isolated molecules can be determined precisely and a super-resolution image can be obtained after accumulating all localized positions of the fluorophores. This high resolution microscopy method helps many biological studies to visualize protein interactions or to see the fine structure of organelles.

The scope of this PhD research is to develop a 3D SMLM microscope which can overcome several principle limitations in imaging nuclei in 3D. Firstly, one of the most common problems of a microscope is sample drift. It is especially critical for super-resolution microscopy, because a small sample drift may result in artefacts and can hamper the resolution. Secondly, another principle problem is that commonly used organic fluorophores are restricted in their photon budget. It is often observed that the chemical structure of fluorophores change after high laser irradiance resulting in photobleaching. Thirdly, for SMLM in particular, a carefully adjusted chemical environment in the sample is recommended to induce sufficiently blinking signals of the organic fluorophores in combination with an appropriate laser irradiance. However, such an imaging buffer can degrade over time and may not be suitable for long time imaging. The above-mentioned limitations motivated the further development of SMLM in a technical perspective during this PhD research.

In the following content of this thesis, Chapter 1 introduces fluorescence microscopy and the standard optical elements of a microscope system. However, a conventional fluorescence microscopy cannot resolve structures such as nucleosomes, the smallest unit of a nucleus, and the higher organization of the chromatin. The principle concept of SMLM is introduced and different approaches to induce blinking of fluorophores such as fluorescent

proteins and organic fluorophores are presented. For imaging nuclei, different DNA fluorophores are discussed depending on their labeling positions. SMLM method based on fluctuation-assisted binding-activated localization microscopy (fBALM) will be introduced, because of its fluorescence properties for achieving high localization precision of the detected molecules and low selectivity of DNA sequences. However, the blinking properties of commonly used organic fluorophores and the method based on fBALM are often limited to a special chemical environment. The imaging buffer can degrade over time and therefore such buffer dependency of blinking signals is inconvenient for a wide range of applications.

During this PhD research, several advanced methods were used to achieve imaging of nuclei in 3D. Since nuclei have a complex structure and are large in three dimensions up to several micrometers for mammalian cells, an image acquisition can take over an hour to acquire sufficient blinking signals for image reconstruction. Chapter 2 presents a drift correction method based on image registration of speckle patterns to correct sample drift with a precision of several nanometer. Since this method utilizes the back-scattered laser light from a cell, it depends on the intrinsic structure of a cell to define the position for the drift correction. Without modification of a standard SMLM optical setup, this drift correction method can be used for imaging over a long time. To demonstrate the drift correction for SMLM, a stack of images showing blinking DNA fluorophores based on the fBALM method was acquired. After drift correction, the visualization of nucleosome domain clusters of the nucleus in 3D was improved.

An advanced optical design of the microscope based on patterned illumination is presented in Chapter 3. This design utilizes a phase-only spatial light modulator (SLM) in combination with the Gerchberg-Saxton algorithm to define an arbitrary region of interest (ROI) for illumination to avoid early photobleaching in the sample. The phase-only SLM can redistribute the light with low power losses. The design can achieve high laser irradiance, because the total power in the sample is independent of the size of the illumination pattern, which is applicable for different SMLM applications. Additionally, the defined arbitrary regions of interest (ROI) have a nearly flat-top intensity profile, which can reduce artefacts due to inhomogeneous illumination and improves quantitative analysis. To demonstrate the patterned illumination technique for SMLM, cell nuclei were imaged based on the fBALM method. A fine structure of a nucleus such as chromatin protrusion was acquired. A density-based cluster analysis based on DBSCAN was used for quantitative analysis. The resulting clusters can help to visualize the nucleosome domain clusters.

However, the optimized imaging buffer based on the fBALM method has a pH-value of 3.7, which decreases over time, leading to difficulty for imaging a nucleus in 3D. In order

to avoid this restriction, Chapter 4 presents a graphene-based material (graphene molecule – GM or nanographene), which was discovered to blink in air and shows no significant blinking dependency of the blinking on different environments. These nanographenes have good blinking properties which are comparable with common fluorophores used in SMLM, but without the need of a special chemical composition of the imaging buffer. Correlative microscopy based on 3D SMLM and AFM was performed. A cover slip with small crevices was imaged to demonstrate a proof of principle experiment with nanographene for applications in material science. An experiment was performed by depositing nanographenes on a mild-etched cover slip. An image stack showing optical isolated nanographenes in a time series was recorded. Small cracks in the cover slip could be resolved after super-resolution image reconstruction. The imaging registration of the two high-resolution methods shows a good overlap of the crevices on the cover slip.

A nanographene with water-solvable ligands was investigated for its biocompatibility in fluorescence microscopy for the first time. An SMLM experiment was performed to demonstrate the blinking of nanographenes in cells without a special imaging buffer. Without significantly reducing the blinking signals, nanographenes in cells can be imaged for a long time. Therefore, they are suitable for imaging cell nuclei. The designed optical setup for SMLM experiments mentioned in this PhD research provides an important tool for imaging nuclei. With the help of nanographenes with blinking properties independent of the imaging buffer, 3D SMLM may be used to visualize the 3D structure of nuclei in the future.

The above-mentioned improvements during this PhD research includes a broad range of research subjects associated to SMLM techniques. These advanced developments are not only for imaging nuclei, but also applicable to applications in other biological researches and in material science.

Zusammenfassung

Die Fluoreszenzmikroskopie ist ein wesentliches Werkzeug für die biologische Forschung, um Themen wie z.B. zelluläre Funktionen, räumliche Organisation oder Proteininteraktionen zu untersuchen. Seit mehr als einem Jahrhundert ist bekannt, dass die Auflösung der konventionellen Lichtmikroskopie nach den Berechnungen von Ernst Abbe aus dem Jahr 1873 auf etwa 200 nm begrenzt ist. Diese Auflösungsgrenze schränkte das Verständnis der strukturellen Organisation von Zellen für viele biologische Fragestellungen ein.

Im späten 20. Jahrhundert wurden mehrere supraauflösende Mikroskopieverfahren entwickelt, um zelluläre Strukturen über die Auflösungsgrenze hinaus untersuchen zu können. In dieser Doktorarbeit wurde die Einzelmolekül-Lokalisationsmikroskopie (SMLM) eingesetzt, um Kernstrukturen mit einer Auflösung von wenigen Nanometern abzubilden. Das Konzept der Methode besteht darin, das Blinken von Fluorophoren in einer Probe zu induzieren, was zu räumlich isolierten beugungsbegrenzten Punkten in den Bildern führt. Die Positionen der einzelnen Punkten und damit die Position der Moleküle kann genau bestimmt werden und nach Akkumulation aller lokalisierten Positionen der Fluorophore kann ein hochauflösendes Bild erzeugt werden. Diese hochauflösende Mikroskopie-Methode ermöglicht vielen biologischen Studien, Proteininteraktionen zu visualisieren oder die Feinstruktur von Organellen sichtbar zu machen.

Ziel dieser Doktorarbeit ist die Entwicklung eines 3D-SMLM-Mikroskops, das mehrere prinzipielle Einschränkungen bei der Abbildung von Zellkernen in 3D überwinden kann. Eines der häufigsten Probleme stellt die Probendrift da. Sie ist besonders kritisch für die hochauflösende Mikroskopie, da eine kleine Probendrift zu Artefakten führen und die Auflösung beeinträchtigen kann. Ein weiteres prinzipielles Problem ist, dass häufig verwendete organische Fluorophore in ihrem Photonenbudget eingeschränkt sind. Durch die hohe Intensität der Laserstrahlung bei SMLM-Experimenten kann sich die chemische Struktur der Fluorophore ändern, was sich letztendlich als Photobleichen bemerkbar macht. Des Weiteren wird insbesondere bei SMLM eine sorgfältig angepasste chemische Umgebung in der Probe benötigt, um in Kombination mit einer hohen Laserintensität ausreichend Blinksignale der organischen Fluorophore zu induzieren. Ein solcher Imaging-Puffer kann jedoch im Laufe der Zeit abgebaut werden und ist daher möglicherweise nicht für eine Langzeit-Bildgebung geeignet. Die oben genannten Einschränkungen motivierten die Weiterentwicklung des SMLM aus technischer Sicht im Rahmen dieser Doktorarbeit.

Die Arbeit gliedert sich in folgende Abschnitte. In Kapitel 1 werden die Fluoreszenzmikroskopie und die optischen Standardelemente eines Mikroskopsystems vorgestellt. Da die herkömmliche Fluoreszenzmikroskopie jedoch keine Strukturen wie Nukleosomen, die kleinste Einheit des Zellkerngenomes, und die übergeordnete Organisation des Chromatins auflösen kann, wird im Anschluss das prinzipielle Konzept der SMLM vorgestellt und verschiedene Ansätze zur Induktion des Blinkens von fluoreszierenden Proteinen und organischen Fluorophoren vorgestellt. Für die Abbildung von Zellkernen werden verschiedene DNA-Fluorophore in Abhängigkeit von ihrer Markierungsposition vorgestellt. Eine SMLM-Methode, die auf der fluktuationsunterstützten bindungsaktivierten Lokalisationsmikroskopie (fBALM) basiert, wird erläutert, da sie aufgrund ihrer Fluoreszenzeigenschaften eine hohe Lokalisationspräzision der detektierten Moleküle und eine geringe Selektivität der DNA-Sequenzen erreicht. Auch hier kann sich der Imaging-Puffer im Laufe der Zeit abbauen, was für eine Reihe von Anwendungen ungünstig ist.

Während dieser Doktorarbeit wurden mehrere fortschrittliche Methoden eingesetzt, um Zellkerne in 3D abzubilden. Da Zellkerne eine komplexe Struktur aufweisen und bei Säugetierzellen in allen drei Dimensionen bis zu mehrere Mikrometern groß sind, kann die Bildaufnahme mehr als eine Stunde in Anspruch nehmen, um genügend Blinksignale für die Bildrekonstruktion zu erhalten. In Kapitel 2 wird eine Driftkorrekturmethode vorgestellt, die auf der Bildregistrierung von Speckle-Mustern basiert, um die Probendrift mit einer Präzision von wenigen Nanometern zu korrigieren. Da diese Methode rückgestreutes Laserlicht aus einer Zelle verwendet, hängt die Driftkorrektur von der intrinsischen Struktur der Zelle ab. Ohne Modifikation eines Standard-SMLM-Aufbaus kann diese Driftkorrekturmethode für Langzeitexperimente verwendet werden. In dieser Arbeit wird die Driftkorrekturmethode zur Verbesserung der Visualisierung von Nukleosomendomänen-Clustern eingesetzt.

Ein fortschrittliches optisches Design des Mikroskops, das auf frei einstellbarem Beleuchtungsmuster basiert, wird in Kapitel 3 vorgestellt. Das Design kann hohe Laserintensitäten erreichen und ist für verschiedene SMLM-Anwendungen einsetzbar. Zusätzlich erlaubt das Design des Mikroskops die Definition beliebiger Regionen von Interesse (ROI) für die Beleuchtung mit einem nahezu homogenen Intensitätsprofil, um ein frühzeitiges Bleichen der Fluorophore in der Probe zu vermeiden. Dieses Design kann Artefakte aufgrund inhomogener Beleuchtung reduzieren und verbessert die quantitative Analyse. In Aufnahmen des Zellkerns, die mit dieser Methode angefertigt wurden, werden Nukleosomendomänen-Cluster auf Basis einer dichte-basierten Clusteranalyse untersucht.

Der für die vorrangigen Experimente optimierte Puffer hat einen pH-Wert von 3,7 und wird mit der Zeit abgebaut. Dies führt zu Schwierigkeiten bei der Abbildung eines Nukleus in 3D, da ein optimales Blinken der Fluorophore nicht mehr gewährleistet ist. Um diese Einschränkung zu umgehen, wird in Kapitel 4 ein Graphen-basiertes Material (Graphen-Molekül - GM oder Nanographen) vorgestellt, das in Luft blinkt und keine signifikante Blinkabhängigkeit in verschiedenen Puffern zeigt. Die Blinkeigenschaften dieser Nanographene sind vergleichbar mit üblichen Fluorophoren, wie zum Beispiel Alexa 647, die in der SMLM verwendet werden, ohne dass eine spezielle chemische Zusammensetzung des Puffers erforderlich ist. Zum Nachweis des Prinzips wurden Experimente durchgeführt, bei denen das Nanographen auf einem mild-geätzten Deckglas aufgebracht wurde. Durch die Aufnahme von hochauflösenden Bildern mit isolierten Nanographen in Luft konnten kleine Risse im Deckglas aufgelöst werden. Obwohl derzeit noch kein synthetisiertes Nanographen zur Bindung an Biomoleküle für die Bildgebung von Zellkernen zur Verfügung steht, soll in einem ersten Schritt ein Nanographen mit wasserlöslichen Liganden in der Fluoreszenzmikroskopie auf seine Biokompatibilität untersucht werden. Ein „Proof of Principle“-Experiment wurde durch die Aufnahme eines großen Bildstapels mit Blinksignalen von wasserlöslichen Nanographen durchgeführt, um die Möglichkeit der Abbildung von Zellkernen zu demonstrieren.

Die oben genannten Verbesserungen während dieser Doktorarbeit umfassen ein weites Spektrum von Forschungsthemen, die mit der SMLM-Techniken verbunden sind. Diese Weiterentwicklungen sind nicht nur für die Abbildung von Zellkernen, sondern auch für Anwendungen in anderen biologischen Forschungen und in den Materialwissenschaften anwendbar.

Acknowledgements

I thank my family very much for their great support during these years. They supported me to pursue a PhD degree without any worries. I also thank my boyfriend who is always patient and has a very tolerant attitude towards every decision I made. My good friends Shruthi and Pelin supported me and shared our emotions to accomplish the PhD.

It was my pleasure to work in the super-resolution microscopy group leading by Prof. Christoph Cremer. His guidance provided many opportunities to work with people from different backgrounds. I would like to thank Prof. Rainer Heintzmann, who supported and supervised two cooperation projects in this PhD work. The PhD work could not be accomplished successfully without the help from the group members Dr. Márton Gelléri, Dr. Jan Neumann, Florian Schock, Renata Vaz Pandolfo, Dr. Maria Fernanda Contreras Gerenas, Johann von Hase, Felix Schreiber, Dr. Aleksander Szczurek, Dr. Wladimir Schaufler, the head of the light microscopy core facility Dr. Sandra Ritz and the former members Dr. Jonas Schwirz and Dr. Mária Hanulova.

I am very thankful for the kindly technical support from Dr. Felix Bestvater and the German Cancer Research Centre who borrowed us generously the spatial light modulator for the cooperation project of “Patterned illumination single molecule localization microscopy (piSMLM)”. It was my pleasure to work closely with Dr. Xiaomin Liu, Dr. Qiang Chen and Dr. Sachin Kumar and for our exciting scientific discussion. The cooperation project “nanographene” would not be successful without the support from Prof. Misha Bonn and Prof. Akimitsu Narita.

It was a great chance to work as a PhD student with the people at the Institute of Molecular Biology (IMB). I especially thank Dr. Ronald Wong, Rossana, and Vera, who were very kind to share and to help me preparing samples. We discussed many interesting research topics in biology. I also thank very much for the help from Markus, Dieter, Anke, Patricia, André, Manfred and Ralf at the electronic and the mechanic workshop of the institute for my special requests of mechanical elements and electronic boards for the microscope.

Content

Abstract	2
Zusammenfassung	5
Acknowledgements	8
Content	9
Chapter 1 Introduction	11
1.1. Fluorescence microscopy for biology	11
1.2. Standard blinking fluorophores	14
1.3. Blinking fluorophores for imaging cell nuclei	18
1.4. Resolution limit of fluorescence microscopy	21
1.5. Localization precision of a single light emitter	23
1.6. Single molecule localization microscopy (SMLM)	24
1.7. Optical setup for 3D SMLM	25
Chapter 2 Sample drift estimation method	29
2.1. Laser speckles	29
2.2. Scattered light from cells	30
2.3. Drift estimation method	31
2.4. Imaging nucleosome domain clusters	32
Chapter 3 Patterned illumination single molecule localization microscopy	34
3.1. Spatial light modulator (SLM)	34
3.2. Gerchberg-Saxton algorithm	35
3.3. Principle design of the illumination beam path	36
3.4. Optical setup for the patterned illumination	37
3.5. Homogeneous illumination	39
3.6. Imaging cell nuclei	42
3.7. Discussion of imaging nuclei based on fBALM	46
Chapter 4 Nanographenes for SMLM.....	48
4.1. Graphene and nanographene	48
4.2. Fluorescence properties of nanographenes	49
4.3. Blinking properties of nanographenes	50
4.4. Fluorescence recovery after UV irradiation	51
4.5. Correlative 3D SMLM and atomic force microscopy (AFM)	52
4.6. Water soluble nanographenes for bio-imaging	53
Chapter 5 Conclusion.....	56
Publication list.....	58

Publication 1	59
Publication 2	74
Publication 3	86
Selbständigkeitserklärung	109
Erklärungen.....	110
Reference	112

Chapter 1 Introduction

Fluorescence microscopy is a powerful technique for biological studies. Spatial organization of organelles or protein interactions can be visualized using a fluorescence microscope by targeting the biomolecules with fluorophores. Using fluorescent signals of the fluorophore as information, fluorescence microscopy can provide a high contrast, sensitivity, specificity and selectivity to image the targeted biomolecules. Nowadays, a number of fluorophores can be synthesized to label to a specific biomolecules for fluorescence imaging. Different chemical compounds were developed for different biological applications.

1.1. Fluorescence microscopy for biology

Light emission phenomena of natural materials, biological organelles or fluorophores involves a fluorescent molecule in different energy states [1]. Figure 1 shows the Jablonski diagram and presents the possible transitions of an electron between different energy levels of a molecule. Different time scales are involved in this transition process [2]. The electron transition starts with an electron excited by a photon from the ground state (S_0) to a higher energy level illustrated as S_1 and S_2 via absorption. Absorption takes time in the range of femtoseconds. The electron in the higher energy level can proceed a non-radiative transition such as internal conversion, or vibrational relaxation (S_2 to S_1) followed by a transition to a lower energy level (S_1 to S_0) by emitting a fluorescence photon. Fluorescence takes time scales between 10^{-7} s to 10^{-9} s.

It is also possible that the electron undergoes a non-radiative transition called intersystem crossing to the triplet state (S_1 to T_1), taking about 10^{-9} s to 10^{-12} s, followed by a transition to the ground states (T_1 to S_0) by emitting a photon, called phosphorescence. Typical time scale of phosphorescence is in the range of 10 s to 10^{-6} s. Most of the fluorescent molecules can repeat the transition process between the excitation and emission cycle many times.

Quenching describes a reversible process that leads to a decreased fluorescence intensity. An electron in an excited state can return to the ground state without emitting a photon. This process can be caused by e.g. energy transfer during a complex formation, internal conversion, or collision with some other molecules while the fluorophore is in the excited state. Once the molecule is in the ground state, the molecule can be excited again.

Bleaching is another possible electron transition process, but it is irreversible. Such a process leads to a permanent loss of fluorescence due to photon induced chemical damage or covalent modifications.

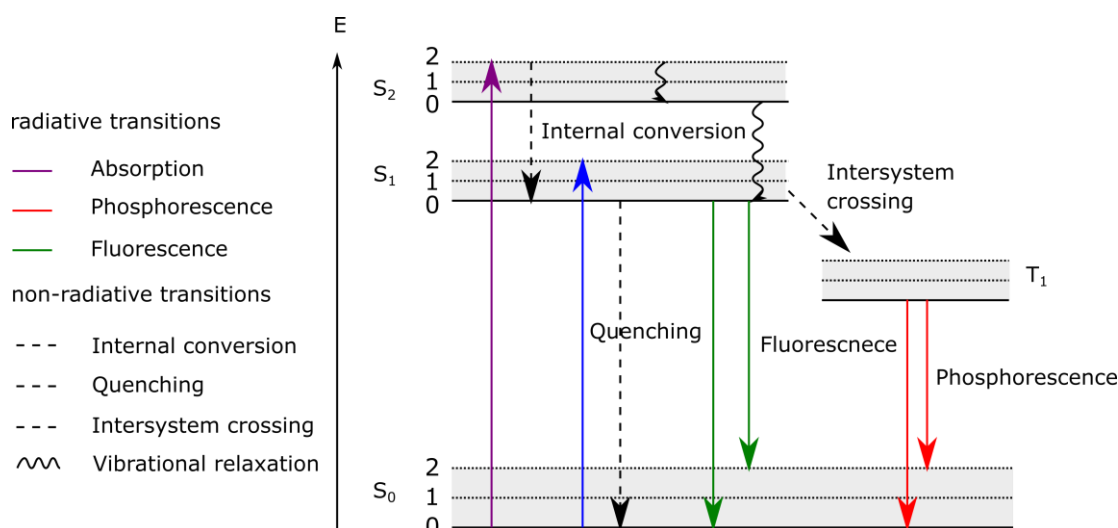


Figure 1 Jablonski energy diagram illustrating possible transitions between the electronic states of a molecule.

The fluorescence cycle described above involves always non-radiative transition. Thereby, the wavelength of the emitted photon is longer than the absorbed photon. The energy difference between the absorption photon (E_{out}) and emission photon (E_{in}) is defined as Stokes shift by Eq.1 [3].

$$\Delta E_{photon} = E_{out} - E_{in} = hc\left(\frac{1}{\lambda_{out}} - \frac{1}{\lambda_{in}}\right) \quad (1)$$

Fluorescence can be detected using a fluorescence microscope. As shown in Figure 2, the basic components include a light source with a broad wavelength range, a filter cube, an objective lens and a detector. An appropriate combination of the filters in the filter cube should be selected according to the fluorophores in the sample. The dichroic mirror is a specialized filter, which is designed to reflect efficiently the excitation wavelength. The position of the dichroic mirror is located after the excitation filter and is oriented 45 degrees with respect to the incident light. The fluorescence signal from the sample is transmitted through the emission filter and is detected by the detector.

As an example, the spectrum of the commonly used far-red organic fluorophore Alexa 647 and a suitable filter cube for this fluorophore is shown in Figure 3(A). Alexa 647 has a maximum excitation wavelength of 650 nm and an emission wavelength of 665 nm with a Stokes shift of 15 nm. The excitation and emission spectrum of the fluorophore can be well-separated using a filter cube with the transmission spectrum shown in Figure 3(B). The spectral range between 590 nm and 650 nm of the light is transmitted through the excitation filter which is chosen to excite optimally the fluorophore. The dichroic mirror is used to reflect the excitation wavelength from the light source and transmit the emission wavelength from the sample. The emission filter with the spectral range from 590 nm to 650 nm is utilized to filter

the remaining excitation wavelength of the light source in order to reduce the background induced by the excitation of the light.

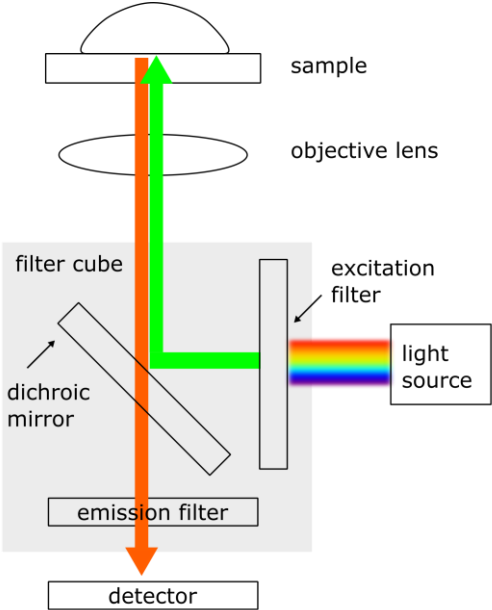


Figure 2 Schematic of a fluorescence microscope equipped with a light source with a wide spectrum, an objective lens, a filter cube and a detector.

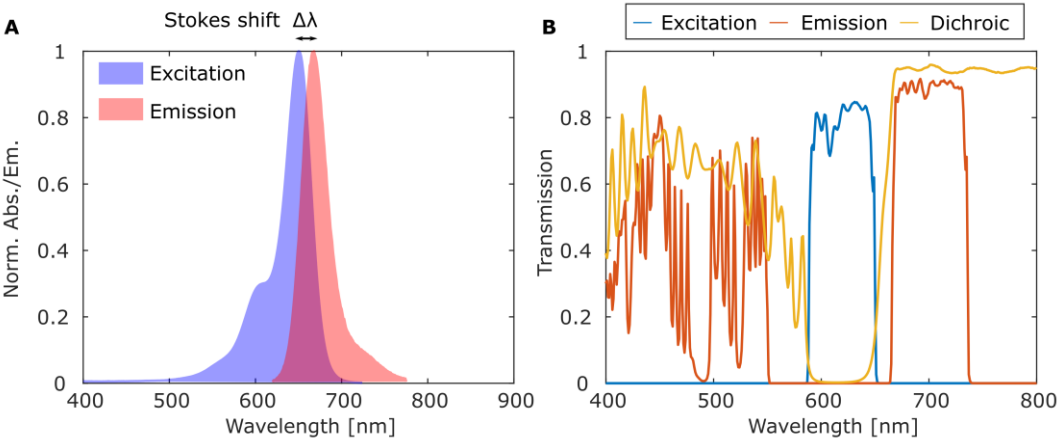


Figure 3 The spectrum of a commercial fluorophore and the suitable filters in the filter cube. (A) Excitation and emission spectrum of Alexa 647 [4]. (B) Spectrum of filters in a far-red filter cube (excitation: HQ620/60x, dichroic: Q660lp, emission: HQ700/75m) [5].

1.2. Standard blinking fluorophores

The photon emission of fluorescent molecules can be interrupted or the fluorescence properties can be altered, resulting in fluctuation of the fluorescent intensities in time. High emission intensity represents the fluorescence state (on-state), whereas low intensity represents the non-fluorescence state (off-state). Such intensity variations in time appear to be “blinking”. Different strategies to induce the blinking of fluorophores were discovered [6–12]. In the following, two mechanisms to generate blinking signals of the standard fluorophores are discussed.

(1) Fluorescent proteins

Fluorescent proteins (FPs) are small and can be genetically fused into target proteins and expressed in cell organelles or proteins. They are highly specific to the target protein and can avoid non-specific binding. For a stable cell line, FPs can achieve very high protein-labeling efficiency to nearly 100% [13]. To generate blinking signals of fluorescent proteins, special fluorescent proteins such as photoactivatable and photoconvertible fluorescent proteins can be used and are named Photoactivatable Fluorescent Protein (PA-FP). The spectral properties of such PA-FPs undergo a change upon irradiation with light of a specific wavelength [14,15].

Photoactivatable Green Fluorescent Protein (PA-GFP T203H) [14] is a variant of the wild-type green fluorescent protein, which is one of the early GFPs showing such a spectral shift upon irradiation. The absorption and emission spectrum of the native (purple) and the photoactivated (green) PA-GFP are shown in Figure 4(A). Solid lines indicate the absorption spectrum for both of the native and the photoactivated PA-GFP. The dashed line shows the emission spectrum of the native PA-GFP and after photoactivation. The peak of the absorption is at a wavelength of 400 nm and 504 nm for the native PA-GFP and for the photoactivated PA-GFP, respectively. The wavelength of 517 nm is the peak wavelength of the PA-GFP emission. After photo-activation, the fluorescence of PA-GFP is enhanced about 100 fold.

Kaede is another type of PA-FP, which undergoes photo-conversion after irradiation [16]. The spectrum of Kaede exhibits a spectral shift from green to red after irradiation. The absorption and emission spectrum of the native (green) and the photoconverted Kaede (red) are shown in Figure 4(B). For the native and the photoconverted Kaede, the absorption and emission spectrum are indicated with a solid line and a dashed line, respectively. The native Kaede has a peak of the absorption spectrum and a peak of the emission spectrum at a wavelength of 508 nm and 518 nm, respectively. It is noted that the spectrum of the photoconverted Kaede is well-separated from the spectrum of their native form. The peak of

the absorption spectrum and the emission spectrum of the photoconverted Kaede are at a wavelength of 572 nm and 580 nm, respectively. Additional to their photoconversion characteristic, a significant increase of the fluorescent emission can be realized in the photoconverted Kaede compared with the native one. After the photoconversion, fluorescence of Kaede is increased approximately 2000 fold in comparison with their native form.

The experiments to achieve blinking signals of the above mentioned PA-FPs can be performed using a pair of lasers in a fluorescent microscopy setup [6,8]. The choices of the wavelengths of the laser are according to the spectrum of the native PA-FP and the spectrum after the photoactivation and photoconversion. One laser works as the activation laser, which activates a sparse subset of FPs. The other laser used as the read out laser illuminates the activated FPs resulting in fluorescent signals. Because the probability of the activation of molecule is proportional to the intensity of the activation laser, by controlling the intensity and by short illumination pulses of the activation, single isolated blinking signals of fluorescent proteins can be obtained in a time series.

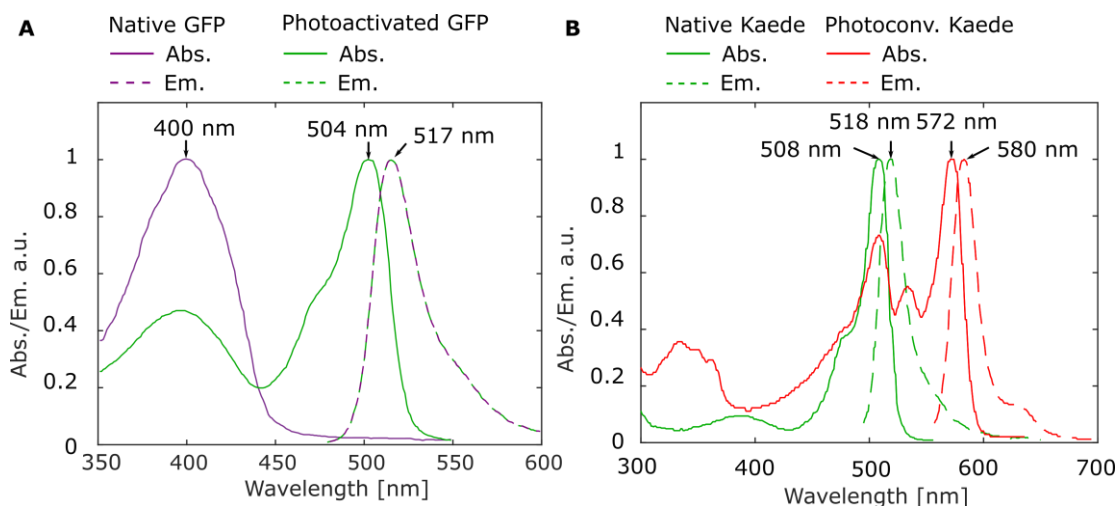


Figure 4 The absorption and emission spectrum of (A) a photoactivable green fluorescent protein (PA-GFP, T203H) [14] and (B) a photoconverted fluorescent protein (Kaede) [16].

(2) Organic fluorophore

Organic fluorophores such as cyanine and rhodamine derivatives are commonly used advanced fluorophores, which have been improved for fluorescent labeling, solubility in water, brightness and photostability [2]. They are versatile and provide a high specificity with biomolecules for different biological applications such as immunoglobulins (IgG, antibodies) [17].

One of the main strategies to achieve switching between on and off states is to design a special imaging buffer based on an oxygen-scavenging system in the presence of a primary thiol such as β -mercaptoethanol (BME) or β -mercaptoethylamine (MEA) in millimolar concentration [18–22]. This design of the buffer can prolong the time for fluorophores staying in the non-fluorescent state, following a stochastic recovery to the ground state by emitting a photon. Therefore, one of the keys to achieve blinking signals for organic fluorophores is to transfer the fluorophores to a relatively stable off-state at the beginning of the experiment by means of a high irradiance of several tens of kW/cm² [19].

Figure 5 shows the possible pathway of the energy transitions for the thiol-based photoswitching of Alexa fluorescent dyes. The energy transition can either occur in between its excited singlet state and the ground state by emitting a photon or it can undergo intersystem crossing. These two transitions are defined as the fluorescent state (ON-state). In the triplet state, a collision can occur between the molecular oxygen and the excited fluorophore [23]. Since the molecular oxygen can act as a quencher, it leads to the recovery of the singlet ground state by producing a singlet oxygen with the rate of k'_{isc} . Removing the oxygen using an oxygen scavenging buffer can keep the triplet state abundant to proceed further radical formation [19]. Thiolate can react with the fluorophore in the triplet state frequently with the rate k_{red} to form a radical anion of the fluorophore ($F^{\cdot-}$) and a corresponding thiyl radical. The radical anion of the fluorophore survives several seconds, resulting in a non-fluorescent state (OFF-state). The significant rate difference between the ON and the OFF state leads to optically isolated fluorescent signals in the image. The radical anion can be oxidized with the rate of k_{ox} back to the singlet ground state with the support of laser irradiance with a wavelength shorter than the excitation wavelength to close the cycle.

For some organic fluorophores in the presence of thiol, a significant change of the absorption spectrum after irradiation can be observed [24]. In the presence of 100 mM MEA, the absorption spectrum of Alexa 488 has a peak of the absorption spectrum at a wavelength of 488 nm. After laser irradiation of 488 nm for 5 minutes, the peak wavelength of the

absorption spectrum is reduced significantly, but an increase of the absorption at the wavelength of 396 nm can be obtained due to the formation of the radical anions of the Alexa 488. Therefore, it is possible to recover the radical anion of the fluorophores to the ground state by illuminating with a laser with a wavelength of 405 nm for a longer time period.

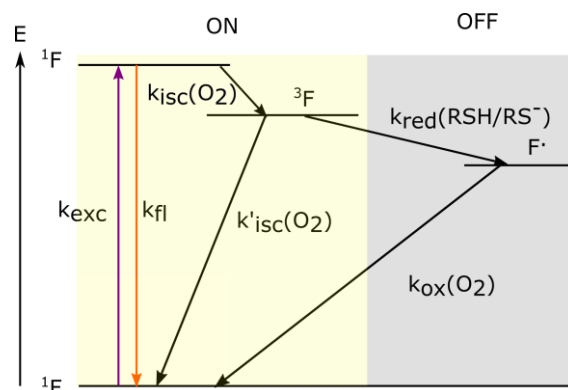


Figure 5 Reversible photoswitching mechanism of organic fluorophores in the presence of thiols. Jablonski diagram presents possible pathways for electron transitions.

To design a buffer to reduce oxygen, it is common to use a glucose oxidase catalase buffer based on enzymatic reactions, containing glucose, glucose oxidase and catalase. The glucose oxidase catalyzes the glucose to produce gluconic acid and hydrogen peroxide. Enzyme catalase is present to degrade the peroxide into water and oxygen [25]. As a side effect, the gluconic acid leads to a pH drop in the buffer and can change the experimental condition. Therefore, a sufficient buffering of the pH-value is necessary. To design such a buffer, an alternative oxygen-scavenger buffer can be prepared using a pyranose oxidase catalase. Pyranose oxidase in combination with catalase can be applied to maintain anaerobic conditions. The oxidation product of glucose is a ketone having a minimal effect on the pH-value [26].

The blinking mechanism is in reality much more complex than the mentioned energy scheme of the fluorophores, because the fluorophores in a biological sample have also chances to interfere with other molecules. An optimization process for individual fluorophores is suggested with a fine adjustment of the thiol concentration according to the sample [19,27,28]. Alternatively, using commercially available mounting media such as Vectashield H-1000 or ProlongGold can also achieve high resolution images, although the mechanism can not be explained due to the restriction of knowing their chemical compositions [29,30]. For multi-color imaging, the combination of fluorophores in the same imaging buffer is difficult and an individual optimization is highly recommended to achieve sufficient blinking signals.

1.3. Blinking fluorophores for imaging cell nuclei

The cell nucleus is one of the most important organelles regarding development and reproduction of eukaryotic cells. It contains deoxyribonucleic acid (DNA) molecules in a complex form with a large variety of proteins. The structure of DNA is a double helix determined by x-ray diffraction studies in 1953 [31]. Four nucleobases, Guanine (G), Cytosine (C), Thymine (T) and Adenine (A), can be paired by forming double or triple hydrogen bonds on the complementary bases of DNA. The pairs for the DNA bonding are the base pairs of DNA, which are G - C and A - T. The distance between adjacent pairs is 0.34 nm [32]. Figure 6(A) shows a simplified scheme of double stranded DNA (ds-DNA) structure illustrated with base pairs. The fundamental unit of the packaging form of DNA in a nucleus is a nucleosome, which contains two copies of histone proteins H2A, H2B, H3 and H4. About 146 base pairs (bp) are wrapped 1.65 times around the histones with additional 20 bp of DNA wrapped around the linker histone (H1). A single unit of the nucleosome is 11 nm in size [33], as illustrated in Figure 6(B). Nucleosomes are arranged like “beads on a string”, separated by a short segment of linker DNA accounting for the remaining 20 percent of genomic DNA [34]. Figure 6(C) shows such beads on a string of chromatin spread imaged with an electron microscope [35].

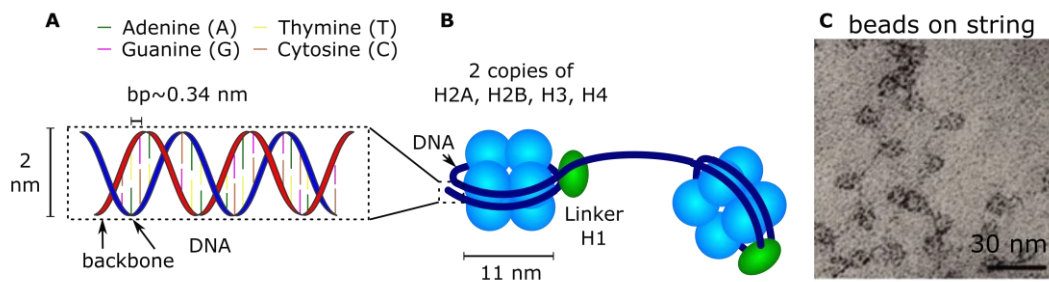


Figure 6 (A) The double stranded DNA with nucleobases A-T and G-C in pairs. (B) Two copies of histone proteins H2A, H2B, H3 and H4 and a linker protein H1 form the nucleosome of DNA in the nucleus. (C) Chromatin spread [35].

Hundred kilo base pairs (kb) of DNA to several mega base pairs (Mb) can fold into a higher complex formation of the chromatin structure [36,37]. To replicate the DNA for reproducing a nucleus, chromatin becomes condensed during mitosis to form compact metaphase chromosomes which are distributed to daughter nuclei. During interphase, most of the chromatin decondenses and appears to be distributed throughout the nucleus [38]. It is known that the chromosomes occupy distinct regions (“territories”) within the nucleus and are highly organized [39]. There may exist channels between chromatin regions, allowing the localization of active gene for transcription, replication and repair [40]. Fluorescence microscopy allows to visualize the dynamic activity of cell division and the structural organization in a cell nucleus [41]. Understanding the spatial organization of chromatin can

help to understand the gene regulation and the genome stability for diseases such as Alzheimer, senescence, cancer and ischemia [41–45].

Different nucleic acid stains were developed to label directly nucleic acids for visualizing the chromatin structures using a fluorescence microscope. The strategies to stain nucleic acid can be classified according to the locations, where the DNA fluorophore is bound. The four binding modes including minor groove, external binder, bis-intercalator and intercalator are shown in Figure 7.

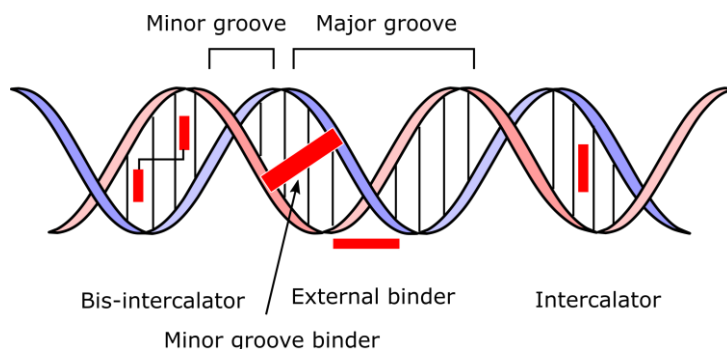


Figure 7 Classifications of labelling positions for nucleic acid stains with minor-groove binder, external binder, bis-intercalator and intercalator. The fluorophore positions are indicated in red.

Some important physical properties of the fluorophores are [46]:

- Specificity of binding to nucleic acids
- Fluorescence properties upon binding and unbinding to nucleic acids
- Quantum yield while binding and unbinding to nucleic acid

The fluorescence properties of the four commercialized DNA fluorophores Hoechst 33258, DAPI, YOYO-1 and SytoxOrange for labeling DNA are listed in Table 1.

Hoechst dye and DAPI dye are two classic minor groove binding dyes, which are widely used as membrane permeant or semi-permeant dyes [46]. They bind particularly to ademinethymine-rich (AT) regions of DNA [47,48]. Both of the dyes are blue fluorescent dyes, which can be excited by UV light and are suitable for multicolor imaging.

YOYO-1 is a monomethine cyanine dye emitting green fluorescence and generally considered as cell impermeant. The name of the dye is based on the basic chemical structure, which contains one carbon atom bridging the aromatic rings of an oxacyanine dye. There are multiple binding modes of YOYO-1 [46,49]. It is known that YOYO-1 acts primarily as a bis-intercalator at a dye-base-pairs ratio less than 1:1. As shown in Figure 7, each monomer unit

intercalates between base pairs and it can result in an unwinding of the double-helix structure. At a higher dye-to-base pair ratio, external binding begins to occur [50,51].

SytoxOrange is an intercalation fluorophore emitting orange fluorescence with a broad spectrum. It has a low selectivity in labeling between base pairs [52]. Although the chemical structure of SytoxOrange is not provided by the supplier, the references indicate the possibility of labeling SytoxOrange with a dye-to-base pair ratio of 1:1 [53,54], resulting in a high labeling efficiency to DNA structures in a nucleus.

Using an imaging buffer as shown in Section 1.2, Hoechst, DAPI and YOYO-1 can be switched between fluorescence on-state and off-state [55,56]. An alternative approach called binding-activated localization microscopy (BALM) or fluctuation-assisted binding-activated localization microscopy (fBALM) [57,58] was developed using the intercalation of nucleic acid fluorophores to induce the blinking signals. This method utilizes that the DNA dyes are non-fluorescent in aqueous solution, and fluorescence is enhanced while binding into the ds-DNA. The reversible cycle of ds-DNA between denaturation and renaturation can be used as a transient binding mechanism for intercalating fluorophores to bind and to unbind into the ds-DNA. Therefore, YOYO-1 and SytoxOrange can be used for BALM or fBALM, because their high fluorescence enhancement while binding into ds-DNA.

Figure 8 shows the scheme of the blinking mechanism based on the fBALM method using YOYO-1 in the bis-intercalation binding state [49]. When YOYO-1 binds to the ds-DNA, fluorescent signals are increased by a factor of 1000 and represent as the fluorescence on-state; when it unbounds from the DNA, YOYO-1 is in the non-fluorescent state with an intrinsically a low fluorescence and low quantum yield.

Table 1 Fluorescence properties upon binding to double stranded DNA of four nucleic acid dyes

	Peak of absorption/emission [nm]	Extinction coefficient [$\text{cm}^{-1} \text{m}^{-1}$]	Quantum yield	Fluorescence enhancement binding into dsDNA	Reference
Hoechst 33258	349/466	40,000	0.59	95x	[59,60]
DAPI	358/456	27,000	0.34	20x	[47,60]
YOYO-1	458/486	98,900	0.38	1000x	[60]
SytoxOrange	543/575	79,000	0.9	450x	[54,61]

To generate sufficient blinking signals of YOYO-1 for imaging the chromatin structures, a strategy is to utilize a moderately decrease of the pH-value over the course of a few hours to introduce local instabilities in the DNA structure. The optimal pH value of the imaging buffer was characterized around pH 3.7 [58]. Since YOYO-1 exhibits in fact multiple binding states, including the charge binding, the mono-intercalated and the bis-intercalated states [49,51], it is difficult to quantify DNA molecules corresponding to single molecule signal counting.

SytoxOrange can also be used for imaging nuclei based on the fBALM method which has comparable fluorescence properties like YOYO-1 [62]. It is nonfluorescent in aqueous conditions and has a fluorescence enhancement of up to 450 fold with a high quantum yield of 0.9 as shown in Table 1. Although the chemical structure of SytoxOrange is not provided by the supplier, the patent of the Sytox fluorophores and publications indicate a low selectivity to base pairs, which highlights the potential for specificity and a high labeling efficiency in ds-DNA with a base pair and dye ratio of 1:1 [53,54]. This shows the potential using SytoxOrange as an alternative DNA fluorophore to evaluate DNA molecules for the quantitative analysis, because of a low selective binding to base pairs. Therefore, SytoxOrange will be particularly used for imaging nuclei in the following experiments.

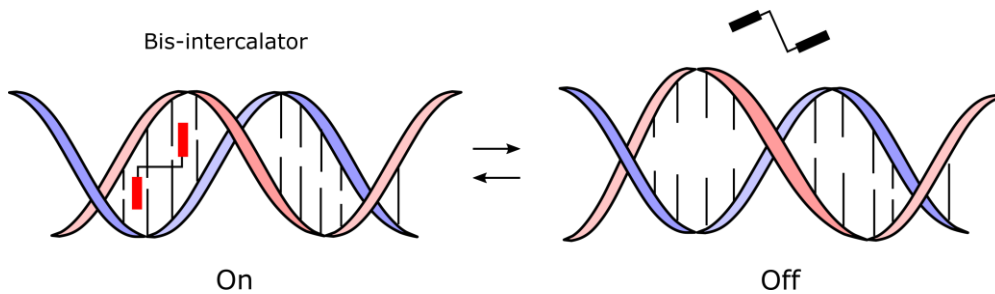


Figure 8 An illustration of blinking mechanism based on the fBALM method. When the bis-intercalator inserts in the ds-DNA, the dye is fluorescent (on-state); when the bis-intercalator is disassociated with the DNA, the fluorophore is non-fluorescent (off-state).

1.4. Resolution limit of fluorescence microscopy

The optical microscope was first invented by the Dutch inventor Antoni van Leeuwenhoek in the 18th century. In several centuries, the manufacturing technologies of optical elements were improved to achieve a better image quality with minimal aberrations. However, the resolution of an optical system was a fundamental limit caused by diffraction of light. For an optical microscope, this occurs when light propagates through the aperture of an objective lens. The fundamental law of the resolution limitation was described by Ernst Abbe in 1873 [63]. As shown in Eq.2, Abbe's formula, representing the diffraction limited spot with a radius of d , is related to the wavelength λ of the light, the refractive index of the medium n and the half angle of the opening angle θ .

$$d = \frac{\lambda}{2n\sin\theta} = \frac{\lambda}{2NA} \quad (2)$$

$n\sin\theta$ is the numerical aperture NA , which represents an important parameter of the objective lens for collecting photons from the sample. For fluorescence microscopy, the wavelength of the light is the emission wavelength of the fluorophores.

Point Spread Function (PSF) is the impulse response of the microscope to a point source. For a numerical approach to compute the theoretical PSF of a microscope, the equations derived by Born and Wolf are often used [64]. By defining the NA of the objective lens, the wavelength of light and the immersion oil, the theoretical PSF can be acquired using the ImageJ plugin PSF generator [65]. Figure 9 shows the PSF calculated using the PSF generator with the input value of $NA=1.4$ of the objective lens and $\lambda = 500 \text{ nm}$. It is assumed that scattering does not occur between the interface of the immersion oil and the objective lens. The Full Width of Half Maximum (FWHM) of the intensity distribution of the PSF is commonly used to define the size of the PSF. The FWHM of the simulated PSF at a wavelength of 500 nm is 184 nm in the lateral and 628 nm in the axial direction. When the NA of the objective lens is defined as 1.0, a larger PSF in both of the lateral and the axial directions is obtained, resulting in a FWHM of 258 nm in the lateral and 1237 nm in the axial direction.

The smallest separation distance between two point-like objects at which they can be distinguished, given by $d_{limit} = 0.61\lambda/NA$ according to Rayleigh [66]. Figure 10 shows the Rayleigh criterion in three different situations. (A) The molecules can be distinguished, when the two fluorescent molecules are separated in a distance larger than the limit ($d > d_{limit}$). (B) The minimal resolvable distance between the two fluorescent molecules is given by $d = d_{limit}$. (C) Two emitters cannot be distinguished when they are apart from each other smaller than the resolvable distance ($d < d_{limit}$).

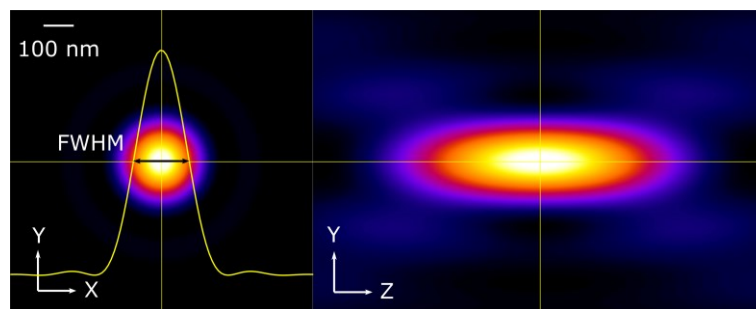


Figure 9 The simulation of a PSF based on the Born and Wolf module of the PSF-generator with $NA=1.4$ and $\lambda = 500 \text{ nm}$. The intensity distributions of the point spread function (PSF) in the x-y plane and the y-z plane.

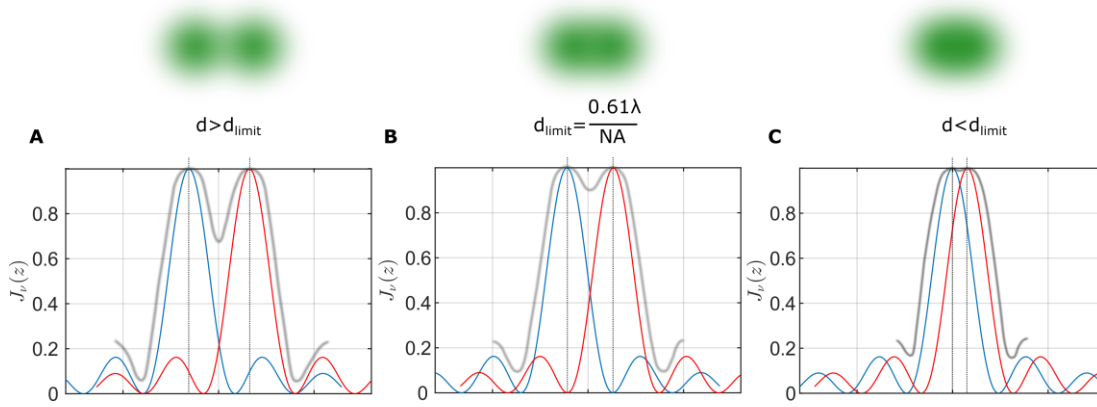


Figure 10 Illustration of the resolution limit criterion. Two single light emitters are separated in (A) a resolvable distance, (B) resolution-limited distance and (C) an unresolvable distance.

1.5. Localization precision of a single light emitter

A modern fluorescence microscope is often equipped with a digital device to detect photons from a fluorescent sample. Figure 11 shows the image of a single fluorescent molecule which is acquired using a digital camera. The fluorescent distribution of the single fluorescent molecule can be realized. Several particle tracking algorithm were developed to determine the position of individual fluorescent molecules with a sub-pixel accuracy below the diffraction limit [67–69].

In the digital image, it is common to fit the intensity distribution using a Gaussian function, because a Gaussian function is mathematically more tractable, and the width of the PSF after fitting shows little differences in practice between these two fitting methods [67].

The position of the molecule can be estimated using method such as Least Square (LS) or Maximum Likelihood Estimation (MLE) to determine the molecule position below the resolution limit [70,71]. The resulting localization precision σ of the fluorescent molecule is given by [67]:

$$\sigma^2 = \frac{s^2 + \frac{a^2}{12}}{N} + \frac{8\pi s^4 b^2}{a^2 N^2}, \quad (3)$$

where a corresponds to the camera pixel size, s is the standard deviation of a Gaussian function approximating the PSF, N is the number of photons, b is the background noise. When the background noise can be neglected compared to the fluorescent signals, a good approximation of the localization precision is [6]:

$$\sigma_{x,y} \approx \frac{s}{\sqrt{N}}. \quad (4)$$

An ideal case for the localization of an emitter with high precision is to have a high number of photons. In this case the estimated localization precision of 2 nm can be achieved using a fluorophore having a photon number of 10,000 [6]. However, in reality typical commercially available fluorophores can emit only a few hundred to a few thousand photons per molecule [15,72].

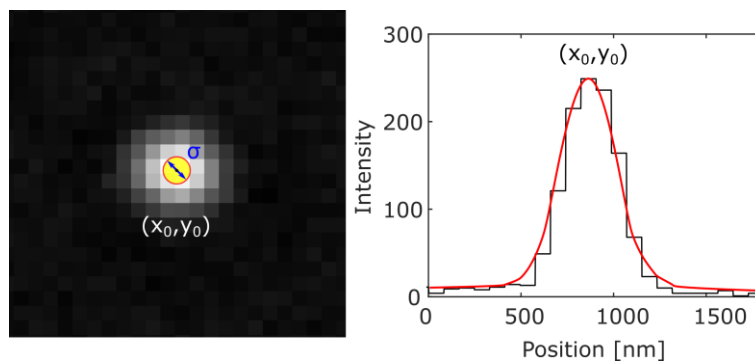


Figure 11 An illustration of the intensity fit of a single molecule image for determining the position (x_0, y_0) .

1.6. Single molecule localization microscopy (SMLM)

As discussed in Section 1.4 and 1.5, two molecules with a distance smaller than the resolution limit can not be distinguished using a fluorescence microscope. But the position of a single fluorescent molecule can be estimated better than the resolution limit.

The possibility to enhance resolution by localization microscopy was described initially in theoretical approaches [12,73,74]. It is assumed that single isolated molecules appear sparsely in images. Since the distance between the adjacent molecules is larger than the resolvable distance, the position of each molecule can be determined better than the resolution limit. The concept scheme is shown in Figure 12. (A) A small cellular structure (< 200 nm) is labeled with fluorophores indicated in green. (B) A time series of frames (1, 2, 3, ..., N) is acquired as an image stack, which each of the frame shows a sparse set of fluorophores in the on state indicated using green spots. (C) After determining the position of the fluorophore precisely and accumulating all the localized position, a high-resolved image of the biological target can be obtained. Although the concept was addressed already in the 1990s, the experimental approach was limited to switch fluorophores efficiently between on-and off-states in the biological samples. Blinking fluorophores as described in Section 1.2 and 1.3 were considered the key to achieve high resolution images. Therefore, this super-resolution microscopy method is named single molecule localization microscopy (SMLM) [6,9,12,22,30,73,75].

Several factors are considered important for practical implementation for SMLM [15,76]. For the sample, the biological structure should be highly or better fully labeled, because a high labeling efficiency can potentially fulfill the sampling theory according to the Nyquist-Shannon sampling theory [77], resulting in a better structural resolution in the reconstruction image. A high on- and off-switching rate can help to acquire an image stack in a reasonable time to detect enough single molecules [19]. It is also important to select a fluorophore with a high photon number, because the localization precision is generally dependent on the approximate inverse square root of the photon number detected per on-off cycle.

As shown in Figure 12, a large number of frames should be acquired to reveal the true structure of the biological target, which is dependent on the targeted biological structure. Because the image acquisition takes usually several minutes, this can lead to sample drift caused by slight temperature changes or a mechanical instability of the microscopy system. Consequently, a wrong position of the fluorescent molecules can be determined. For imaging nuclei, a simple drift correction method based on the speckle pattern of the cell was developed and will be discussed in Chapter 2. The detailed information can be found in [SC1].

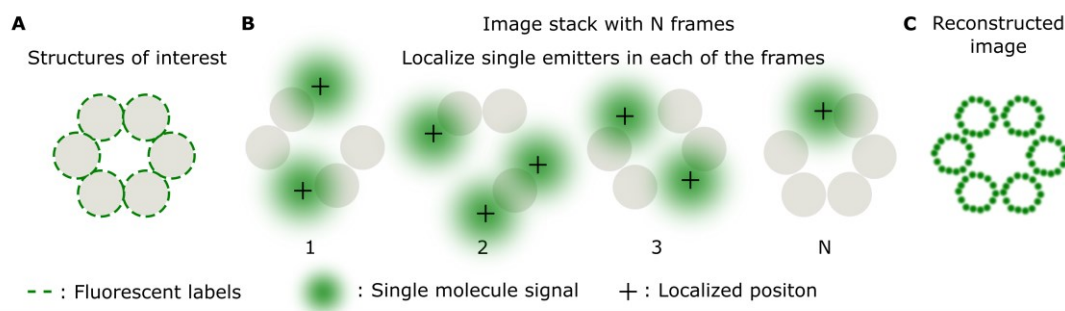


Figure 12 Schematic concept of single molecule localization microscopy (SMLM). (A) The structure of a biological target labelled with fluorophores. (B) A sparse set of fluorophores is in the fluorescent on-state per frame. At each frame, the distance between two adjacent fluorophore in the on-state is larger than the minimal resolvable distance. (C) A super-resolved structure of the biological target defined in A.

1.7. Optical setup for 3D SMLM

The classic design of an optical setup for SMLM experiments is to introduce lasers as a light source in the excitation beam path and a highly sensitive camera as the detector in the detection beam path of a fluorescence microscope [6,30,78]. The choice of the equipment is primarily dependent on the spectral properties of the fluorophores in the biological samples and the on-off switching condition of the buffer.

The standard design of the optical setup is shown in Figure 13. Three commonly used lasers with a wavelength of 488 nm, 561 nm and 647 nm were equipped in the optical setup. The laser with a wavelength of 488 nm indicates the excitation beam path. The orange emission from the beads sample shows the detection beam path in the optical setup of the microscope. The detailed description of the setup can be found in [SC1].

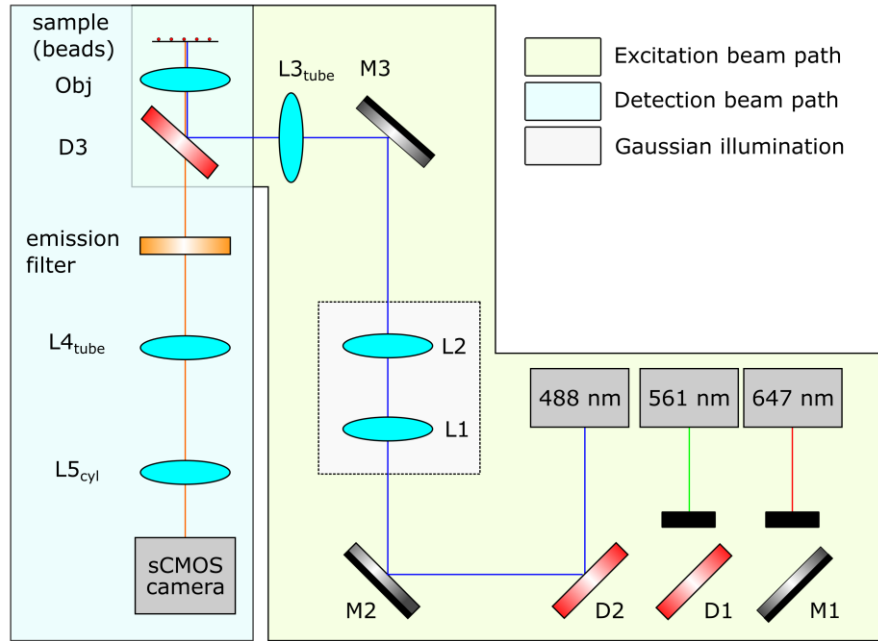


Figure 13 A standard design of an optical setup for SMLM. M1, M2 and M3 are mirrors, D1, D2, and D3 are dichroic mirrors. Obj., L1, L2, L3_{tube}, L4_{tube} and L5_{cyl} are lenses.

A telescope consisting of two lenses L1 and L2 was used to expand the laser beam. A tube lens L3_{tube} was utilized to focus the beam into the back focal plane of an objective lens with a NA of 1.47. The dichroic mirror (D3) reflected the expanded laser beam towards the objective lens. The objective lens was mounted in a nanometer positioning piezo stage to adjust the focal position. The illumination area in the sample had a Gaussian intensity profile with a FWHM of about 50 μm , resulting in an irradiance of up to 30 kWcm^{-2} in the sample. The area of the sample at the central position of the Gaussian beam has a higher irradiance than the area of the sample at the edge of the Gaussian beam. This can induce different localization density in the reconstructed image [79]. To improve the illumination profile in the sample, an advanced optical setup to illuminate the sample with a nearly flat-top illumination is presented in detail in [SC2] and in Chapter 3. Additionally, users can define the region of interests to prevent early photobleaching of the sample.

For the detection beam path, an emission filter is inserted into the detection beam path to filter the wavelength of the laser and allows the emission wavelength of the fluorophore to transmit through the optical system. A tube lens L4 is used to image the sample onto the camera.

By imaging fluorescent beads with a size of 100 nm, the width of the PSF was acquired. The theoretical values were calculated using an ImageJ plugin PSF generator using the vectorial-based model from Richard and Wolf [80,81]. The experimental results were evaluated using Huygens software by fitting the intensity distribution with a Gaussian function. Table 2 shows the theoretical results and the PSF measurements as a comparison. A slightly unsymmetrical PSF in x and y can be noted. Also a small difference between the theoretical results and the experimental results can be realized due to aberrations in the optical system or refractive indices mismatch.

Table 2 The FWHM of the theoretical size and the experimental size of the PSF.

emission	BP 525/30 (505-540)		BP600/50 (575-625)		LP 655	
	theory	measurement	theory	measurement	theory	measurement
x (nm)	210	252	230	266	270	286
y (nm)	210	264	230	273	270	302
z (nm)	440	683	550	685	600	662

For 3D SMLM, one of the methods to encode three dimensional information of individual fluorophores in 2D images is to insert a weak cylindrical lens $L5_{cyl}$ in the detection beam path [82,83]. This method introduces a defocus of the PSF and deforms the PSF from a circular shape to an elliptical shape based on astigmatism. Depending on the orientation of the elliptical shape of the PSF, it can be used to determine the axial location of the molecule. As shown in Figure 14, the vertical elongation of the PSF represents the position of the molecule above the focal plane (+Z); whereas, a horizontally elongated PSF is located below the focal plane (-Z). The width of the PSF increases gradually from the focal plane to an out of the focal plane. Therefore, one can calibrate the width w_x and w_y as a function of z by determining the width w_x and w_y of the PSF in different axial positions. The calibration function is described as [82]:

$$G(x, y) = h \cdot \exp\left(-2 \frac{(x-x_0)^2}{w_x^2} - 2 \frac{(y-y_0)^2}{w_y^2}\right) + b \quad (5)$$

where h is the peak height, b is the background, (x_0, y_0) is the center position of the peak, and w_x and w_y represent for the widths of the PSF in the x and y directions, respectively. The calibration of the PSF is essential and has to be characterized prior to blinking experiments. This is because the engineered PSF can be different between microscopy systems and between

different emission wavelengths. Similarly, other methods such as double-helix PSF, bi-plane and ZOLA can be used to deform the PSF in a different manner in order to encode the axial information in 2D images [84–86].

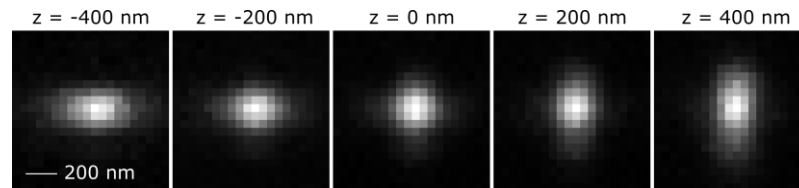


Figure 14 An example of the engineered PSF at the axial position of $z = -400$ nm, -200 nm, 0 nm, 200 nm and 400 nm. These images were acquired using the optical setup built in this PhD research as shown in Figure 13.

By fitting the width of the engineered PSF as a function of z using ThunderSTORM, an open-source ImageJ plug-in [87], the width of the fluorescent beads at the corresponding axial (z) position were obtained. The resulting calibration curves are shown in Figure 15. The standard deviation of the calibration curve are 7.0 nm and 8.2 nm in x and in y , respectively. For the other emission wavelengths, the same calibration procedure were applied to acquire the calibration curves.

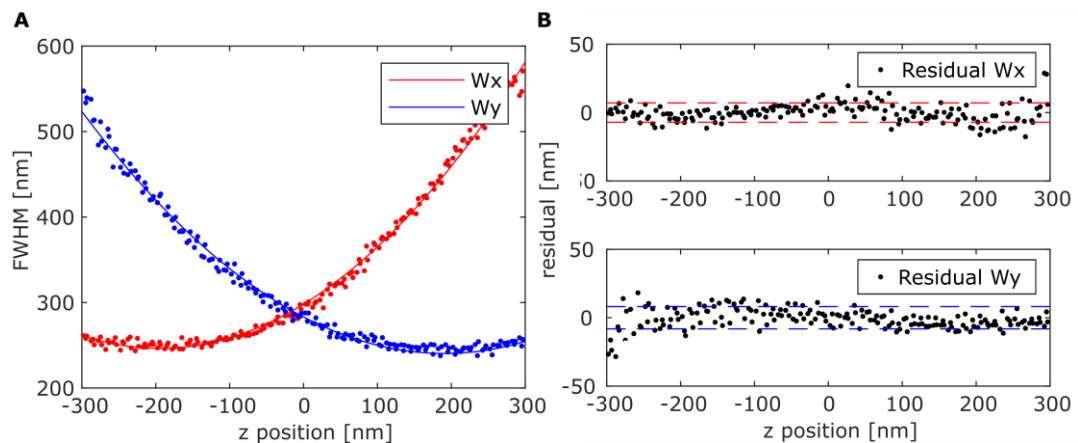


Figure 15 The calibration curves show the width W_x and W_y of the PSF in x and in y directions determined by the FWHM as a function of z . The data was acquired using the emission filter ET600/50.

Chapter 2 Sample drift estimation method

A high number of frames are needed to be acquired for the reconstruction of a super-resolution image and the imaging acquisition takes often several tens of minutes. However, sample drift during image acquisition due to temperature change or mechanical relaxation is not avoidable. This is especially critical for super-resolution imaging, because a small amount of drift in the microscope system can introduce blurring artifacts in the reconstructed image hampering resolution. Since a nucleus contains a highly complex structure, the image acquisition can take over an hour to acquire sufficient signals for reconstructing the 3D nucleus. In the following, a method based on the evaluation of speckle patterns formed by backscattered laser light from the cells for SMLM experiments to estimate drift will be presented.

2.1. Laser speckles

Speckle is an interference phenomenon observed when a coherent light source illuminates an object such as a white wall or a diffuser. Figure 16 shows schematic optical paths to illustrate speckle formation. A coherent light source such as a laser is used to illuminate a rough surface containing microscopic structures. Each small unit on the macroscopic surface can be regarded as new light sources. Each light wavelet travels with different optical path lengths. This leads to a different degree of interference and appears in a variation of the intensity distribution on a detector. Such a complex intensity pattern are called speckle pattern [88].

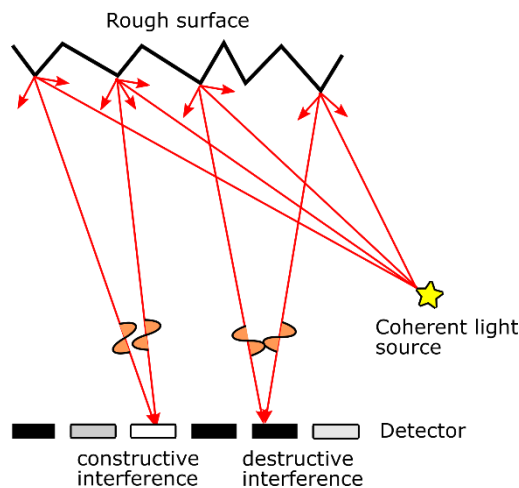


Figure 16 Schematic of laser speckles formation. A coherent light source illuminates a rough surface and the light is scattered in different directions. After light propagation, the wavelets can constructively or destructively interfere on the pixelated detector.

2.2. Scattered light from cells

Such speckle patterns can also be seen when a laser illuminates cellular structures using a standard microscope for SMLM. Figure 17 illustrates the scattering light from a cell in all directions. A laser illuminates a fiber-like organelle, representing a scatterer in the cell. For simplicity, only forward and backward scattered light is shown in Figure 17. Because cellular organelles have typically a size larger than the laser wavelength, scattering is describe by Mie-scattering, which is known to be only weakly dependent on the wavelength [89]. Diffraction at the edges of the cell organelles and refraction due to different relative indices between the cell and the medium can result in such light-scattering [90].

Using the optical setup of SMLM as shown in Figure 13, the interference of the back-scattered light from a cell can be acquired in the camera. Strong intensity variations can be seen. An example image showing a speckle pattern of a cell is shown in Figure 18. The ROIs at different axial positions ($z = -2 \mu\text{m}$, $z = -1 \mu\text{m}$, $z = 0 \mu\text{m}$, $z = 1 \mu\text{m}$) reveal different features in the speckle pattern. As indicated by a red circle, a near-diffraction limited spot is located in the center at $z = -2 \mu\text{m}$ and the position of the spot slightly shifts at $z = -1 \mu\text{m}$. At $z = 0 \mu\text{m}$ and $z = 1 \mu\text{m}$, the spot completely vanishes. Outside of the circle, different speckle patterns can be realized in different axial positions. Dependent on the morphology of the cells, the intensity pattern differ strongly [90]. Therefore, the structural differences of the intensity of the speckle patterns can be used to determine the position of the cell in three dimensions.

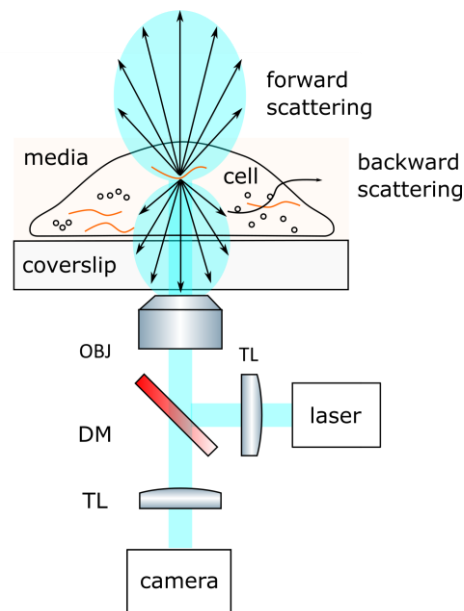


Figure 17 A schematic microscope setup for imaging speckle patterns of cells. (OBJ: objective lens, TL: tube lens, DM: dichroic mirror.)

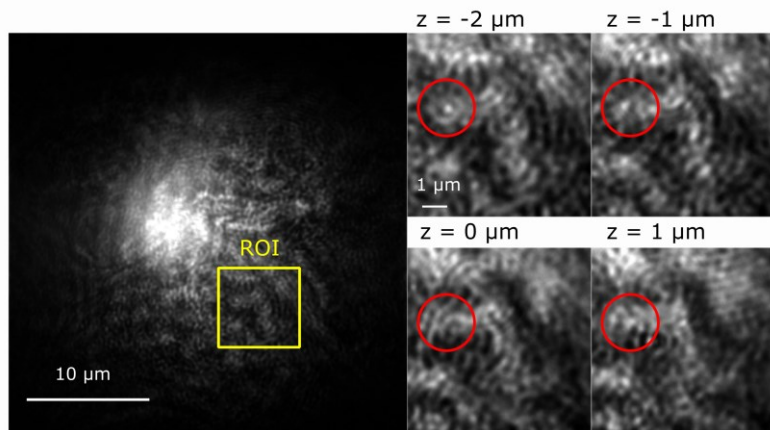


Figure 18 Speckle pattern of a cell sample. The insets show the ROI at four axial positions ($z = -2 \mu\text{m}$, $-1 \mu\text{m}$, $0 \mu\text{m}$ and $1 \mu\text{m}$). A speckle feature is highlighted by a red circle. Reprinted with permission from [SC1] ©The Optical Society.

2.3. Drift estimation method

Since each cell exhibits a unique speckle pattern and the speckle patterns vary continuously in z , a speckle reference z -stack f with n frames with a separation of Δz is acquired at the beginning of the measurement (t_0), where z is the axial position of each speckle frame. Figure 19 shows the scheme of the drift correction method. For drift estimation, single drift estimation frames g were acquired separated in time by Δt . Users can define the time separation for their SMLM experiment. Each of these images g show a speckle pattern closely corresponding to one present in the speckle reference stack f . Using the DFT method according to [91], the position of the sample drift at each sub-period (Δt) of the SMLM experiment can be analyzed. Detailed information about the computation process is presented in the original work [SC1].

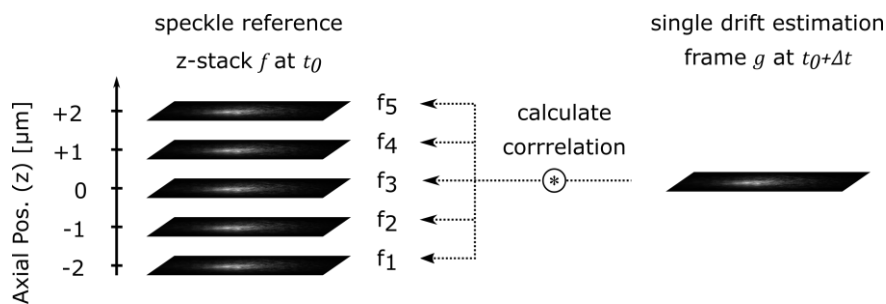


Figure 19 Scheme for drift estimation. A z -stack of speckle patterns f as a position reference of the cell is acquired. Single drift estimation frames g are captured at regular time intervals during the experiment. Reprinted with permission from [SC1] ©The Optical Society.

This method is particularly useful for imaging cell nuclei. One of the important advantages is that this method does not require additional sample preparation and photobleaching does not need to be considered. Another advantage is that a larger drift could be possibly determined, since the position information is defined in the reference stack. Using DFT image registration,

speckle images can be correlated with the reference z-stack and the three dimensional drift can be determined. A proof of principle experiment is shown in Figure 20. (A) A large drift with several micrometers was simulated and the results of the drift estimation are presented. A high accuracy with a standard deviation of 2 nm was obtained as shown in (B).

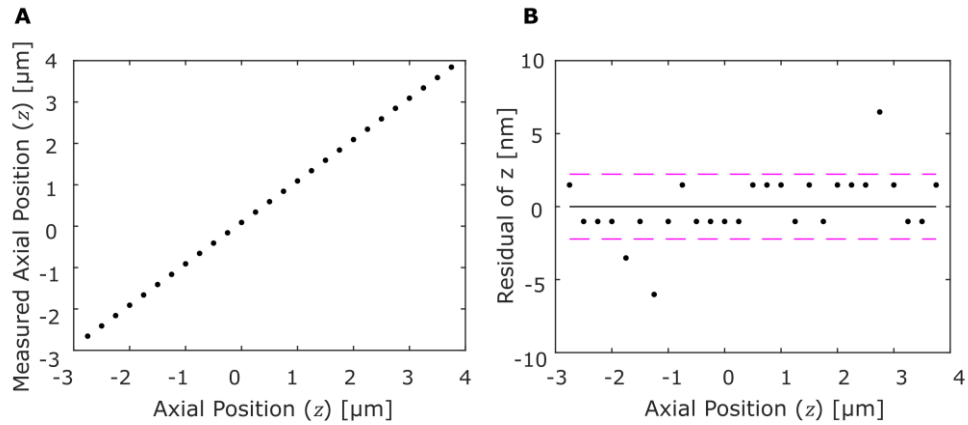


Figure 20 Speckle based z-position estimation by a defined z-position in a range of 7 μm and a step size of 250 nm. (a) Measured z-position. (b) Residuals of the linear regression. Reprinted with permission from [SC1] ©The Optical Society.

2.4. Imaging nucleosome domain clusters

To demonstrate the ability of the speckle-based drift correction method for the improvement of the imaging quality of cell nuclei, the fBALM method was performed and the speckle based drift correction method was used to correct the position of the localized DNA fluorophores. More detailed procedure of the correction can be found in [SC1].

Figure 21 shows the widefield image and the super-resolution image of a nucleus acquired based on the fBALM method. A ROI of the super-resolution image is selected to compare the super-resolution images before and after drift correction. Several nucleosome domain clusters can be seen in the three-dimensional image indicated using a color-coded z-projection. In comparison to the super-resolution image before drift correction, the super-resolution image after drift correction reveals a more confined nucleosome domain cluster. The z extension of the cluster was reduced by 150 nm. Detailed information can be found in [SC1]. The true 3D structure of the nucleus can be revealed with the help of drift correction, resulting in a better quantification.

The detected single molecule signals (SM) represents DNA locations inside the nucleus, which can be used to analyze the nuclear architecture. In the following demonstration 10,000 frames were acquired inside the nucleus, resulting in 189,209 SMs in an area of 209.5 μm^2 . In the small ROI shown in Figure 21 with an area of 5.0 μm^2 , a nucleosome domain cluster

consisting of 810 SMs was detected. By acquiring a higher number of frames, a larger number of signals can be detected assuming constant blinking signals during the image acquisition. By improving the statistic analysis, the true structure of the nucleus can be possibly revealed.

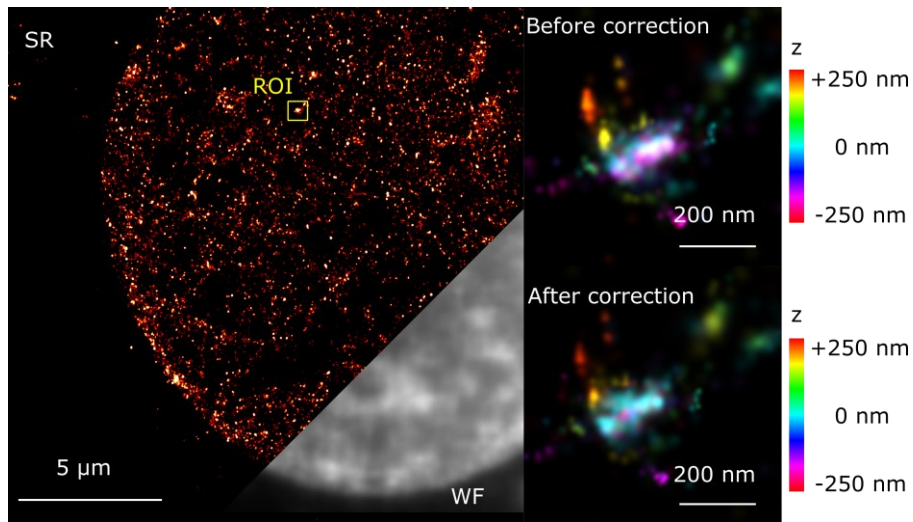


Figure 21 The intensity sum projection of the drift corrected 3D SMLM image of a nucleus labelled with the DNA dye SytoxOrange. Inset: A super-resolution image comparison of a nucleosome domain cluster shown in the centre of the ROI before correction and after correction. The colours indicates the z position using a colour-coded maximum intensity projection. Reprinted with permission from [SC1] ©The Optical Society.

Chapter 3 Patterned illumination single molecule localization microscopy

High laser irradiation is commonly used to illuminate a sample in SMLM experiments. However, commercial fluorophores are limited in their photon budget and high laser illumination can induce photodamage of the fluorophores. In order to avoid unnecessary illumination of the sample, an advanced optical design of SMLM was developed. This design allows the users to define arbitrary regions of interest for illumination. Additionally, the design facilitates a homogeneous illumination of the sample for a better quantitative analysis of the nucleosome domain clusters in a nucleus. In the following chapter, the optical design will be introduced and a proof of principle experiment is demonstrated by imaging a cell nucleus.

3.1. Spatial light modulator (SLM)

An Liquid Crystal on Silicon (LCoS) spatial light modulator (SLM) is a display, in which a thin layer of liquid crystals (LC) is sandwiched between a top sheet of glass coated with a transparent electrode (ITO layer) and a pixelated silicon substrate made by a complementary metal-oxide semiconductor (CMOS) panel [92]. The schematic of a reflective LCoS SLM is shown in Figure 22 [93]. Since LC is a birefringent material, the birefringence Δn of LCs is defined by [94]

$$\Delta n = n_e - n_o, \quad (6)$$

where n_o and n_e are the ordinary refractive index and the extraordinary refractive index, respectively.

When an external electric field is applied, for example, by applying a voltage to the pixels of the LCoS panel, LC molecules can be re-orientated. For a parallel-aligned nematic LC SLM, the LC molecules rotate along the axis perpendicular to both the light propagation direction and the polarization direction, while the voltage is applied. Therefore, the effective refractive index Δn_{eff} changes accordingly. Subsequently, the optical path length is changed, whereas the polarization state remains unaffected, resulting in a modulation of the phase retardation [95]. The phase retardation of light is given by [94]

$$\delta = 2\pi\Delta n_{eff}d/\lambda, \quad (7)$$

where d is the thickness of the LC layer and λ is the wavelength of the incident light. Since the light travels two times through the LCs, the phase retardation is rewritten by

$$\delta = 2\pi\Delta n_{eff}2d/\lambda. \quad (8)$$

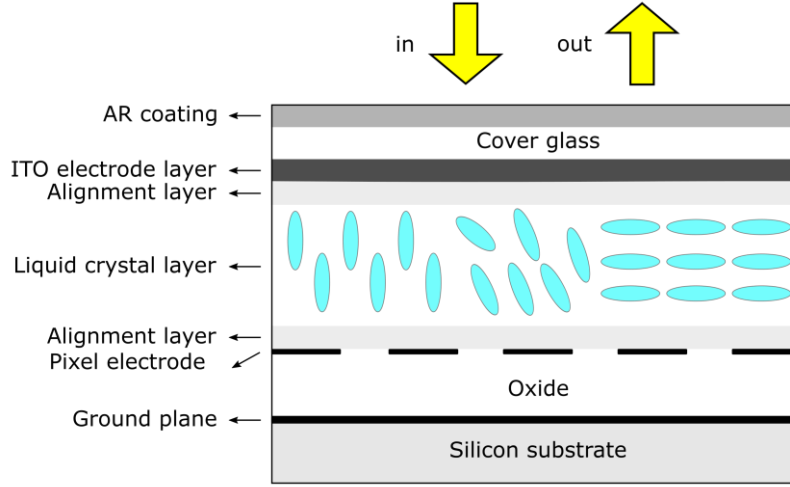


Figure 22 Schematic configuration of a LCoS SLM presented in the side view.

3.2. Gerchberg-Saxton algorithm

Gerchberg-Saxton (GS) algorithm is an iterative algorithm for retrieving the phase of the target intensity of light based on Fourier transformation [96]. The scheme of the algorithm is shown in Figure 23. The iterative process can be explained by the following Pseudo code:

```

 $\psi_1 = A_s e^{i\varphi_1}$ 
while (error > threshold)

     $\psi_2 = \text{FT}(\psi_1)$ 
     $\varphi_3 = \text{phase}(\psi_2)$ 
     $\psi_3 = A_T e^{i\varphi_3}$ 
     $\psi_4 = \text{IFT}(\psi_3)$ 
     $\varphi_4 = \text{phase}(\psi_4)$ 
     $\psi_1 = A_s e^{i\varphi_4}$ 

end
 $\varphi_4$  is displayed on the SLM

```

where ψ : wave function, A: amplitude, φ : phase, FT: Fourier transformation, IFT: inverse Fourier transformation. A_s : source amplitude, A_T : target amplitude. φ_1 is 0 in the GS algorithm.

The disadvantage of the GS algorithm is the appearance of laser speckles because of destructive interference between adjacent sampling points, resulting in strong intensity variations in the desired intensity pattern. Another disadvantage of this algorithm is that the

source intensity must be known in advanced. Without knowing the source intensity, the target intensity pattern can not be calculated correctly.

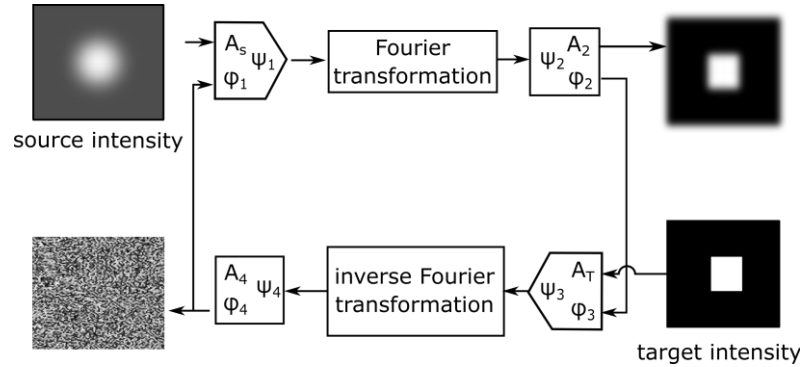


Figure 23 Scheme of the Gerchberg Saxton Algorithm for phase calculation of a target intensity.

3.3. Principle design of the illumination beam path

To design a patterned illumination beam path using a LCoS SLM, a simplified scheme is shown in Figure 24. The laser was expanded by a pair of lenses to match the size of the LCoS SLM. The polarization state of the expanded beam was aligned by a $\lambda/2$ waveplate to match the modulation axis of the liquid crystal layer of the SLM. The phase distribution of the desired intensity pattern was calculated using the GS algorithm. However, the presence of the zeroth order of unshaped diffracted light reflected by the SLM is a common problem seen in SLM systems, resulting in a bright spot superimposed on the desired intensity pattern.

To separate the zeroth order and the desired intensity pattern, the principle design of the illumination beam path is to superimpose a Fresnel lens on the phase function. Light propagating through the liquid crystal is diffracted and focuses by the Fresnel lens to the focal plane at P_{im} , which is located in the front focal plane of the Lens 1. The zeroth diffraction order of light is reflected on the SLM without diffraction on the liquid crystals. The diffracted light and non-diffracted light will propagate through Lens 1. The non-diffracted light will be focused at the back focal plane of Lens 1 forming a very bright spot at P_{cp} . P_{cp} is the conjugated pupil plane of the objective lens, representing the spatial frequencies of the image. By introducing a high-pass filter at P_{cp} , the non-diffracted light (low frequencies) and the diffracted light (high frequencies) can be separated, resulting in a high contrast of the desired intensity pattern in the image plane in the sample.

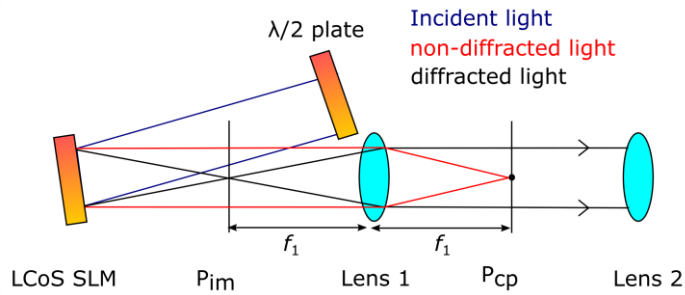


Figure 24 The principle design of the illumination beam path for generating an arbitrary illumination pattern using an LCoS SLM. By superimposing a Fresnel lens in the phase function, the diffracted light forms the desired intensity pattern at the position of P_{im} . The non-diffracted light is blocked at the position of P_{cp} .

3.4. Optical setup for the patterned illumination

The patterned illumination beam path was added to a standard 3D SMLM as discussed in Section 1.7. Figure 25 shows the combined optical setup including the Gaussian illumination mode and patterned illumination mode in the illumination beam path, which are highlighted by a blue and in the yellow background, respectively. The optical elements for the Gaussian illumination mode and the patterned illumination mode are highlighted by a gray and by a pink background, respectively.

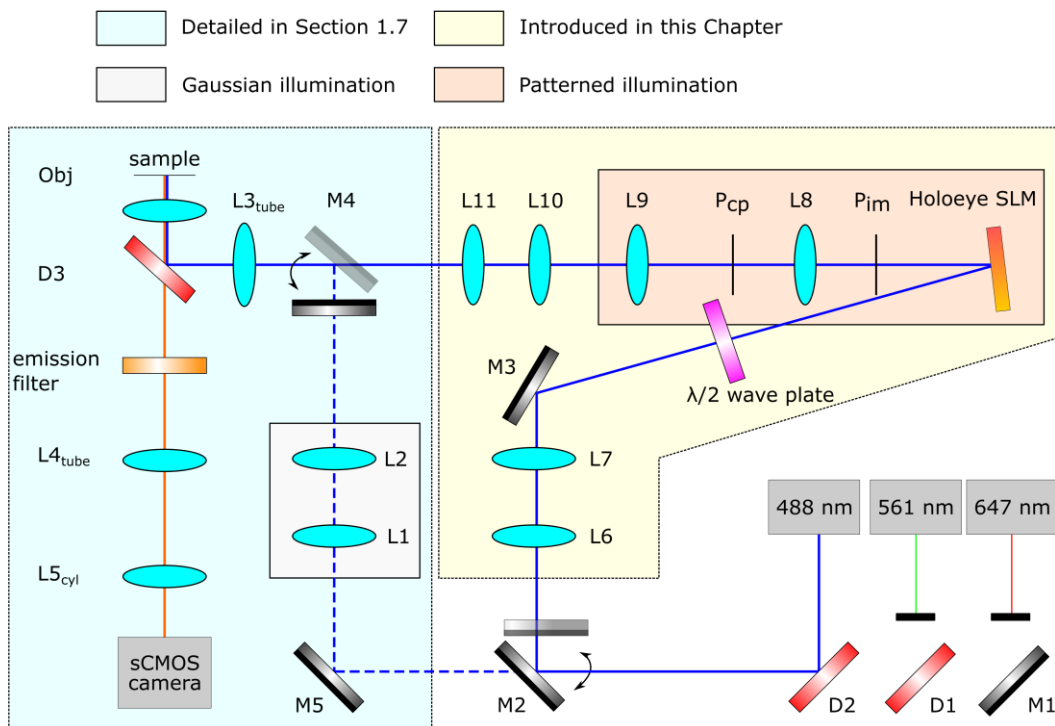


Figure 25 The patterned illumination single molecule localization microscope (piSMLM) including Gaussian illumination (background in blue) and patterned illumination modes (background in yellow).

The photograph of the piSMLM setup is shown in Figure 26. The blue line indicates the optical path of the laser for the patterned illumination mode and the green line indicates the optical path of the laser for the Gaussian illumination mode. The inset shows a central stop which has a small black paper in the center of the glass cover slip to block the zeroth diffraction order at P_{cp} .

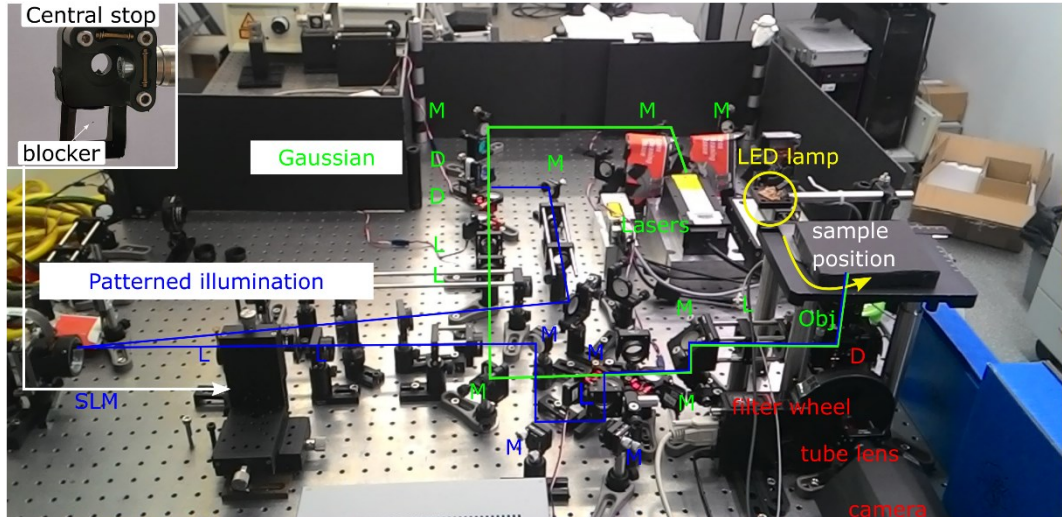


Figure 26 The optical setup of piSMLM. The blue line indicates the patterned illumination beam path and the green line indicates the Gaussian beam path. The inset image shows the central stop which blocks the zeroth diffraction order.

As demonstrated in Section 3.3, a Fresnel lens is superimposed onto the phase of the desired pattern to separate the zeroth diffraction order. By blocking the non-diffracted light consisting low frequencies at P_{cp} , high frequencies which preserve the fine structure of the desired intensity pattern can propagate through the optical system and illuminate the sample with the desired intensity pattern.

To determine the focal length of the Fresnel lens, a mirror with small holes is placed at the sample position. By illuminating the sample with a LED light, the position of the mirror sample was adjusted until nearly diffraction limited spots could be seen. Once the focal position is determined, the detection beam path is ensured to be aligned. Afterward, the mirror sample was illuminated using a laser with a defined intensity pattern generated by the GS algorithm. The focal length of the Fresnel lens was adjusted until the sample was illuminated with the desired intensity pattern showing the highest contrast. The focal length of the Fresnel lens was adjusted for each of the laser wavelength.

Table 3 shows the specification of the LCoS (PLUTO, HOLOEYE) used in the piSMLM setup. Using a phase modulator of SLM with a high reflectivity, a high fill factor and

a high diffraction efficiency, high losses of light can be prevented. Higher irradiance in the sample can be achieved by simply reducing the size of the ROI [SC2].

Table 3 Specification of the phase only LCoS PLUTO from HOLOEYE used in the piSMLM setup.

Reflectivity:	93%	Addressing:	8 Bit
Resolution:	1920 × 1080 pixels	Signal format:	DVI
Pixel pitch:	8.0 μm	Input frame rate:	60 Hz
Fill factor:	87 %	Diffraction efficiency:	60%
Active area:	15.36 × 8.64 mm	Phase shift:	2π at 633 nm

3.5. Homogeneous illumination

Without knowing the source intensity, the GS algorithm will not be able to provide the correct phase pattern to illuminate the sample with the desired target intensity. A method to improve the homogeneity of the desired target intensity pattern without knowing the source intensity is to introduce a calibration image to weight the target intensity. The calibration image includes the influences from the optical system, which can effectively reduce the inhomogeneity of the desired intensity pattern. The scheme of the modified GS algorithm is presented in Figure 27. The blue line indicates the improvement of the modified GS algorithm for the flat-top illumination.

For each of the laser wavelengths, a calibration image was generated using a square as a desired target intensity pattern. The phase was computed by the standard GS algorithm. The detailed description to acquire the calibration image can be found in [SC2]. The calibration image was normalized to one. The resulting calibration images for each of the laser wavelength can be seen in Figure 28. The calibration image was then used to calculate the new weighted target amplitude A_T^* :

$$A_T^* = A_T / \sqrt{\text{calibration image}}. \quad (9)$$

A fluorescent text marker sample was used to determine the illumination area of the Gaussian illumination. The results can be seen in the upper row of Figure 29. To identify the area where the laser illuminated the sample using the patterned illumination technique, a mirror sample with holes of about 200 nm in diameter was used. A square was defined as the desired intensity pattern as the input of the modified GS algorithm. Detailed information of the measurement for the patterned illumination can be found in [SC2]. The results of the patterned illumination for a desired square pattern for different laser wavelengths can be seen in the lower

row of Figure 29. As a result, the Gaussian illumination can be shaped to a defined intensity pattern with homogeneous distribution as shown in Figure 29.

To reduce the speckles in the desired intensity pattern several phase patterns were calculated using the GS-algorithm. Since the modified GS uses a random phase pattern as the initial phase, every final desired target intensity exhibits a different speckle pattern [88,97,98]. By displaying up to 40 precalculated phase patterns during the SMLM acquisition, an almost speckle free illumination pattern can be obtained. The homogeneity comparison of the defined illumination pattern based on the standard GS algorithm and the modified GS algorithm is shown in Figure 30. The detailed procedure to compute the speckle-free image can be found in [SC2].

The patterned illumination technique in combination with the modified GS algorithm allows to redistribute light efficiently with low power losses. As shown in Figure 31, the power is mostly independent of the size of the illumination pattern; whereas, the irradiance will increase with a decrease of the illumination area.

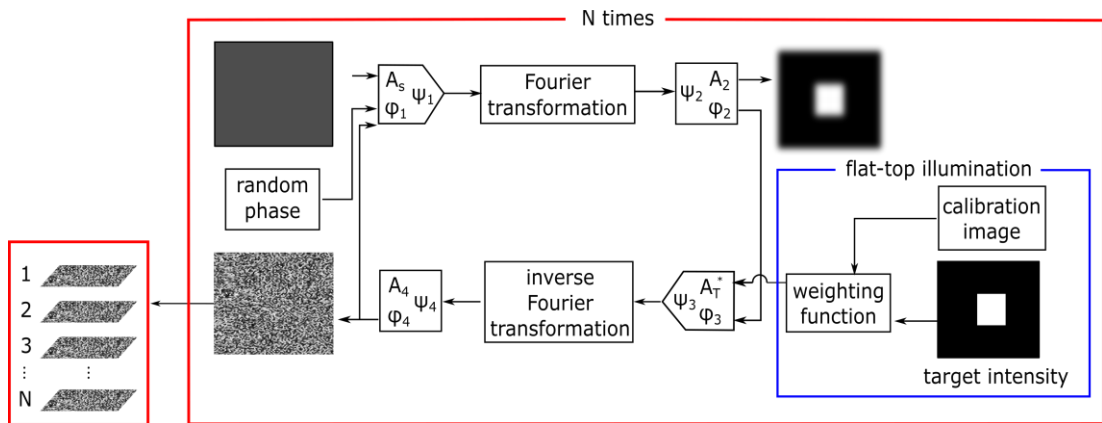


Figure 27 The modified Gerchberg-Saxton algorithm for the flat-top illumination indicated using a blue line. Reprinted with permission from [SC2] ©The Optical Society.

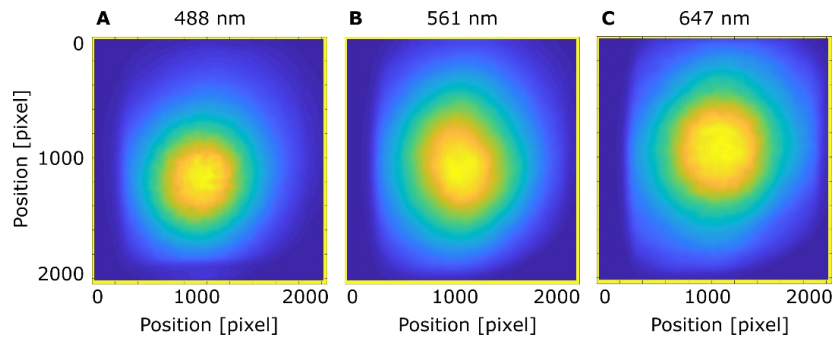


Figure 28 The calibration images for the three lasers used in the optical setup.

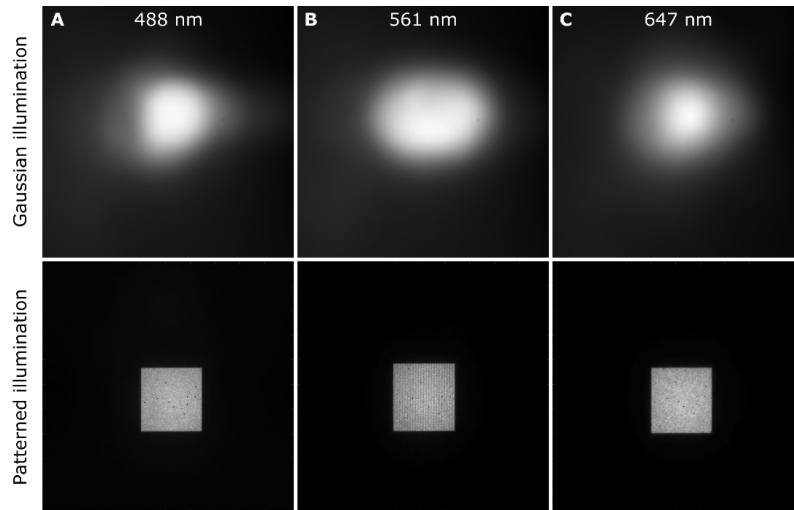


Figure 29 The illumination comparison between the Gaussian illumination and the patterned illumination from the three lasers.

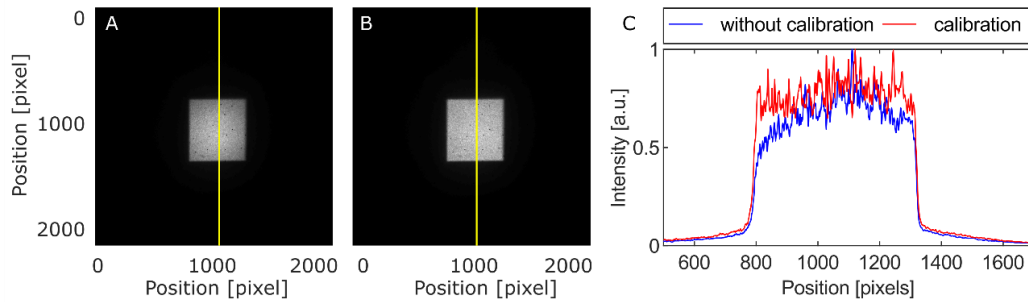


Figure 30 The intensity profile comparison between two illumination patterns. (A) The phase computed by the standard Gerchberg-Saxton algorithm and (B) by the modified Gerchberg-Saxton algorithm. (C) Intensity profiles of the position indicated with the yellow line in (A) and (B) Reprinted with permission from [SC2] ©The Optical Society.

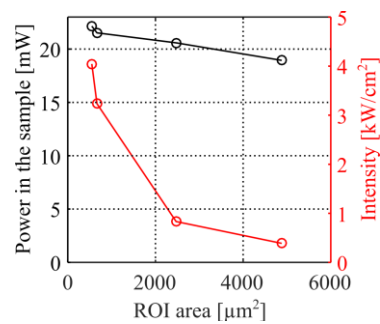


Figure 31 Plot of laser power versus ROI area and the corresponding irradiance. Reprinted with permission from [SC2] ©The Optical Society.

3.6. Imaging cell nuclei

For quantitative evaluation of the DNA density in cell nuclei, the fluorescence intensity distribution is evaluated. Since the piSMLM setup facilitates a flat-top illumination, it can ensure that the resulting fluorescence intensity from the sample is not significantly affected by the field dependency of the laser irradiance. As a comparison measurement, Gaussian illumination and homogeneous illumination were used to illuminate the same cell nucleus. The resulting images using these two illumination methods are shown in Figure 32.

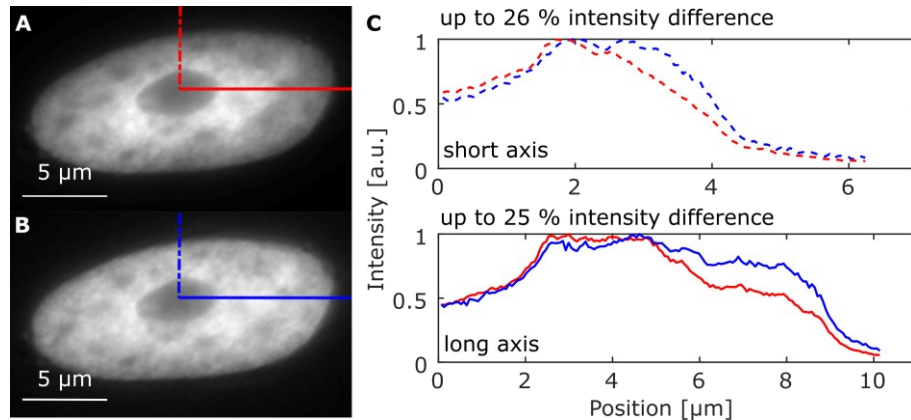


Figure 32 Imaging of a HeLa cell nucleus by (A) Gaussian illumination and (B) flat-top illumination. (C) The intensity profiles through the cell nucleus in two perpendicular directions (red: Gaussian illumination profiles, blue: flat-top illumination profiles). Reprinted with permission from [SC2] ©The Optical Society.

By means of Gaussian illumination as shown in Figure 32(A), the fluorescence intensity in the center of the nucleus is apparently higher than at the edge of the nucleus. This can be attributed to the Gaussian intensity profile of the laser which has the highest irradiance at the center of the illumination area and a lower irradiance in the edge. Whereas, the nucleus illuminated using the flat-top illumination shows smaller intensity variations as seen in Figure 32(B). Figure 32(C) shows the intensity profiles along the x and y axis. The intensity profiles indicate an underestimation of the DNA content at the periphery of the nucleus when using Gaussian illumination of up to 26%.

Homogeneous illumination is also essential for SMLM measurements, because the quality of the super-resolution image can be influenced in the periphery of the illuminated region where the irradiance is not high enough to induce blinking signals [99]. To evaluate nucleosome domain clusters in a cell nucleus, a defined ROI with flat-top illumination based on the modified GS algorithm was chosen to acquire SMLM data sets. A cell nucleus of the two daughter cells was selected for the patterned illumination as a demonstration. The detailed information about image acquisition using patterned illumination can be found in [SC2]. The

selected cell was assumed to be in the early interphase and did not yet start replication of the DNA. In the selected nucleus, 1232,754 DNA fluorophores were detected. The estimated thickness of the optical section is about 600 nm in the axial direction. The resulting 2D SMLM image is shown in Figure 33.

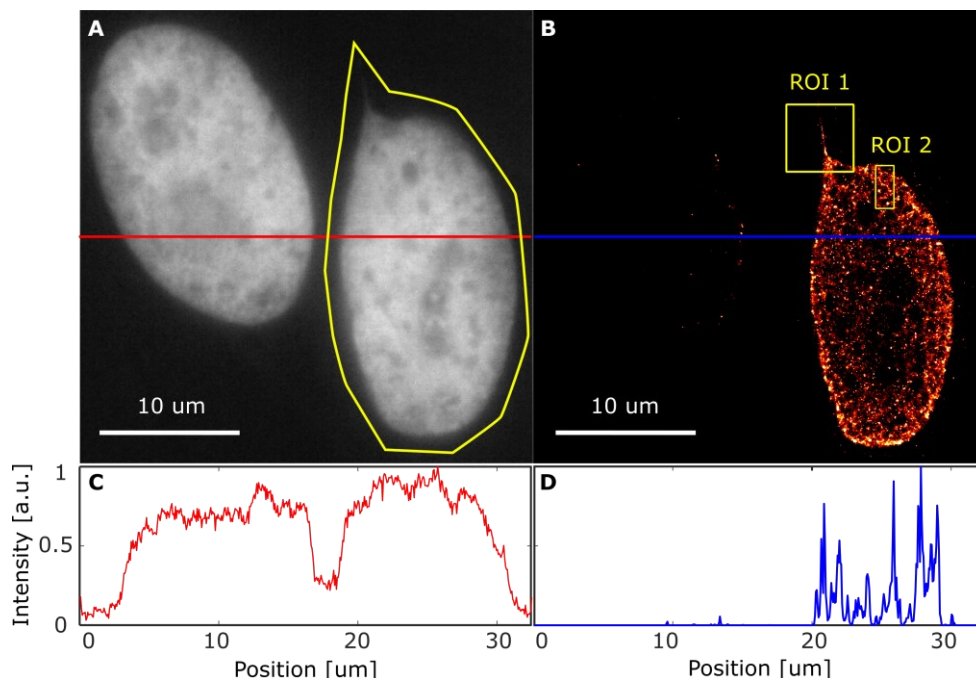


Figure 33 Imaging of nuclei based on patterned illumination. (A) Wide-field image of two daughter cell nuclei. The yellow contour indicates the area for illumination. (B) Super-resolution imaging of the selected nucleus. ROI 1 shows a chromatin protrusion. ROI 2 is used for cluster analysis. (C, D) The intensity profiles at the positions are indicated using a red line and a blue line shown in A and B, respectively. Reprinted with permission from [SC2] ©The Optical Society.

Figure 33(A) shows a wide-field image of the two nuclei acquired by homogenous illumination. Figure 33(B) shows the super-resolution imaging based on fBALM by imaging one of the nucleus. Intensity profiles are plotted at the position indicated by the red and blue lines in widefield and for the super-resolution images as shown in Figure 33(C,D), respectively. The intensity profile of the widefield image appears to have a small intensity variation. In contrary, a high variation of the intensity profile can be seen in the super-resolution image.

ROI 1 of Figure 33(B) shows a fine structure (chromatin protrusion) of the nucleus. A comparison between the wide-field image and the super-resolution image of the chromatin protrusion can be seen in Figure 34. The super-resolution image reveals a chromatin protrusion with a dimension of 50 nm at the position indicated by the arrows, which can not be seen in the widefield image.

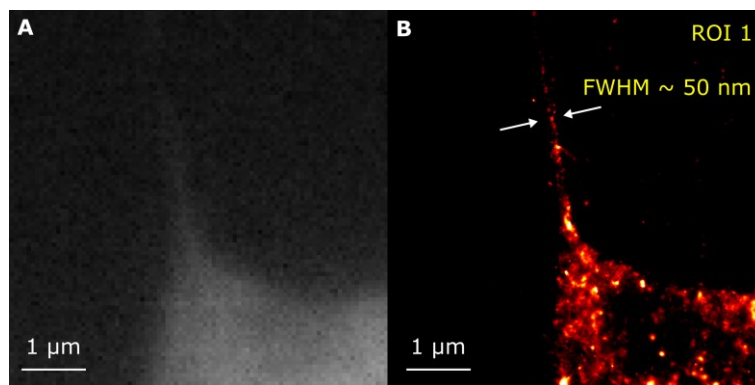


Figure 34 The chromatin protrusion image acquired using (A) conventional widefield microscopy and (B) super-resolution microscopy based on fBALM. The size of the chromatin protrusion is about 50 nm measured using the FWHM of the intensity profile at the position of the arrows.

According to the scheme of beads on a string shown in Figure 6, the nucleosome is the smallest packaging unit of DNA in the nucleus, which has a diameter of 11 nm. It can be packed into a higher-order of chromatin fibers with sizes of 30 nm and 120 nm [100]. A density based cluster analysis of the blinking DNA fluorophores using DBSCAN was performed to estimate the size of DNA packaging [101]. By defining the search radius of next neighbor molecules and the minimum number of molecules inside a cluster, the localized molecules in the nucleus can be clustered. The resulting clusters can represent different orders of chromatin packaging in the nucleus.

Several bright clusters can be seen in ROI 2 of the super-resolution image in Figure 33(B). The DBSCAN cluster analysis was then performed using a search radius of 12 nm and a minimum cluster size of 18 molecules. The resulting clusters are shown in Figure 35(B). Different sizes of clusters can be realized and three representative clusters are indicated at (I), (II) and (III) by red circles.

A histogram of the cluster size is shown in Figure 36. The DNA clusters can be classified into three categories with different sizes with a diameter (I) up to 30 nm (small-sized clusters), (II) above 30 nm up to 100 nm (middle-sized clusters), and (III) above 100 nm up to 180 nm (large-sized clusters). 105 small-sized clusters and 82 middle-sized clusters were found. Only 4 large-sized clusters were found. Although the cluster size can be changed by giving a different searching radius or a minimal distance to the neighbor molecules for DBSCAN, other recent publications reported similar sizes of chromatin in nuclei. An electron microscopy method based on ChromEMT showed that the chromatin is a chain with a diameter from 5 nm to 24 nm [102]. Another method based on SMLM using Alexa 647 EdU-labeling showed that the chromosomal regions consist of nanodomain clusters with a spatial extent of tens of nanometers [103].

However, it is not yet clear what kind of higher order chromatin fibers exists and what kind of relevant functions may be involved in such a hierarchical level of the chromatin organization [104,105]. SMLM single molecule data in combination with cluster analysis facilitate the visualization of the nucleosome domain clusters and potentially higher order organization of chromatin can be quantified to determine their structural patterns.

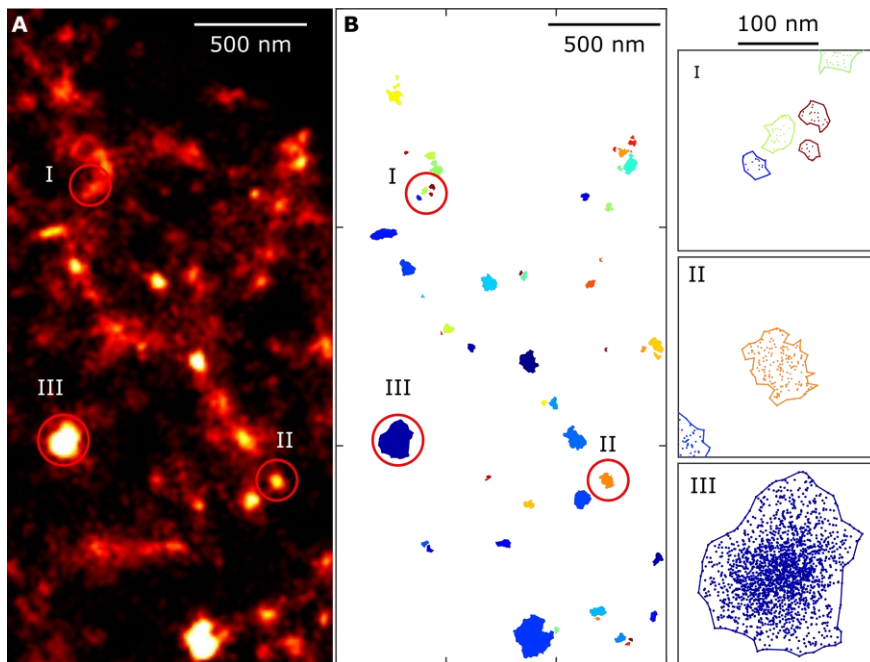


Figure 35 Cluster analysis based on DBSCAN using the localized DNA fluorophores in ROI 2 shown in Figure 33. Three representative sizes of nucleosome domain clusters indicated with red circles are shown in (A) a super-resolution image and (B) DBSCAN analysed nucleosome domain clusters. The region of a cluster is filled with a colour. I: Small size of clusters (up to 30 nm). II: Middle size of clusters (30 nm – 100 nm). III: Large size of clusters (100 nm – 180 nm).

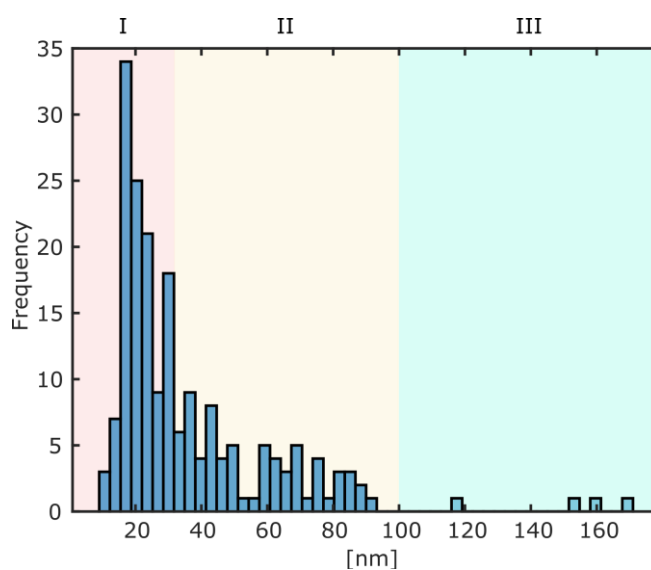


Figure 36 Histogram of the nucleosome domain cluster size using DBSCAN.

In a biological point of view, the localized DNA fluorophores (SytoxOrange) represent the binding sites of the DNA in the nucleus. For example, by analyzing the fluorophore density in the nucleus, the DNA molecule density can be used to estimate the accessibility of active genes in the nucleus [40]. The results of a DNA molecule density analysis can be seen in Figure 37, revealing different DNA densities in the nucleus in a range between 4 and 14 SMs/100 nm². To achieve a better quantification analysis of the nucleus, the DNA should be completely labeled and the fluorophores should blink only one time to ensure the localization of the DNA at each binding site will be counted only once.

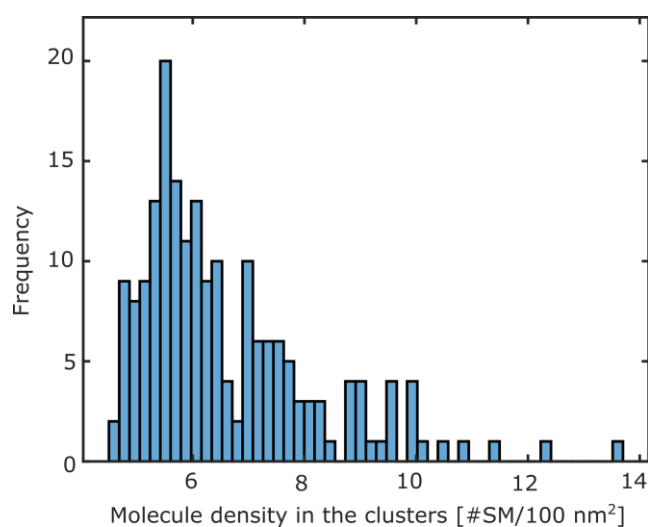


Figure 37 Histogram of the molecule density in the clusters .

3.7. Discussion of imaging nuclei based on fBALM

The chemical composition of the imaging buffer used in fBALM is similar to the imaging buffer used for organic fluorophores. The buffer contains an enzymatic reaction based on glucose oxidase catalase. Since it produces gluconic acid and hydrogen peroxide, the pH value of the buffer decreases over time [28,58]. For YOYO-1, with the help of a gradual reduction of the pH value, the optimal condition for sufficiently blinking signals were determined to be the pH value of 3.7. About 2 to 3 hours should be waited in the beginning of the experiment until the imaging buffer reaches the optimal pH value [58]. The continuous decreasing pH value can restrict the time for imaging a 3D nucleus, because the image acquisition can take more than an hour to acquire sufficient blinking signals. Moreover, the sample cannot be imaged again because the majority of the fluorophores diffused into the imaging buffer and low concentrated DNA intercalation dyes may be difficult to associate to the DNA structure.

One possible method to minimize the effect of buffer acidification during the image acquisition for imaging nuclei is to optimize the buffer system. The new buffer should have a gradually decreasing pH value. Once the pH value of the buffer reaches a value of 3.7, it can stay constant during the image acquisition. Another approach for imaging nuclei for long time is to equip the microscope with a pump system to exchange the imaging buffer gradually [106]. By exchanging the imaging buffer and relabeling the nuclear structure, blinking DNA fluorophores can be acquired continuously. A more applicable method is to have intrinsic blinking DNA fluorophores without the dependency of the buffer condition while image acquisition. A stable imaging environment is beneficial for the quantification analysis of a 3D nucleus.

Chapter 4 Nanographenes for SMLM

Although a number of fluorophores were demonstrated to be suitable for SMLM, most organic fluorophores have sufficient blinking properties only when embedded in special imaging buffers. For DNA fluorophores based on the fBALM method, for example, an acidic imaging buffer is used to allow DNA fluorophores to associate to and disassociate from the DNA structures dynamically. In this Chapter, fluorescent materials based on graphene are introduced. They have intrinsic blinking properties independent of the imaging buffer, which arises the potential for a new class of fluorophores for SMLM in applications such as material science and bio-imaging.

4.1. Graphene and nanographene

Graphene is a flat, single-atom-thick monolayer of graphite, which forms a planar hexagonal configuration like a honeycomb lattice [107]. It is composed of sp^2 – hybridized carbon atoms, which are covalently bonded to each other. A schematic diagram of a monolayer of graphene can be seen in Figure 38. The very first method to obtain a stable monolayer of graphene was to use regular adhesive tape resulting in a large graphene sheet [108].

For fluorescence microscopy, fluorophores with a small size are more applicable, because they are located close to the targeted biomolecules after labeling. To produce small graphene fragments, which are called graphene quantum dots (GQDs) or graphene molecules (GMs), two different approaches can be used. The synthetic approaches can be classified by a top-down approach and a bottom-up approach [109]. Both approaches result in graphene fragments with a size of several nanometers. The fragments have tunable photoluminescence properties, high photostability, and good biocompatibility, which makes them suitable for fluorescence microscopy [110,111]. The top-down synthesis method uses physical or chemical techniques to cleave carbonaceous raw materials. This method allows synthesizing large quantities, but the size of graphene fragments and the resulting products are difficult to control. The bottom-up synthesis method relies mostly on solution or surface mediated organic reactions to derive nanographenes. Therefore, this method can be used to synthesize nanographenes with atomic precision in small quantities [112–115].

In this Chapter, bottom-up synthesized nanographenes were studied particularly, because they have the potential to be synthesized with specific ligands to bind to biomolecules. These nanographenes are small with a size of 1-5 nm, which is as small as organic fluorophores.

They were reported to be stably fluorescent which makes them suitable for fluorescence microscopy [109,116,117].

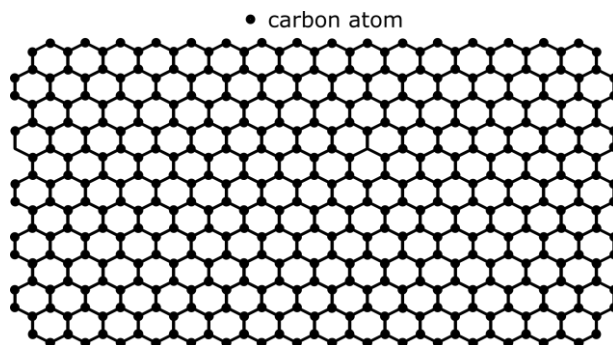


Figure 38 A scheme of 2D graphene material composed by carbon atoms.

4.2. Fluorescence properties of nanographenes

The fluorescence properties of the nanographenes DBOV-Mes (GM-C38), GM-C60, GM-C78 and GM-C96 were characterized in [113,114,118,119]. DBOV-Mes has zigzag periphery and the structures of GM-C60, GM-C78 and GM-C96 have a full armchair periphery. Their chemical structures are shown in Figure 39.

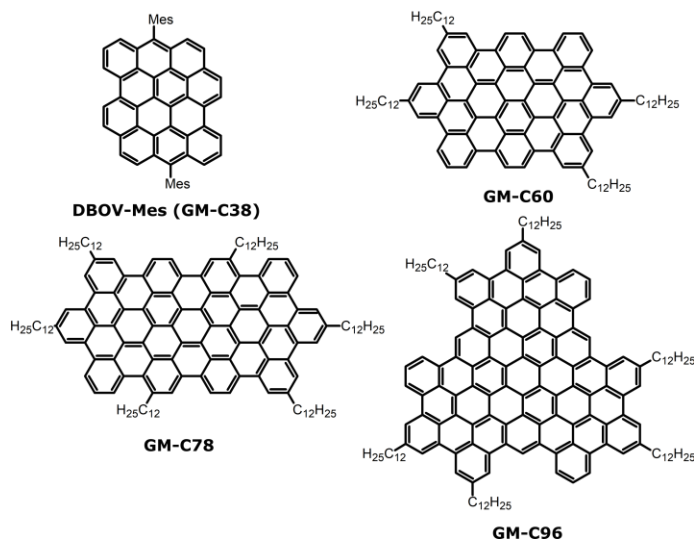


Figure 39 The chemical structures of DBOV-Mes (GM-C38), GM-C60, GM-C78 and GM-C96 [113,114,118,119].

The fluorescence properties of the nanographenes and Alexa 647 are shown in Table 4. Detailed information about the fluorescence properties can be found in [SC3]. DBOV-Mes has the highest extinction coefficient, quantum yield and brightness compared to the other nanographenes (GM-C60, GM-C78 and GM-C96). In comparison to Alexa 647, DBOV-Mes exhibits more than twice higher quantum yield, but a lower brightness and a smaller extinction coefficient. Additionally, DBOV-Mes has a small Stokes shift and the narrowest emission

spectrum among the tested nanographenes. Such fluorescence properties of fluorophores are beneficial for multi-color imaging because an overlapping of the spectra [120] can be avoided. Therefore, in the following, DBOV-Mes was chosen to demonstrate the ability of nanographenes for SMLM experiments. Applications in super-resolution imaging for material science and bio-imaging will be presented in Section 4.5 and in Section 4.6, respectively.

Table 4 Fluorescence properties of Alexa 647, DBOV-Mes (GM-C38), GM-C60, GM-C78 and GM-C96 [SC3].

Dye	Excitation maximum (nm)	Emission maximum (nm)	Extinction ($M^{-1}cm^{-1}$)	Quantum yield	Brightness ($M^{-1}cm^{-1}$)
Alexa 647 [27]	650	665	239,000	0.33	78,870
DBOV-Mes (GM-C38)	610	614	70,000	0.79	55,300
GM-C60	412	701	22,000	0.1	2,200
GM-C78	—*	513	54,000	0.02	1,080
GM-C96	491	650	61,000	0.01	610

*Due to the measurement limitation of the spectrometer, the peak of the excitation spectrum of GM-C78 was not available.

4.3. *Blinking properties of nanographenes*

Several important blinking properties of nanographenes were evaluated based on the method presented in [27]. The blinking properties of the nanographenes in three different environments including air, Dulbecco’s Phosphate-Buffered Saline (DPBS) and polystyrene are compared with Alexa 647 in an imaging buffer containing an oxygen scavenging system in the presence of thiol. The detailed experimental results can be found in [SC3]. The blinking properties include:

- (1) *Photon number per switching event*: Localization precision is dependent on the number of detected photons and the width of the PSF. Assuming the width of the PSF in a microscope system is constant, a high number of detected photons per switching event will result in a better localization precision.
- (2) *Photostability*: In the beginning of the experiment, it is common that the fluorophores are excited by a relatively high laser intensity ($5-30 \text{ kW/cm}^2$) to transfer the majority of the fluorophores into the dark state [19]. When fluorophores are excited by such high intensities the covalent bounds can be modified resulting in photobleaching. Fluorophores with a good photon resistance are therefore highly desirable.
- (3) *On-off duty cycle*: On-off duty cycle is defined as a ratio of time, at which the fluorophore stays in the on-state in respect to the off-state time. For SMLM, it is important to have only a

small fraction of fluorophores in the on state, while the majority of the fluorophores are present in the off state, which will result in optically isolated molecules in the images. Therefore, fluorophores with a low duty cycle will be more applicable to achieve high-resolved images.

(4) *Number of switching cycles*: For an ideal switching, a fluorophore has only one on-off cycle. During the SMLM image acquisition, the fluorophore appears in the on-state in one frame and is in the off-state for the rest of the acquired frames. In experiments, where structural features are to be investigated, fluorophores are considered to be advantageous if they can be switched many times. Subsequently, they can be localized multiple times and the true position can be determined in the reconstructed image after averaging the position of the same molecule [72].

Nanographenes have a high photon number per blinking event and low duty cycle, which make them comparable with Alexa 647. These properties render them suitable for SMLM experiments without an additional imaging buffer preparation. The slightly longer blinking time compared to Alexa 647 can be useful for super-resolution methods like MINFLUX, which may require a longer on-state for searching the position of the fluorophore [121].

Table 5 Blinking characteristic of Alexa 647 in an imaging buffer; DBOV-Mes and GM-C60 in three different imaging environments including DPBS, air and polystyrene; GM-C78 and GM-C96 in polystyrene [SC3].

Dye	Alexa 647	DBOV-Mes (GM-C38)			GM-C60			GM-C78	GM-C96
Environment	Blinking buffer*	DPBS buffer	Air	Poly-styrene	DPBS buffer	Air	Poly-styrene	Poly-styrene	Poly-styrene
Detected photons per switching event	3,438	4,918	5,570	4,902	3,673	4,960	4,690	5,740	5,020
Duty cycle ($\times 10^{-4}$)	2.1	1.3	4.7	8	5.3	1.2	3.2	2.7	1.7
Blinking time (ms)	65	87	108	54	75	79	96	83	94

*glucose oxidase catalase buffer in the presence of thiol [27].

4.4. Fluorescence recovery after UV irradiation

Some organic fluorophores have a reversible blinking property when embedded in a special imaging buffer, because of a significant change of the absorption spectrum upon irradiation [19,24]. Without embedding in the imaging buffer, a similar characteristic of fluorescence recovery of DBOV-Mes can be seen in Figure 40. DBOV-Mes exhibits a fluorescence recovery after exposing to laser radiation with a wavelength of 405 nm. The experiment was performed using a pair of lasers. A laser with a wavelength of 532 nm was

used for the excitation and a laser with a wavelength of 405 nm was used to recover the fluorescence signals. The repeatable recovery of the fluorescence signals can be seen in Figure 40. The insets show three representative images of sparse nanographenes in the sample at three different time points. Frame 1 shows nanographenes at the beginning of the laser illumination; frame 20,000 shows nanographenes after 18 minutes illumination with the laser with a wavelength of 532 nm; frame 20,001 shows the fluorescence recovery upon a short time (~ 1 s) illumination using the laser with a wavelength of 405 nm. Several fluorescence recoveries of the nanographene were performed repeatedly during another 18 minutes.

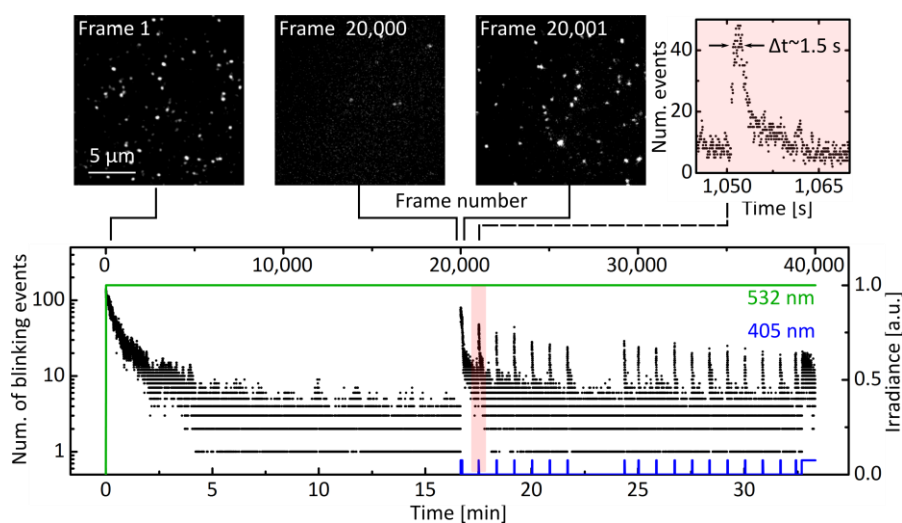


Figure 40 Three representative images of blinking events of DBOV-Mes in air. Fluorescence recovery using a laser with a wavelength of 405 nm. Reprinted with permission from [SC3] © 2019 Wiley-VCH Verlag GmbH & Co. KGaA.

4.5. Correlative 3D SMLM and atomic force microscopy (AFM)

A demonstration of nanographenes used in 3D SMLM was performed. Correlative microscopy was used to compare the images acquired by two different high-resolution methods based on atomic force microscopy (AFM) and 3D SMLM. The detail experimental procedure and the experimental protocols can be found in [SC3].

Figure 41(A) shows the scheme of the experimental procedure to deposit nanographenes on a cover slip with crevices on the surface. Subsequently, 3D SMLM and AFM were performed to image the crevices on the cover slip. For 3D SMLM, the localized molecules were accumulated into two super-resolution images according to their bimodal distribution in the axial position. Figure 41(B) shows an intensity projection of the localized molecules which are located between $z = +300$ nm to -10 nm. Since the molecules are on the glass surface, it shows a relatively homogeneous distribution of nanographenes. Figure 41(C)

shows the intensity projection of the deeper localized molecules with a location between $z = -10$ nm and -300 nm. The resulting image shows a clear structural pattern of crevices in the cover slip. Figure 41(D) shows the AFM image at the same area acquired with the SMLM method. Figure 41(E) shows the image registration of the two high-resolution images. The line profile of the AFM image and the super-resolution image are shown in (F) and (G), respectively.

The above experiments demonstrate the capability of using nanographene in SMLM. Without embedding the sample in a special imaging buffer, DBOV-Mes in air has good blinking properties resulting in a high-resolution 3D SMLM image. After image registration with the image acquired by AFM, the high-resolution image of 3D SMLM shows highly correlated fine structures. The capability of DBOV-Mes blinking in air shows a significant advantage in the application of SMLM in material science compared to the organic fluorophores, which requires a special imaging buffer.

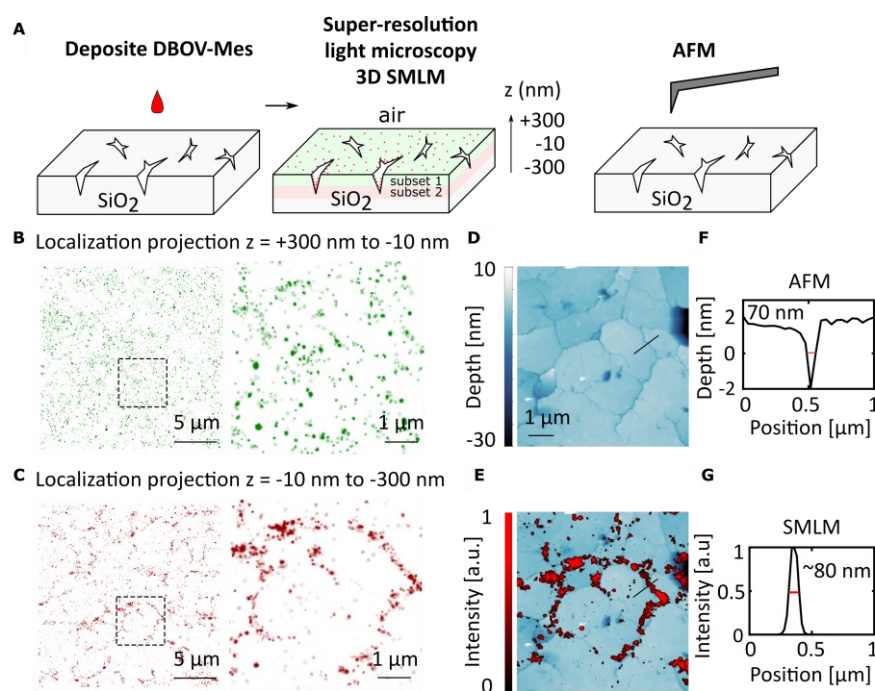


Figure 41 Correlative super-resolution microscopy based on 3D SMLM and AFM. (A) Depositing DBOV-Mes on the glass surfaces (B,C) Accumulation of localized molecules of two different subsets. (D,E) AFM and image registration of the SMLM using the ROI shown in (C). (F,G) FWHM of the width of the crack indicated by a line shown in (D). Reprinted with permission from [SC3] © 2019 Wiley-VCH Verlag GmbH & Co. KGaA.

4.6. Water soluble nanographenes for bio-imaging

In the previous section, correlative 3D SMLM and AFM was demonstrated as a proof of principle experiment using nanographenes for SMLM. However, the original material was synthesized in toluene for applications such as optoelectronic and organic light emitting diodes

(OLEDs) [113,122]. It is necessary to synthesize water soluble nanographenes for bio-imaging applications.

As shown in Section 4.3, DBOV-Mes has the best fluorescence and blinking properties among the four described nanographenes (Figure 39). The water-soluble groups tetraethylene glycol methyl ether were attached to DBOV-Mes for investigation of their fluorescence properties and biocompatibility for fluorescence microscopy [123].

The absorption and emission spectrum of DBOV-Mes-OTEG and Alexa 647 are shown in Figure 42. In comparison with DBOV-Mes, DBOV-Mes-OTEG has an excitation wavelength red-shifted from 610 nm to 658 nm and an emission spectrum shifted from 614 nm to 667 nm. DBOV-Mes-OTEG exhibits a comparable spectrum as standard far-red fluorophores. The emission spectrum overlaps well with the emission spectrum of Alexa 647. Therefore, DBOV-Mes-OTEG can be imaged using a commonly equipped filter cube for far-red fluorophores in a commercial fluorescence microscope.

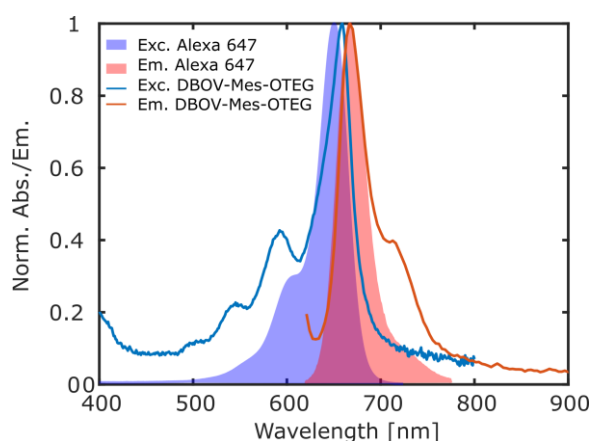


Figure 42 Spectral comparison between the water solvable DBOV-Mes-OTEG and Alexa 647 [4].

A proof of principle experiment for bio-imaging was performed by incubating DBOV-Mes-OTEG with mammalian cells (U2OS) for 24 hours. DBOV-Mes-OTEGs were brought into cells through endocytosis to examine their localization in cells. After fixation of the cells, the blinking properties of DBOV-Mes-OTEG were examined. The sample was embedded in DPBS, a commonly used buffer in biological researches for SMLM experiments. An image stack with 10,000 frames showing blinking of nanographenes inside the cell was acquired to investigate the blinking behaviour of nanographene. The long time experiments were performed using a laser with an irradiance of 10 kW/cm².

The images of conventional microscopy and 3D SMLM are shown in Figure 43. (A) shows an image overlay of bright-field microscopy and fluorescence microscopy. The ROI

indicated by a red rectangle was then imaged using the 3D SMLM method. The blinking DBOV-Mes-OTEGs were acquired at the nuclear membrane. The intensity projection of a 50 nm thin section of the 3D SMLM image can be seen in (B). A confined enrichment of DBOV-Mes-OTEGs in endocytotic vesicles, lysosomes lipid droplets and other cellular regions due to the chemical nature of DBOV-Mes-OTEG can be observed.

The experimental results show that DBOV-Mes-OTEGs in cells exhibit good blinking properties without special imaging buffer. After a continuously high laser irradiance (10 kW/cm^2) for about 90 minutes, no significant decrease of blinking signals was observed. Sufficient blinking signals could be seen using a laser with a low irradiance of about 0.2 kW/cm^2 . Therefore DBOV-Mes-OTEG can be used practically as a dye for fluorescence and for super-resolution microscopy, because of their good photostability. When a specific ligand to bind to DNA is synthesized, DBOV-Mes-OTEG can be used for imaging nuclei.

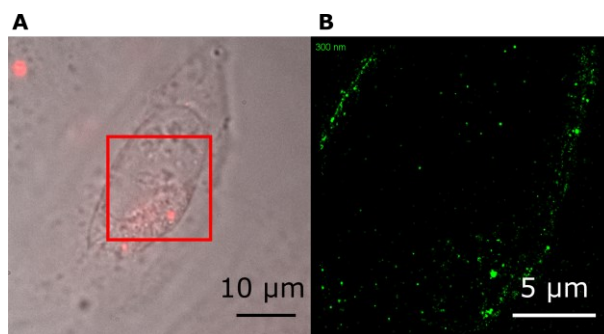


Figure 43 Conventional microscopy image and super-resolution image of a U2OS cell after 24 hours incubation of DBOV-Mes-OTEG. The sample was embedded in DPBS. The ROI shows the illumination area of SMLM (A) An image overlay of the bright-field image and the fluorescence image. (B) Intensity projection of the super-resolution image with an selected axial thickness of 50 nm.

Chapter 5 Conclusion

SMLM provides an essential tool to image cellular structures, which can not be resolved with a conventional microscope. This super-resolution microscopy technique has been used to visualize different cellular organelles to achieve unprecedented resolution down to several nanometers. It is yet a challenge to image cellular nuclei due to their complex structures and large volume in three dimensions. The goal of this PhD thesis was to develop SMLM methods for imaging nuclear structures in 3D. This thesis includes a broad view of methods in SMLM including an advanced design of the microscope and the development of a fluorophore based on graphene.

For the improvement of the microscope, an original work of this PhD research was to develop a drift correction method based on speckle patterns originating from back-scattered light [SC1]. The speckle pattern based drift correction method is especially beneficial for imaging nuclei, because this method utilizes the intrinsic structure of a cell as a position reference in 3D. Therefore, it enables the users to image cellular structures for a long time without drift shown in the reconstructed image. A demonstration of this drift correction method was performed for imaging a nucleus based on the fBALM method using a standard SMLM setup. Several clusters were found in the super-resolution image of the nucleus. After drift correction, more confined nucleosome domain clusters in 3D were revealed, which could not be observed without drift correction. The position of DNA fluorophores which are drift corrected can be used for quantitative evaluation to reveal the true structural organization of the nucleus.

Another original work during this PhD research was the design of an optical beam path which allows users to define regions of interest for illumination [SC2]. This method can minimize the area of light exposure to avoid early photobleaching of fluorescent labels in biological targets. Based on a Computer Generated Holograms, the phase of the desired intensity pattern for illumination was computed using a modified Gerchberg-Saxton algorithm. By projecting the computed phase on a SLM, a defined pattern for illumination can be obtained. The big advantage of this optical design is that light can be efficiently distributed with low loss of power. By defining a small region of interest, a sufficient irradiance to induce blinking fluorophores can be achieved without a laser with high power. Therefore, this method can be used for diverse SMLM applications when high irradiance is required. The user-defined intensity pattern facilitates flat-top illumination, which is beneficial for quantitative analysis. For imaging nuclei, a cell nucleus was illuminated using the flat-top illumination. The spatial

organization of the nucleus was analyzed using a density based cluster analysis on the localized DNA fluorophores. Different sizes of the clusters in the nucleus was obtained.

The above-mentioned improvements solve certain problems of the microscope for SMLM. However, fluorescent labeling using commercial available fluorophores is a principle restriction for SMLM, because sufficient blinking signals can only be acquired with a careful adjusted chemical environment in the sample. A new class of fluorophores based on nanographenes was developed during the PhD research for the practical use of SMLM in material science and bio-imaging [SC3]. The fluorescence properties of four different nanographenes were investigated. It was discovered that they have intrinsic blinking characteristics, which are comparable with the commonly used organic fluorophore Alexa 647. Furthermore, they show only a small dependency on the environmental conditions. Highly comparable blinking signals were achieved in air, which makes them suitable for applications in material science. For the demonstration of nanographene in applications for material science, 3D SMLM was performed to image the fine structure of a cover slip with small crevices on the surface. Another high-resolution image method based on AFM was performed to confirm the structure shown in the SMLM image. Similar structures of the crevices were acquired after image registration.

A water-soluble nanographene was then investigated to study their capability for bio-imaging. Its biocompatibility and blinking characteristics were confirmed to be suitable for SMLM. Although the demonstrated water-soluble nanographenes cannot be used to label DNA molecules in nuclei, this nanographene could be imaged for a long time without significantly decreasing of the blinking characteristic. Therefore, this nanographene may be suitable for imaging nuclei, when additional ligands are synthesized to bind to DNA molecules. The complete optical setup presented in this PhD thesis shows the potential to image nuclear structures with high resolution in three dimensions with the help of blinking fluorophores based on nanographene.

The advanced optical setup for SMLM presented in this PhD thesis is indeed not restricted to only image cell nuclei. It can be used to image other biological sample targets, when high-resolution is required. The advanced design of the optical setup and the development of nanographenes with a specific ligand to bind to a biomolecule can broaden the range of applications for SMLM in biology and in material science.

Publication list

1. **S.-Y. Chen**, R. Heintzmann, C. Cremer, "Sample drift estimation method based on speckle patterns formed by backscattered laser light," Biomed. Opt. Express (2019). DOI: <https://doi.org/10.1364/BOE.10.006462>
2. **S.-Y. Chen**, F. Bestvater, W. Schaufler, R. Heintzmann, and C. Cremer, "Patterned illumination single molecule localization microscopy (piSMLM): user defined blinking regions of interest," Opt. Express (2018). DOI: <https://doi.org/10.1364/OE.26.030009>
3. X. Liu[‡], **S.-Y. Chen**[‡], Q. Chen, X. Yao, M. Gelléri, S. Ritz, S. Kumar, C. Cremer, K. Landfester, K. Müllen, S. Parekh, A. Narita und M. Bonn," Nanographenes: ultrastable, switchable, and bright probes for super-resolution microscopy," Angew. Chem. Int. Ed. (2019). DOI: <https://doi.org/10.1002/anie.201909220>

[‡] Authors contribute this work equally

Publication 1

[SC1] Sample drift estimation method based on speckle patterns formed by backscattered laser light

Shih-Ya Chen, Rainer Heintzmann, and Christoph Cremer

Biomed. Opt. Express, 10(12), 6462-6475 (2019)

DOI: <https://doi.org/10.1364/BOE.10.006462>

Author	Shih-Ya Chen
Conceptual research design	x
Plan of research activities	x
Data collection	x
Data analyses and interpretation	x
Manuscript writing	x
Suggested publication equivalence value	1.0

This paper is published by The Optical Society under the terms of the [OSA Open Access Publishing Agreement](#). No reprinted permission is required.

Sample drift estimation method based on speckle patterns formed by backscattered laser light

SHIH-YA CHEN,¹ RAINER HEINTZMANN,^{2,3} AND CHRISTOPH CREMER^{1,4,*} 

¹*Institute of Molecular Biology, Mainz, Germany*

²*Institute of Physical Chemistry and Abbe Center of Photonics, Friedrich-Schiller-University Jena, Jena, Germany*

³*Leibniz Institute of Photonic Technology, Jena, Germany*

⁴*Department of Physics, University of Mainz (JGU), Mainz, Germany*

**cremer@kip.uni-heidelberg.de*

Abstract: Single molecule localization microscopy (SMLM) has been established to acquire images with unprecedented resolution down to several nanometers. A typical time scale for image acquisition is several minutes to hours. Yet it is difficult to avoid completely sample drift for long time measurements. To estimate drift, we present a method based on the evaluation of speckle patterns formed by backscattered laser light from the cells using a single molecule localization microscope setup. A z-stack of unique speckle patterns is recorded prior to the measurements as a three-dimensional position reference. During the experiment, images of scattered laser light were acquired, and correlated individually with each of the images of the speckle reference stack to estimate x, y and z drift. Our method shows highly comparable results with a fiducial marker approach, achieving a precision of several nanometers. This method allows for high precision three dimensional drift correction of microscope systems without any additional sample preparation.

© 2019 Optical Society of America under the terms of the [OSA Open Access Publishing Agreement](#)

1. Introduction

Single molecule localization microscopy (SMLM) was developed to achieve super-resolved microscopy images with unprecedented resolution down to several nanometers [1–4]. However, sample drift occurs commonly during image acquisition. A small amount of drift in the microscope system can induce blurring artifacts in the reconstructed image, hampering resolution. This is especially disadvantageous in 3D SMLM where the reconstructed 3D image depends critically on the correct axial coordinate. Therefore, correction of sample drift is essential and several approaches were presented to correct sample drift in microscope systems.

One of the most common approaches is based on image post-processing using cross-correlation of the fluorescence emission localization data[5–7]. This method sorts blinking molecules in time intervals of an equal length. The combined blinks in each time interval form a 3D structure. The cross-correlation of the 3D structures of every time interval with the corresponding reference structure of the first time interval will yield the drift during the experiment. The position of the detected molecules is then adjusted according to the result of the computed drift. However, this method requires a sufficient number of blinking events in the reconstructed images to provide visible features for the calculation. Biological targets with distinct features such as filaments, a fiber-like structure, may result in better drift accuracy compared to samples without clear structures.

Another common approach is to prepare fiducial markers on the coverslips such as gold nanoparticles or fluorescent beads [8,9]. By tracking the positions of the fiducial markers, the

drift of the microscope system in three dimensions is obtained. The advantage of this drift correction method is that biological features in the images are not required. However, fiducial markers need to be prepared before the preparation of the samples. Additional optimization of sample preparation for the fiducial markers is recommended to prevent aggregation and inhomogeneous distribution of the markers on the coverslip, which has undesired influence on finding appropriate markers for drift correction [10].

An alternative approach for drift correction is to fabricate a fiduciary micro-pattern by the means of a lithography method [11]. Manufacturing directly imprinted coverslips significantly reduces the effort of sample preparation, but they might not be easily accessible and affordable for standard bio-imaging laboratories.

A hardware-based approach is to introduce an infrared LED light source in the microscope system. By detecting the reflection at the interface between the cover glass and the embedding medium, the axial position is tracked and constantly adjusted during image acquisition [12]. This method presents a convenient axial drift correction and focus stabilization for microscope users. However, an additional lateral drift correction method should be applied in order to realize a three dimensional correction.

An alternative approach is based on image correlation using bright-field images of samples illuminated by an infrared LED. This approach provides an advanced method to simultaneously correct drift in three dimensions [13]. This method requires an additional light source for illumination and sufficient features in the bright-field images for a correlation analysis.

In this report, we present a method for SMLM based on speckle pattern image correlation to estimate sample drift in three dimensions. A home-built microscope setup equipped with laser light sources was used to demonstrate the drift estimation method. Using only low power of the laser, the interference of the backscattered laser light of a cell sample results in a speckle pattern in the acquired image. Due to the complexity of cells, the speckle pattern is unique and varies strongly with focus position. Therefore, the speckles can be used to provide a straightforward positioning reference for the drift estimation measurements. By recording a z-stack of images showing laser speckles, the three dimensional position information of the cell sample is encoded in this reference stack. We used an image registration method based on nonlinear optimization and discrete Fourier transforms (DFTs) [14]. This method can achieve high accuracy without demanding computational time and memory. By correlating the scattered laser images individually with each of the images from the speckle reference stack using the DFT method will yield x, y and z drift information. Below we describe our method to determine accurately the 3D sample position and validate it on fiducial markers (fluorescent beads) experiments. Additionally, a 3D SMLM image of a cell sample is presented to demonstrate our drift correction approach.

2. Methods

2.1. Experimental setup

A home-built SMLM based on the setup presented in [15] was used to acquire images for the proposed drift estimation method. The scheme of the setup is shown in Fig. 1. The microscope was equipped with a 488 nm (Omicron, Germany), a 561 nm (Frankfurt Laser, Germany) and a 647 nm (Cobolt, Sweden) laser. A telescope consisting of two lenses L1 ($f = 30$ mm, Thorlabs) and L2 ($f = 60$ mm, Thorlabs) was used to expand the laser beam. A quad band dichroic (Chroma, zt405/488/561/647rpc) was used to reflect the lasers. A tube lens ($f = 120$ mm, Thorlabs) was utilized to focus the beam into the back focal plane of the objective lens (HCX PL APO 100 \times /NA 1.47 OIL, Leica) mounted in a nanometer positioning piezo stage (P-721, Physik Instrumente). The immersion oil with a refractive index of 1.518 (at 23 $^{\circ}$ C, Zeiss) was applied on the objective lens. The samples were placed on a manually controlled x-y stage. The focus was adjusted

using a manual z-axis translation mount (SM1Z, Thorlabs) and the white light LED was used for bright-field illumination.

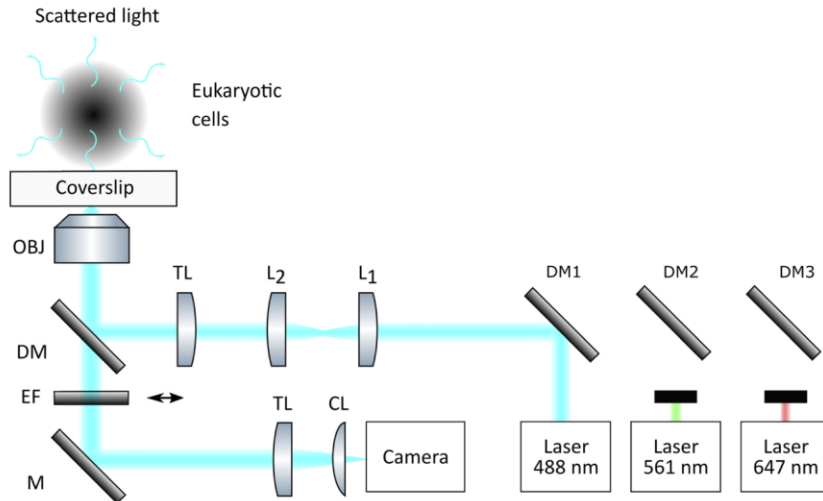


Fig. 1. Demonstration of imaging speckle patterns using a standard SMLM setup. (Obj: objective lens, DM: dichroic mirror, EF: emission filter for fluorescent beads measurement and for 3D SMLM, M: mirror, TL: tube lens, CL: cylindrical lens, L: lens)

A tube lens ($f = 200$ mm, Thorlabs) was used to image the sample onto a sCMOS camera (PCO edge 4.2, PCO). A cylindrical lens ($f = 1000$ mm, Thorlabs) was used in the detection beam path to introduce astigmatism for 3D localization. Three emission filters (HC520/35 Semrock, ET600/50 Chroma, ET655 Chroma) were mounted in a PC controlled motorized filter wheel (FW102C, Thorlabs). An emission filter was inserted for fluorescent beads measurements and SMLM measurements. No emission filter was used for the speckle mode.

2.2. Speckle patterns of a cell

Speckle patterns originate from the interference of coherent light showing intensity variations in pronounced features [16]. Such a phenomenon can also be observed when illuminating biological samples [17]. To obtain a speckle pattern of a cell, the optical setup shown in Fig. 1 was used to illuminate a eukaryotic cell.

To acquire a speckle pattern, the emission filter was removed and the backscattered light from the sample was recorded on the camera. An exemplary speckle image is shown in Fig. 2. A complex intensity distribution, formed by the interference of the backscattered laser, can be realized. These speckle patterns are unique, because each of the cells exhibits a huge variety of structural formations. When the sample drifts, the speckle pattern is shifted accordingly and the amount of drift can be estimated with high accuracy using an image registration method [13]. Bright signals, originating from reflected light from the optical elements, can increase the background of the image and reduce the speckle contrast. In most cases, the speckle contrast is sufficiently high to determine reliably the sample drift by image registration.

The speckle size is defined as [18]:

$$d = 2.44 \lambda f_{\#} M \quad (1)$$

where the λ is the wavelength, $f_{\#}$ is the f-number of the lens system and M is the magnification. This relation implicates, that a laser with a longer wavelength produces a speckle pattern with a larger speckle size, which can lower the precision of the image registration.

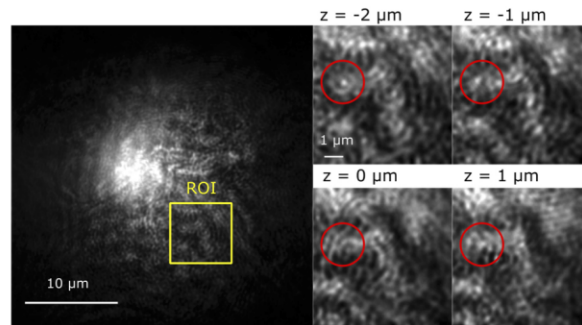


Fig. 2. Speckle pattern of a cell sample. The insets show the ROI at four axial positions ($z = -2 \mu\text{m}$, $-1 \mu\text{m}$, $0 \mu\text{m}$ and $1 \mu\text{m}$). A speckle feature is highlighted by a red circle.

The insets of Fig. 2 show the speckle pattern of the cell sample at four z -positions with a relative axial separation of $1 \mu\text{m}$. A nearly diffraction limited spot indicated with a red circle can be seen at the position of $z = -2 \mu\text{m}$. At the position of $z = -1 \mu\text{m}$ the spot is not visible anymore instead a new spot at a slightly shifted position appeared.

2.3. Drift estimation algorithm

Since each cell exhibits a unique speckle pattern and the speckle patterns vary continuously in z , the speckle patterns can be used as a position reference of the sample in three dimensions. Prior to the drift measurement, a position reference stack containing speckles at different axial planes is recorded. As shown in Fig. 3, a speckle reference z -stack f with n frames and a separation of Δz was acquired at time t_0 , where z represents the axial position of each speckle frame.

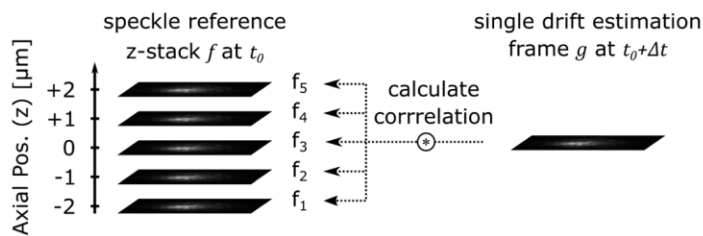


Fig. 3. Scheme for drift estimation. A z -stack of speckle patterns f as a position reference of the cell is acquired. Single drift estimation frames g are captured at regular time intervals during the experiment. By finding the maximum correlation in the speckle reference stack f with g , the drift in x , y and z is estimated.

For drift estimation, single drift estimation frames g were acquired separated in time by Δt . The time separation depends on the SMLM experiment. Each of these images g show a speckle pattern closely corresponding to one present in the speckle reference stack f . Axial and lateral drift is determined by computing the lateral (xy -) maximum of the correlation between g and each frame $f(z)$. The z -position of the speckle reference frame with the highest correlation corresponds to the axial position of the measured drift estimation frame g .

For evaluating the correlation R between g and $f(z)$, we used the DFT method according to [13]. The DFT algorithm returns the image displacement vector $D = [x + \Delta x, y + \Delta y]$ by correlating the single drift estimation frame g with every frame of f :

$$CC_{xy} = \text{DFT}_{xy}^{-1}(\text{DFT}_{xy}(f(z))\text{DFT}_{xy}^*(g)), \quad (2)$$

$$D(z) = \operatorname{argmax}_{xy} |CC_{xy}|. \quad (3)$$

Additionally the DFT algorithm returns the translation invariant normalized root mean square error (RMSE) DFT_{ERROR} between the two images:

$$DFT_{ERROR} = \sqrt{1 - \frac{\max_{xy} |CC_{xy}|^2}{\sum |DFT_{xy}(f(z))|^2 \sum |DFT_{xy}(g)|^2}}. \quad (4)$$

The normalized correlation value is calculated as

$$R_{DFT}(z) = 1 - DFT_{ERROR}(f(z), g). \quad (5)$$

For higher accuracy, an upsampling factor of 100 was used for the DFT and R_{DFT} was interpolated four times along z using cubic spline interpolation. In the following experiments, all data analysis was performed using Matlab R2018b (Mathworks). Since the position of a cell is defined by recording a reference z -stack, a fine step size of the reference stack can encode the detailed speckle patterns. A step size of 10 nm was used to acquire the z -position in the following measurements. The z -position can be estimated precisely by computing the normalized correlation value as shown in Eq. 5.

2.4. Sample preparation

To calibrate the single molecule axial localization based on astigmatism, a sample with fluorescent beads (TetraSpeck 100 nm, ThermoFisher) was prepared. Fluorescent beads were diluted 1:1000 in ddH₂O. The suspension beads solution was sonicated in an ultrasonic bath (EMAG) for 15 min to prevent aggregation. 200 μ l beads solution was applied on a glass bottom 35 mm dish (ibidi) overnight. The dish was washed with ddH₂O water extensively about 10 times to remove mobile beads. After applying 1 ml ddH₂O in the dish, the fluorescent beads sample was used for 3D calibration based on the method [19, 20].

To validate our method, we compared the SMLM localizations with our speckle-based drift estimation on cell samples including fluorescent beads. A sample with fluorescent beads located on the coverslip prior to seeding the cells was prepared as described above. U2OS cells were cultured in a 25 ml culture flask filled with Dulbecco's Modified Eagle's Medium (DMEM, Thermo Fisher) supplemented with 10% fetal bovine serum (FBS, Thermo Fisher) and 1% Penicillin Streptomycin (Pen Strep, Thermo Fisher) in a cell culture incubator (37°C, 5% CO₂). Cells were plated at low confluency on the dish prepared with immobilized beads overnight. Cells were fixed with pre-warmed (37°C) Formaldehyde (4%, Sigma-Aldrich) for 15 min. Afterwards cells were washed three times with Dubecco's Phosphate Buffered Saline (DPBS, Sigma-Aldrich) and the cells were embedded in PBS for imaging.

To image the cell nucleus, the U2OS cells were treated with 0.5% Triton X-100 in DPBS for 10 min and washed with DPBS. Cells were incubated at 37 °C with 1:1000 RNase A cocktail (Thermo Fisher) in DPBS for 15 min. Cells were washed with DPBS and nuclei were stained with 0.05 μ M SytoxOrange in PBS (Thermo Fisher) for 30 min. A typical imaging buffer with an enzymatic oxygen scavenging system was prepared for fBALM [21]. The buffer contained 10% glucose (Sigma-Aldrich), 5 mg/ml glucose oxidase from aspergillus niger (Sigma-Aldrich), 500 μ g/ml catalase from bovine liver (Sigma-Aldrich) in DPBS.

2.5. Determination of 3D positions of fluorescent beads

To determine the 3D position information of fluorescent beads from a 2D image, a cylindrical lens was inserted in the detection beam path of the optical setup to deform the point spread function (PSF) to an elliptical shape with increasing defocus [19,20]. To derive the axial position of the fluorescent beads, a calibration of the setup is necessary. For this calibration, a z -stack

with an axial range from -400 nm to 400 nm and a step size of 10 nm of the 3D PSFs of three fluorescent beads in the center of the field of view was recorded. This image stack was processed using ThunderSTORM to acquire the 3D calibration curve [22]. The calibration curve was used to determine the 3D position of fluorescent beads from 2D images using ThunderSTORM.

2.6. Drift estimation routine for SMLM imaging

To demonstrate the drift correction method based on speckle patterns for SMLM measurements, an experimental flow chart is presented in Fig. 4. Before the SMLM measurement, the focal position of the cell Pos_{center} and the beads Pos_{beads} were identified. For the speckle-based method, no emission filter was inserted and a reference z-stack at Pos_{center} was acquired.

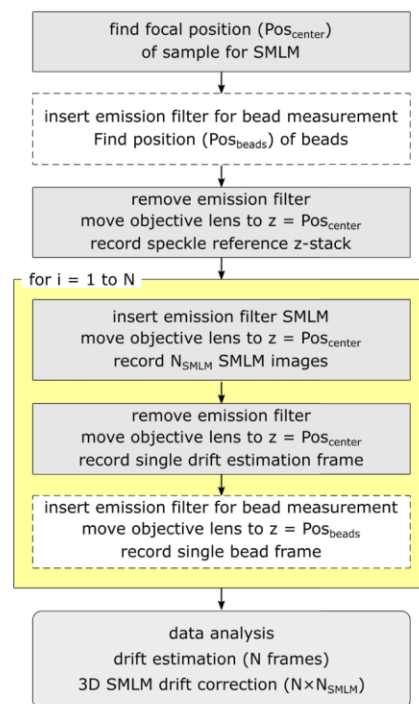


Fig. 4. Flow chart of 3D SMLM experiment with speckle- and beads-based drift estimation methods. The dashed boxes are optional and are only used for comparison measurements.

In the next step, we acquired N_{SMLM} images at position Pos_{center} with an emission filter inserted into the detection beam path. Afterwards, a single drift frame was acquired at position Pos_{center} without an emission filter. Then a single bead frame was acquired at position Pos_{beads} with an emission filter. This measurement procedure of the last three steps is an N times routine and can be defined according to requirements of the user. The amount of drift determined by both methods were analyzed according to Section 2.3 and Section 2.5. The results of the drift estimation method based on the speckle method were interpolated to the number of total frames $N \times N_{SMLM}$ of the SMLM measurement using spline interpolation. The positions of the localized molecules were then corrected according to the drift.

Alternatively, the experiment can be performed using a single laser. For speckle illumination, the emission filter is removed and the laser power is reduced to prevent overexposure of the camera. For SMLM, the emission filter is inserted and the laser illumination intensity is increased to achieve appropriate blinking of molecules. The operation duration to insert a filter takes

about 3 to 4 seconds using the default setting of the filter wheel. A shorter operation time can be achieved using the fast mode, or reducing the pause time or customization of in the routine setting of the filter wheel, or using a second camera and ND-filters or weak reflections for speckle-based drift estimation. Because the intensity of the speckle pattern is much higher than the intensity of the fluorescent emission of the excited fluorophores, the blinking emission does not influence the accuracy of the image registration.

3. Drift estimation experiments

Two different experiments were performed to show the performance of the drift estimation algorithm. One experiment was done on a short time scale to show the typical characteristics of the proposed correlation method. The other experiment was performed on a long time scale to compare the results of our methods with the drift estimation method using fluorescent beads.

3.1. Simulated drift using a cell sample

The sample (U2OS cells) was illuminated using the 488 nm laser with a power of 0.01 mW (1.4 W/cm^2) in the speckle mode. A speckle reference z-stack f_{exp1} with a range of 10 μm and a step size of 10 nm was acquired with a camera exposure of 5 ms. To demonstrate the correlation of speckle patterns, a second stack g_{exp1} of speckle images representing simulated drift estimation frames at 27 axial positions starting at $-2.75 \mu\text{m}$ with a step size of 250 nm was recorded immediately after the first stack with the same exposure time and laser power.

3.2. Cell sample with fluorescent beads

To validate our method, the sample (U2OS cells with fluorescent beads) was imaged sequentially between the method based on speckle patterns and the fluorescent beads method. At each of the measurements, we acquired an image showing a speckle pattern and sequentially another image showing beads by immediately inserting the emission filter using the filter wheel. The switching time between the image acquisitions was about 2 seconds. We analyzed the positions between the two methods.

To acquire speckle patterns, the power of the laser with a wavelength of 488 nm was set to 0.01 mW (1.4 W/cm^2) and 10 ms exposure to record a reference stack spanning 500 nm at a step size of 10 nm. The 488 nm laser corresponding to an irradiance ($8 \text{ mW} \sim 1 \text{ kW/cm}^2$) was used to acquire fluorescence of the beads with a camera exposure of 100 ms.

The drift estimation based on speckle patterns was analyzed according to Section 2.3. The 3D positions of three fluorescent beads were determined using ThunderSTORM. The analysis is shown in a time trace and a comparison of the results is presented in Section 4.3.

3.3. Drift correction for SMLM of nuclear structure

For the demonstration of the speckle-based method used for imaging chromatin structures, the speckle images were acquired using the same setting described in Section 3.2. For imaging beads as a comparison experiment, the laser with a wavelength of 647 nm (8 mW , $\sim 1 \text{ kW/cm}^2$) and a camera exposure of 30 ms were used. The emission filter LP655 was selected. Four fluorescent beads were analyzed using ThunderSTORM.

For SMLM imaging, the drift estimation routine described in Section 2.6 was utilized. Prior to the acquisition routine, a reference z-stack with an axial range of 410 nm and a step size of 10 nm was acquired using the laser with a wavelength of 488 nm. For the super-resolution imaging of the chromatin structure, the laser with a wavelength of 561 nm (14 mW , $\sim 1 \text{ kW/cm}^2$) was used to induce blinking events. Twenty subsets of 500 images were acquired and the localized molecules were analyzed using ThunderSTORM.

4. Results

4.1. Experimental result of the simulated drift using a cell sample

To validate our drift estimation method, we performed an experiment with the U2OS cells sample without fluorescent beads. Figure 5 shows a typical curve of the correlation between $g_{exp1}(z = 0)$ and each frame of f_{exp1} yielding a clear maximum, which represents an estimation of the z position of the sample. Since Fig. 5 was based on data acquired immediately after recording the reference stack, almost no drift was present and therefore the maximum is as expected close to the position $z = 0$.

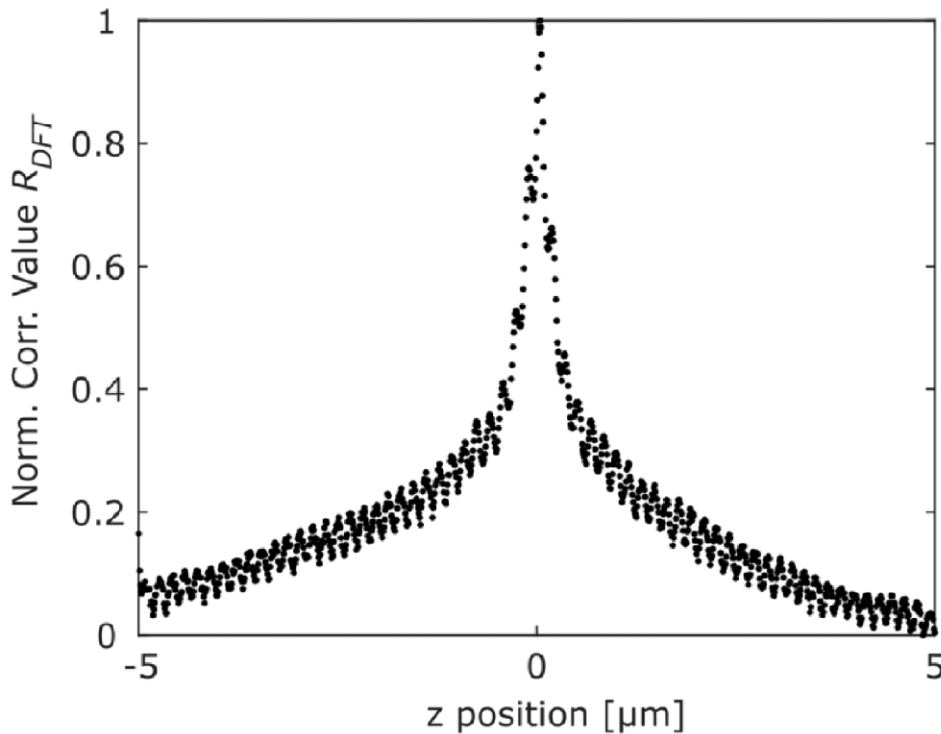


Fig. 5. Correlation (normalized to a maximum of one) between the drift estimation frame $g_{exp1}(z = 0)$ and each image of the speckle reference z -stack f obtained from measured data.

To evaluate our speckle-based method for larger drifts, all frames of g_{exp1} were correlated with f_{exp1} and the z position of the maximum correlation was determined. Since the axial position of every frame of g_{exp1} is known and the drift of the setup can be neglected, a linear dependency can be found between the axial positions versus the position determined by our drift estimation algorithm as shown in Fig. 6(a). The residuals after linear regression are shown in Fig. 6(b) yielding a standard deviation of 2 nm, indicating that the proposed drift correction method can robustly correct simulated drift with high accuracy.

4.2. Repeatability of the drift estimation

The repeatability of the drift estimation was investigated by acquiring speckle patterns continuously for 10 seconds at the same position, assuming no drift happened during this image acquisition. A stack of 1000 images (10 ms per frame) was captured and the stack of speckle patterns was then analyzed using the method described in Section 2.3. As shown in Fig. 7, the standard deviation

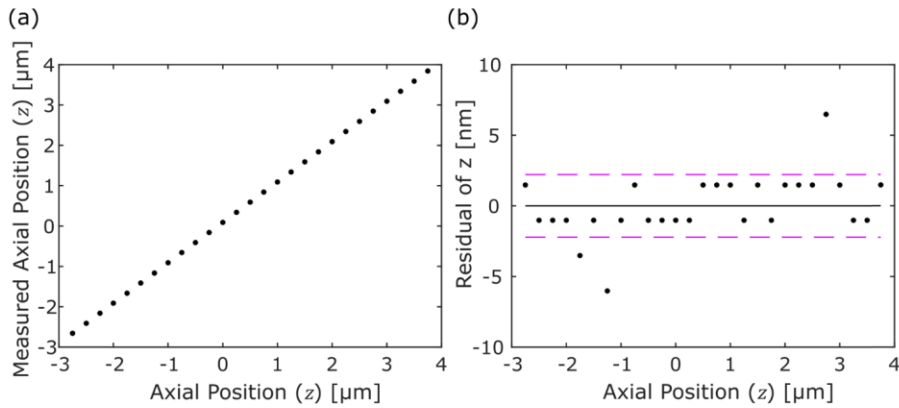


Fig. 6. Speckle based z-position estimation by a defined z-position with a range of $7\ \mu\text{m}$ and a $250\ \text{nm}$ step size. (a) Measured z-position. (b) Residuals of the linear regression.

of the repeatability of the speckle-based drift estimation in axial position are $3.0\ \text{nm}$ and $1.5\ \text{nm}$ in the x-axis and $2.2\ \text{nm}$ in the y-axis. In Fig. 7(a), a peak at one second with a z-drift of $16\ \text{nm}$ can be seen. This may be attributed to environmental conditions such as airflow or a small vibration of the optical table.

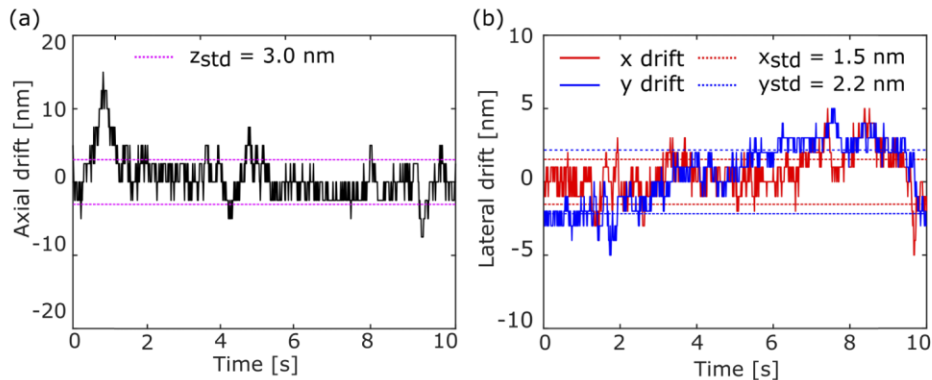


Fig. 7. The repeatability of the speckle-based drift estimation method for 10 seconds in (a) optical axis (z) and (b) lateral axes (x,y).

4.3. Experimental results of the cell sample with fluorescent beads

To validate our method for a practical drift situation, we compared the speckle-based method and the localized positions of fluorescent beads. The images of fluorescent beads can be considered as single emitters shown in the raw images of SMLM measurements. The experiment was performed as shown in the flow chart in Fig. 4 without the SMLM image acquisition. We acquired pairs of images showing speckles and fluorescent beads every 20 seconds in a period of 10 minutes. An exemplary speckle image is shown in Fig. 8(a). Three fluorescent beads as indicated in the ROI of Fig. 8(b) were used for the analysis.

The comparison of the two drift estimation methods is shown in Fig. 9. Figure 9(a) shows the axial drift determined by evaluating the fluorescent beads and by using our drift estimation method. A steady drift of $100\ \text{nm}$ could be seen in the first 5 minutes. After 5 minutes, the system does not exhibit a noticeable drift. The shaded range of $5.4\ \text{nm}$ is given by the averaged

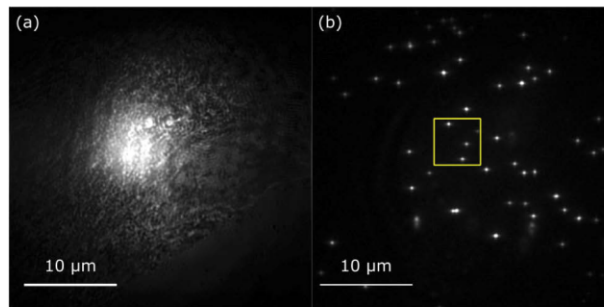


Fig. 8. An experimental result of the sample drift measurement. A pair of image with (a) a speckle pattern and (b) fluorescent beads.

standard deviation of all bead localizations and the results of both methods correspond closely. We defined the localization-based fluorescent bead method as the references and compared it with the results based on the speckle image correlation. The axial position difference between both methods is shown in Fig. 9(b) with a standard deviation of ± 9.4 nm. Although this value is good enough for SMLM experiments, it also indicates that the estimate of 2 nm precision as obtained from Fig. 6 may be overly optimistic.

A similar analysis was applied to determine the lateral drift in x and y and the results are shown in Fig. 9(c). The measurement shows that the microscope system has a gradual drift of about 150 nm in 10 minutes in the x direction. A small drift of the system in the order of tens of nanometers can be seen in the y direction. The shaded area indicates the average standard deviation of the bead measurement of ± 1.7 nm and ± 3.7 nm in x and y , respectively. The results of the differences between the two methods in x and y are shown in Fig. 9(d) with a standard deviation of ± 6.4 nm and ± 8.2 nm in x and y , respectively.

The results of the lateral and axial drift using speckle image correlation show a good agreement with the results using fluorescent beads. The small deviation between the two methods can be explained by small disturbances introduced by the rotation of the filter wheel. The repeatability of the drift estimation as shown in Fig. 7 caused by environmental conditions could lead to also this small deviation. Both methods have several nanometer precision but our speckle pattern image registration method does not require additional sample preparation and is highly applicable for SMLM measurements.

4.4. Drift correction for 3D SMLM

Nuclei labeled with the DNA dye SytoxOrange were used to demonstrate the speckle-based drift correction. Fluorescent beads were prepared additionally in the dish for a comparison measurement. The results of the drift estimation comparison between the two methods is shown in Fig. 10. The drift estimations in three dimensions show a good agreement between the two methods. A lower precision of the fluorescent beads compared with the results shown in the Fig. 9 can be attributed to a lower intensity of the fluorescent beads in the sample.

Figure 11 reveals nuclear genome architecture with small nucleosome domain clusters. Similar patterns were realized in [21,23]. As shown in the inset of Fig. 11, before correction, the nucleosome domain cluster shown in the center appears to be distributed spatially in a broad range along the axial direction. Whereas, after drift correction, a much smaller distribution of the nucleosome cluster can be observed as indicated by the reduced color distribution. The proposed drift correction method may support biological studies of nuclear genome architecture for a better quantification of the chromatin nano-organization inside the nucleus.

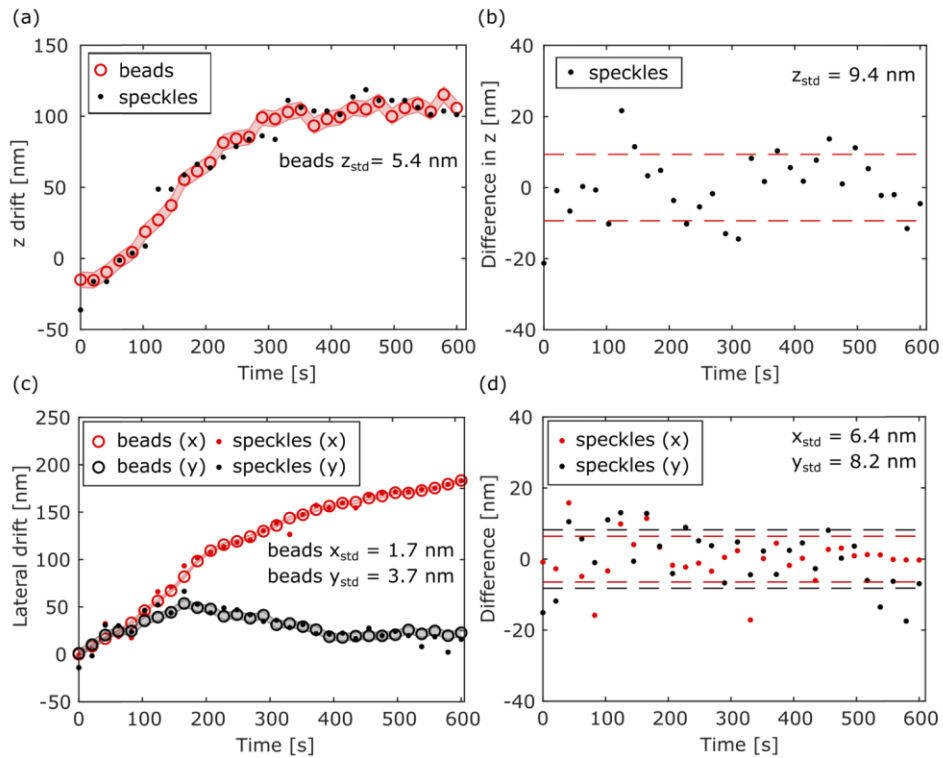


Fig. 9. Time dependent measurement for comparing the drift estimation between fluorescent beads and our speckle-based method. The sample was illuminated by the laser with a wavelength of 488 nm. (a,c) Axial and lateral drift measurements. The shaded areas are given by the averaged standard deviation of all bead localizations. (b,d) Difference between beads- and speckle-based drift estimation in axial and in lateral direction. The dashed lines indicate the standard deviation.

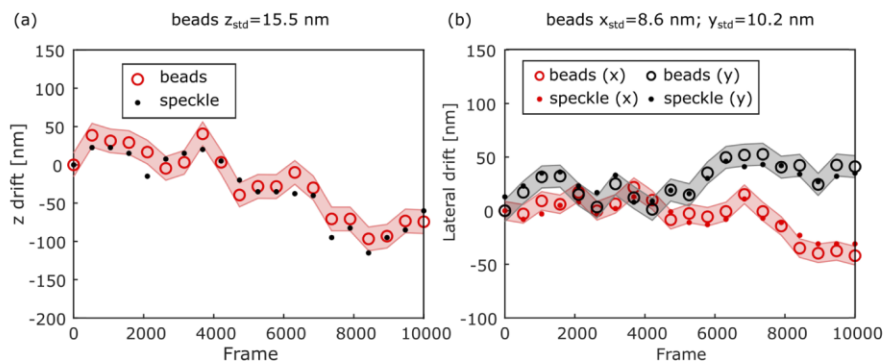


Fig. 10. Time dependent measurement for comparing the drift estimation between fluorescent beads and our speckle-based method in a 3D SMLM experiment. For the speckle-based method, the laser with a wavelength of 488 nm was used to illuminate the sample; and the laser with a wavelength of 647 nm was used to excite the fluorescence beads. (a) Axial and (b) lateral drift measurements for x and y separately. The shaded areas are given by the averaged standard deviation of all bead localizations.

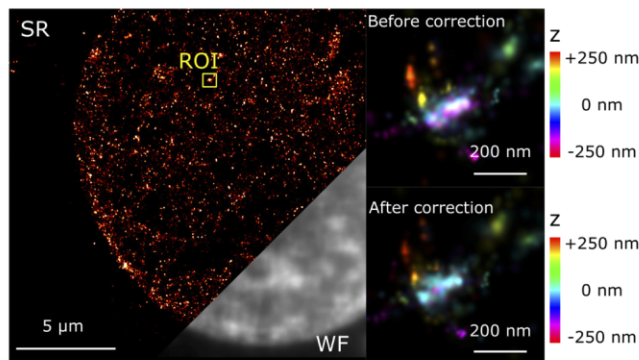


Fig. 11. The intensity sum projection of the drift corrected 3D SMLM image of a nucleus labeled with the DNA dye SytoxOrange [23], excited by the laser with a wavelength of 561 nm. Inset: color-coded maximum intensity projection before and after correction. The color scale indicates the z position.

5. Conclusion

We presented a three-dimensional drift estimation method for SMLM, based on speckle image correlation. We used low laser power to illuminate eukaryotic cell samples and image the backscattered laser light showing distinct speckle patterns. Because the structure of cells is unique, this method provides straightforward three-dimensional spatial information of the sample, which can be used for high-resolution drift estimation.

This method is expected to be especially useful in long term, high precision 3D SMLM measurements such as biological studies of nuclear genome architecture [24,25], because no fluorescent signals are required and the illumination power is kept low. Without additional sample preparation, sufficient blinking data points from SMLM measurements or advanced modification of the microscope setup, this method results in a highly precise drift estimation comparable with a fiducial markers approach. This method also provides an alternative drift correction approach for microscope systems equipped only with a single laser.

In this report, we demonstrated a speckle-based drift correction method for use in 3D SMLM in three dimensions. In the future, we plan to implement a second camera monitoring the speckle pattern during the SMLM image acquisition. The speckle-based method, especially when combined with a feedback mechanism, is expected to also find numerous applications in other imaging modes that need to keep the focus stable. If combined with a precise XY stage control, it can also serve to avoid lateral drifts during imaging. We expect that this method provides an alternative solution for highly precise drift correction in three dimensions in real time.

Funding

Boehringer Ingelheim Stiftung, Mainz/Germany; International PhD Programme on Gene Regulation, Epigenetics & Genome Stability, Mainz/Germany.

Acknowledgment

The authors thank the microscope core facility of the IMB for providing U2OS cells for the measurements, the electronic and the mechanic workshop for manufacturing electronic boards and mechanic elements. Dr. Sandra Ritz and Dr. Márton Gelléri helped proof reading of the manuscript. R.H. acknowledges funding by the Deutsche Forschungsgemeinschaft (DFG)

via SFB TR166 “Receptorlight”, TP A4 and the Collaborative Research Center SFB 1278 (PolyTarget, project C04).

Disclosures

The authors declare that there are no conflicts of interest related to this article.

References

1. M. J. Rust, M. Bates, and X. Zhuang, “Sub-diffraction-limit imaging by stochastic optical reconstruction microscopy (STORM),” *Nat. Methods* **3**(10), 793–796 (2006).
2. E. Betzig, G. H. Patterson, R. Sougrat, O. W. Lindwasser, S. Olenych, J. S. Bonifacino, M. W. Davidson, J. Lippincott-Schwartz, and H. F. Hess, “Imaging Intracellular Fluorescent Proteins at Nanometer Resolution,” *Science* **313**(5793), 1642–1645 (2006).
3. P. Lemmer, M. Gunkel, D. Baddeley, R. Kaufmann, A. Urich, Y. Weiland, J. Reymann, P. Müller, M. Hausmann, and C. Cremer, “SPDM: light microscopy with single-molecule resolution at the nanoscale,” *Appl. Phys. B: Lasers Opt.* **93**(1), 1–12 (2008).
4. C. Cremer and B. R. Masters, “Resolution enhancement techniques in microscopy,” *Eur. Phys. J. H* **38**(3), 281–344 (2013).
5. M. J. Mlodzianowski, J. M. Schreiner, S. P. Callahan, K. Smolková, A. Dlasková, J. Šantorová, P. Ježek, and J. Bewersdorf, “Sample drift correction in 3D fluorescence photoactivation localization microscopy,” *Opt. Express* **19**(16), 15009–15019 (2011).
6. Y. Wang, J. Schnitzbauer, Z. Hu, X. Li, Y. Cheng, Z.-L. Huang, and B. Huang, “Localization events-based sample drift correction for localization microscopy with redundant cross-correlation algorithm,” *Opt. Express* **22**(13), 15982–15991 (2014).
7. R. Han, L. Wang, F. Xu, Y. Zhang, M. Zhang, Z. Liu, F. Ren, and F. Zhang, “Drift correction for single-molecule imaging by molecular constraint field, a distance minimum metric,” *BMC Biophys.* **8**(1), 1–14 (2015).
8. S. H. Lee, M. Baday, M. Tjioe, P. D. Simonson, R. Zhang, E. Cai, and P. R. Selvin, “Using fixed fiducial markers for stage drift correction,” *Opt. Express* **20**(11), 12177–12183 (2012).
9. H. Ma, J. Xu, J. Jin, Y. Huang, and Y. Liu, “A simple marker-assisted 3D nanometer drift correction method for superresolution microscopy,” *Biophys. J.* **112**(10), 2196–2208 (2017).
10. A. Balinovic, D. Albrecht, and U. Endesfelder, “Spectrally red-shifted fluorescent fiducial markers for optimal drift correction in localization microscopy,” *J. Phys. D: Appl. Phys.* **52**(20), 204002 (2019).
11. Y. Youn, Y. Ishitsuka, C. Jin, and P. R. Selvin, “Thermal nanoimprint lithography for drift correction in super-resolution fluorescence microscopy,” *Opt. Express* **26**(2), 1670–1680 (2018).
12. S. A. Jones, S. H. Shim, J. He, and X. Zhuang, “Fast, three-dimensional super-resolution imaging of live cells,” *Nat. Methods* **8**(6), 499–505 (2011).
13. M. Guizar-Sicairos, S. T. Thurman, and J. R. Fienup, “Efficient subpixel image registration algorithms,” *Opt. Lett.* **33**(2), 156–158 (2008).
14. R. McGorty, D. Kamiyama, and B. Huang, “Active microscope stabilization in three dimensions using image correlation,” *Opt. Nanoscopy* **2**(1), 3–7 (2013).
15. S.-Y. Chen, F. Bestvater, W. Schaufler, R. Heintzmann, and C. Cremer, “Patterned illumination single molecule localization microscopy (piSMLM): user defined blinking regions of interest,” *Opt. Express* **26**(23), 30009–30020 (2018).
16. J. W. Goodman, “Some fundamental properties of speckle*,” *J. Opt. Soc. Am.* **66**(11), 1145–1150 (1976).
17. J. B. Pawley, *Handbook of Biological Confocal Microscopy* (Springer, 2006), Chap. 9.
18. M. Draijer, E. Hondebrink, T. van Leeuwen, and W. Steenbergen, “Review of laser speckle contrast techniques for visualizing tissue perfusion,” *Lasers Med. Sci.* **24**(4), 639–651 (2009).
19. B. Huang, W. Wang, M. Bates, and X. Zhuang, “Three-dimensional super-resolution imaging by stochastic optical reconstruction microscopy,” *Science* **319**(5864), 810–813 (2008).
20. H. P. Kao and A. S. Verkman, “Tracking of single fluorescent particles in three dimensions: use of cylindrical optics to encode particle position,” *Biophys. J.* **67**(3), 1291–1300 (1994).
21. A. Szczyrek, L. Klewes, J. Xing, A. Gourram, U. Birk, H. Knecht, J. W. Dobrucki, S. Mai, and C. Cremer, “Imaging chromatin nanostructure with binding-activated localization microscopy based on DNA structure fluctuations,” *Nucleic Acids Res.* **45**(8), e56 (2017).
22. M. Ovesný, P. Křížek, J. Borkovec, Z. Švindrych, and G. M. Hagen, “ThunderSTORM: a comprehensive ImageJ plug-in for PALM and STORM data analysis and super-resolution imaging,” *Bioinformatics* **30**(16), 2389–2390 (2014).
23. A. Szczyrek, U. Birk, H. Knecht, J. Dobrucki, S. Mai, and C. Cremer, “Super-resolution binding activated localization microscopy through reversible change of DNA conformation,” *Nucleus* **9**(1), 182–189 (2018).
24. T. Cremer, M. Cremer, B. Hübner, H. Strickfaden, D. Smeets, J. Popken, M. Sterr, Y. Markaki, K. Rippe, and C. Cremer, “The 4D nucleome: Evidence for a dynamic nuclear landscape based on co-aligned active and inactive nuclear compartments,” *FEBS Lett.* **589**(20 PartA), 2931–2943 (2015).

25. T. Cremer and C. Cremer, "Chromosome territories, nuclear architecture and gene regulation in mammalian cells," *Nat. Rev. Genet.* **2**(4), 292–301 (2001).

Publication 2

[SC2] Patterned illumination single molecule localization microscopy (piSMLM): user defined blinking regions of interest

Shih-Ya Chen, Felix Bestvater, Wladimir Schaufler, Rainer Heintzmann, and Christoph Cremer

Opt. Express, 26(23), 30009-30020 (2018)

DOI: <https://doi.org/10.1364/OE.26.030009>

Author	Shih-Ya Chen
Conceptual research design	x
Plan of research activities	x
Data collection	x
Data analyses and interpretation	x
Manuscript writing	x
Suggested publication equivalence value	1.0

This paper is published by The Optical Society under the terms of the Creative Commons [Attribution 4.0 License](https://creativecommons.org/licenses/by/4.0/). No reprinted permission is required.

Patterned illumination single molecule localization microscopy (piSMLM): user defined blinking regions of interest

SHIH-YA CHEN,¹ FELIX BESTVATER,² WLADIMIR SCHAUFLENER,^{2,3} RAINER HEINTZMANN,^{4,5} AND CHRISTOPH CREMER^{1,3,6,*}

¹Institute of Molecular Biology, Mainz 55128, Germany

²German Cancer Research Center, Im Neuenheimer Feld 280, 69120 Heidelberg, Germany

³Institute of Pharmacy and Molecular Biotechnology (IPMB), Heidelberg University, 69120, Germany

⁴Institute of Physical Chemistry and Abbe Center of Photonics, Friedrich Schiller University Jena, 07743, Germany

⁵Leibniz Institute of Photonic Technology, Jena 07745, Germany

⁶Physics Department University of Mainz (JGU), Mainz 55128, Germany

*c.cremer@imb-mainz.de

Abstract: Single molecule localization microscopy (SMLM) has been established as an important super-resolution technique for studying subcellular structures with a resolution down to a lateral scale of 10 nm. Usually samples are illuminated with a Gaussian shaped beam and consequently insufficient irradiance on the periphery of the illuminated region leads to artifacts in the reconstructed image which degrades image quality. We present a newly developed patterned illumination SMLM (piSMLM) to overcome the problem of uneven illumination by computer-generated holography. By utilizing a phase-only spatial light modulator (SLM) in combination with a modified Gerchberg-Saxton algorithm, a user-defined pattern with homogeneous and nearly speckle-free illumination is obtained. Our experimental results show that irradiance 1 to 5 kW/cm² was achieved by using a laser with an output power of 200 mW in a region of 2000 μm² to 500 μm², respectively. Higher irradiance of up to 20 kW/cm² can be reached by simply reducing the size of the region of interest (ROI). To demonstrate the application of the piSMLM, nuclear structures were imaged based on fluctuation binding-activated localization microscopy (fBALM). The super-resolution fBALM images revealed nuclear structures at a nanometer scale.

Published by The Optical Society under the terms of the [Creative Commons Attribution 4.0 License](https://creativecommons.org/licenses/by/4.0/). Further distribution of this work must maintain attribution to the author(s) and the published article's title, journal citation, and DOI.

1. Introduction

Fluorescence microscopy is an important tool for studying a variety of questions in biology. Cellular organelles exhibit very complex molecular structures on different scales, from a few micrometers down to several nanometers. However, fine structures of cell organelles below the optical resolution limit are not observable. The super-resolution method Single Molecule Localization Microscopy (SMLM) was developed to overcome the resolution barrier. The first 'pointillism' method of SMLM was demonstrated by imaging blinking quantum dots (QDs) as light emitters [1]. The QDs signals were distinguished with the help of independent component analysis based on statistical blinking of QDs. This 'pointillism' technique opened avenues to study cellular structure by using photo-switchable fluorophores for biological samples [2–4]. In order to photoactivate or recover fluorophores, such fluorescence microscopes are typically equipped with lasers, which normally have Gaussian irradiance profiles. However, the disadvantage of Gaussian illumination for SMLM is the introduction of uneven illumination in the sample. Depending on the irradiance distribution of the Gaussian illumination, different amounts of fluorescence photons are emitted, which can lead to a higher localization precision in the center region of the Gaussian illumination spot relatively to the outside region [5].

Moreover, molecules in low irradiance areas show a longer on-state, resulting in many overlapping emitters, which introduces artifacts in the reconstructed super-resolution image, thus hampering the quantitative evaluation based on the intensity distribution [6]. Several approaches have been proposed to overcome the inhomogeneity problem over the full field of view. One method to create a flat-top illumination is to insert two micro lens arrays for creating ray bundles. The ray bundles propagate and overlap in the sample plane resulting in a homogenous illumination [7]. Another approach is to use a laser which is coupled into a multimode fiber [8]. The disadvantage of both of these methods is the requirement of fast spatial dithering (e.g. by a rotating diffuser) to eliminate non-uniformities. Some other methods utilize a beam-shaper to convert a Gaussian beam into a flat-top irradiance distribution [9,10]. However, a beam-shaper is commonly designed to generate a circular laser spot, which limits the field of view to a circular illumination area. Additionally, all of the above mentioned methods are limited to a certain shape of illumination and changing the shape requires special design and additional optical components.

To overcome the limitations of current SMLM, we developed a patterned illumination technique for wide-field fluorescence microscopy based on computer-generated holography. By utilizing a phase-only spatial light modulator (SLM) in combination with a Gerchberg-Saxton algorithm (GS) [11], one has the possibility to define arbitrary patterns as regions of interest (ROIs). In order to achieve flat-top illumination with arbitrary desired shapes, we propose a calibration method which can eliminate a slight misalignment or laser induced inhomogeneous illumination by modifying the standard GS algorithm.

In this method, the superposition of a Fresnel lens and the phase mask calculated by our modified GS algorithm separates the pattern from the undesirable zeroth diffraction order, resulting in a high contrast image. Because of the light redistribution in the phase-only SLM, low power losses can be achieved. The advantage of this technique is that the total power in the sample is independent of the size of the illumination pattern. By reducing the ROI, higher irradiance can be achieved. In contrast to our method, placing a modulator in the image plane to define a ROI to achieve patterned illumination by a digital micro-mirror device (DMD) exhibits a linear dependency on the size of the illumination area [12,13]. Therefore, higher illumination irradiance can only be obtained by increasing the laser power. Furthermore, without introducing an additional device to reduce laser speckles in the sample, the time-averaging method was implemented in the software of piSMLM [14–16]. To demonstrate the capability of piSMLM, we first show the influence of non-uniform illumination in wide-field fluorescence microscopy by comparing images of cell nuclei excited by Gaussian illumination with flat-top illumination. Additionally, we show the possibility for user-defined ROIs with high illumination intensities to achieve SMLM super-resolution image.

2. Patterned illumination single molecule localization microscopy setup

2.1 Excitation beam path

A custom-made inverted fluorescence microscope was designed and set up for patterned illumination single molecule localization microscopy. The scheme of the setup is shown in Fig. 1. The microscope was equipped with a 488 nm (Omicron, Germany), a 561 nm (Frankfurt Laser, Germany) and a 647 nm (Cobolt, Sweden) laser with 200 mW, 200 mW and 120 mW of the maximum output power, respectively. The three lasers were combined with dichromatic reflectors D1 and D2. By switching the flip-mirrors M5 and M8, the illumination mode could be chosen between Gaussian illumination and the patterned illumination mode.

Gaussian illumination mode: The laser was expanded by a pair of lenses L1 and L2 ($f = 30$ mm, $f = 60$ mm) and focused at the back focal plane of the objective lens (HCX PL APO 100 \times /NA 1.47 OIL, Leica, Germany) by a tube lens L9 ($f = 125$ mm). The quadband dichroic mirror D3 (ZT405/488/561/647rpc, Chroma Technology) was used to reflect the laser and to transmit emitted fluorescence light from the sample. In this setup, a Gaussian irradiance

distribution with a full width at half maximum (FWHM) of $50\ \mu\text{m}$ was created in the focal plane of the objective lens.

Patterned illumination mode: The laser was expanded by a pair of lenses L3 and L4 ($f = 10\ \text{mm}$, $f = 100\ \text{mm}$) to match the size of the LCoS SLM (Pluto, Holoeye, Germany). The polarization state of the expanded beam was aligned by a lambda half waveplate to match the modulation axis of the liquid crystal layer of the SLM. The phase distribution of the desired intensity pattern was calculated using a modified Gerchberg-Saxton (GS) algorithm.

Elimination of zeroth diffraction order: A typical problem seen in SLM systems is the presence of the zeroth order of unshaped diffracted light reflected by the SLM. This results in a bright spot superimposed on the desired intensity pattern. A common method to separate this zeroth order and the desired intensity pattern is to add the phase function of a blazed phase grating to tilt the diffracted light from on-axis to off-axis [17]. However, the spatial separation of the desired intensity pattern and the zeroth order requires an off axis propagation of the zeroth order through the optical system, which results in a slightly anisotropic pixel pitch. Another disadvantage is the dispersion introduced by the grating structure resulting in different diffraction angles for the aligned lasers. Another approach to separate the zeroth order and the desired intensity pattern is to superimpose a Fresnel lens on the phase function [18]. Using this method, the desired intensity pattern and the diffraction-limited spot of the non-diffracted light can be slightly separated along the optical axis. By placing a blocker at the position of the zeroth order spot, this spot can be filtered out. However, the axial separation of the desired intensity pattern and the zeroth order blocker is relatively small. The blocker can remove a severe amount of the desired intensity pattern as well.

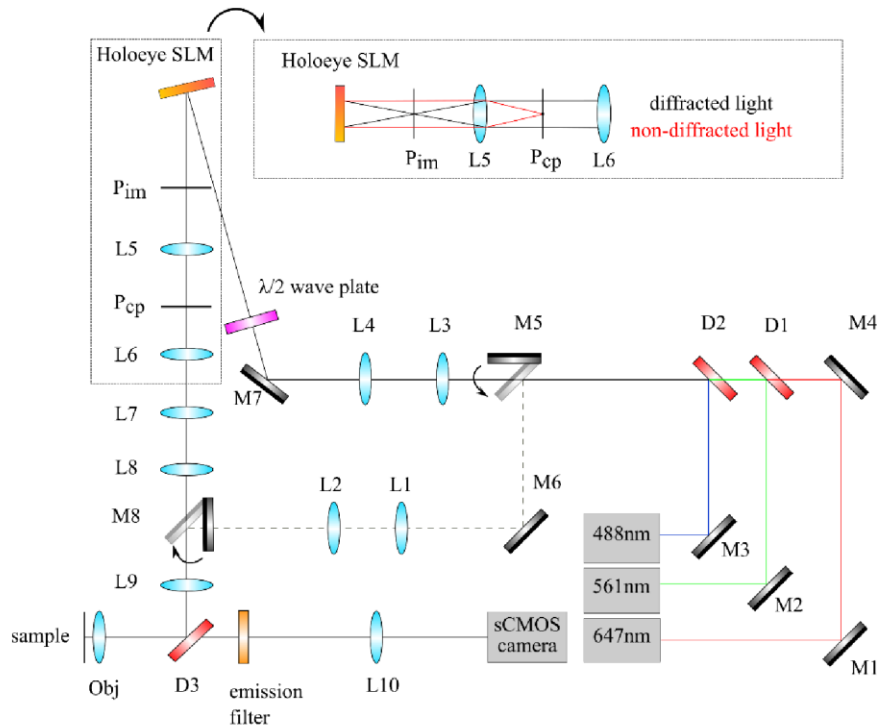


Fig. 1. Patterned illumination single molecule localization microscopy (piSMLM) setup. The inset shows the ray paths of diffracted and non-diffracted light at the SLM, which demonstrates an optimal separation between the desired pattern and the zeroth order originating from the non-diffracted light.

In our piSMLM setup, we utilized the superposition of the phase distribution calculated by the modified GS algorithm and the phase of a Fresnel lens with a focal length of 110 mm to form an on-axis image at the position P_{im} (see Fig. 1). This image revealed a very uniform background because of the non-diffracted light. Using lens L5, this image was Fourier-transformed into the conjugated pupil plane located at the position P_{cp} . The fine structures of the image were represented by higher frequencies in the conjugated pupil plane. The background due to the non-diffracted light would form a diffraction-limited spot in the center of the conjugated pupil plane. A coverslip with a small central stop was used to filter the non-diffracted light. This high-pass filter had a minimal influence on the higher frequencies of the desired intensity pattern. The filtered low frequencies had minimal impact on the final image. With the lenses L6 ($f = 35$ mm), L7 ($f = 125$ mm), L8 ($f = 200$ mm) and L9 ($f = 125$ mm) the conjugated pupil plane was relayed to the pupil of the objective lens.

Suppression of laser speckles: Another common problem regarding the GS algorithm is the appearance of speckles. To address this issue, a sequence of phase masks with initial random phases was calculated. Because the initial phase is random, every single desired intensity pattern exhibits a unique speckle pattern. By recording multiple fluorescence images with different speckle patterns and averaging the intensities, an almost speckle-free intensity pattern was obtained [14–16].

Flat-Top Illumination: The almost speckle-free averaged intensity pattern with low speckle noise can still show an inhomogeneous intensity distribution over the entire field of view. Several factors can be the reason for this non-uniformity: aberrations due to slight misalignment in the excitation beam path; the influence of the zeroth order blocker; inhomogeneous illumination of the SLM, i.e. by a Gaussian laser beam or the limitation of the convergent iterative process of the standard GS algorithm. To correct for these effects to obtain a flat-top illumination, a modified GS algorithm is presented in Fig. 2.

The standard GS algorithm was extended by introducing a calibration image which weights the target intensity pattern to correct the non-uniformity. The weighting of the target intensity is achieved by dividing element-wise the target intensity pattern by the normalized calibration image. A detailed description how to measure the calibration image is given in section 3.1. A MATLAB GUI interface (Matlab 2014b, Mathworks) was used to define the desired intensity patterns and the phase patterns were calculated using a GPU accelerated Matlab script.

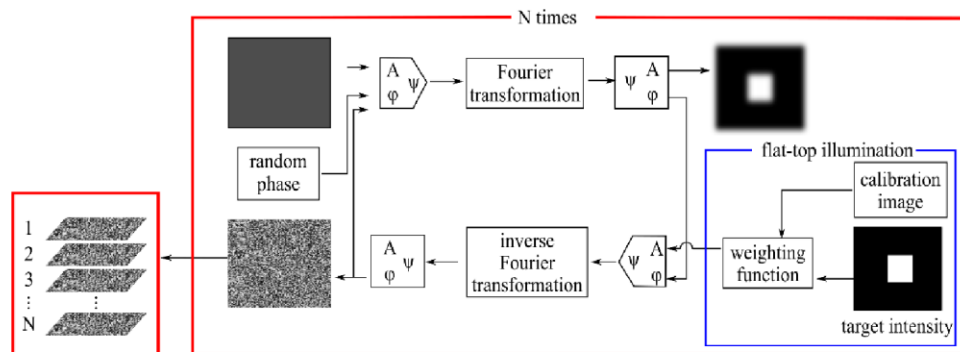


Fig. 2. Flow chart of the modified Gerchberg-Saxton algorithm with wave function ψ , amplitude A and phase ϕ . The target intensity is weighted by a measured calibration image as a new input intensity to achieve flat-top illumination (blue). Multiple phase masks are generated to remove speckles by the time-averaging method (red).

2.2 Detection beam path

Fluorescence was collected by the objective lens and was separated from the excitation laser by the dichromatic beamsplitter D3. Emission filters (HC609/54, HC520/35, Semrock, ET525/50, ET600/50, ET655, Chroma Technology) were mounted in a motorized filter wheel

(FW102C, Thorlabs). The emission light was focused by a tube lens ($f = 200$ mm) and imaged on a sCMOS camera (PCO edge 4.2) with a pixel size corresponding to 65 nm in the sample plane.

3. Experimental results and discussion

3.1 Homogeneously patterned illumination

In the first step, a calibration image for characterizing and correcting the non-uniform illumination was recorded by defining the whole field of view as the desired illumination pattern. Forty corresponding phase masks were calculated using the standard GS algorithm with 20 iterations. After averaging the intensity of the 40 recorded illumination patterns, the image was smoothed with a disk-filter (circular averaging filter) with the size of 30 pixels and normalized to obtain the final calibration image as shown in Fig. 3.

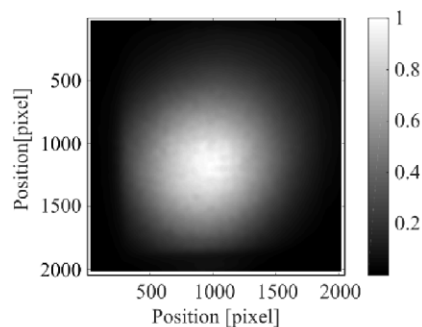


Fig. 3. Calibration image for the full field of view. Pixel size, 65 nm.

To demonstrate the patterned illumination technique, the standard GS algorithm with 20 iterations was used to calculate 40 phase masks of a rectangular ROI with the size of 529×492 pixels at the center of the field of view. A mirror sample with nanoholes was used to measure the geometry and the homogeneity of the illumination pattern in the focal plane. By using a LED transmission light source, the position of the mirror was adjusted until the resolution-limited spots of the nanoholes were in the focus. The 488 nm laser was then used to illuminate the sample with the desired pattern. Figure 4(a) shows low speckle noise after averaging 40 images. The intensity profile along the vertical direction of the desired pattern exhibits a pronounced non-uniform profile, as shown in Fig. 4(c) indicated in blue. The same desired pattern was defined to show the improvement of the homogeneous illumination based on the modified GS algorithm (in red). The resulting image is shown in Fig. 4(b).

It can be noted that the region outside of the ROI shows an intensity of less than 5%, because of the limitation of the Gerchberg-Saxton algorithm. The phase retrieval process is fast in the first few iterations, but computing an error-free illumination pattern requires much more iterations due to the slow convergence process [19]. Twenty iterations of the standard or of the modified GS algorithm were chosen to be the optimal number of iterations to achieve a well-defined illumination distribution. The resulting patterned illumination shows a good agreement with the desired pattern as shown in Figs. 4(a) and 4(b).

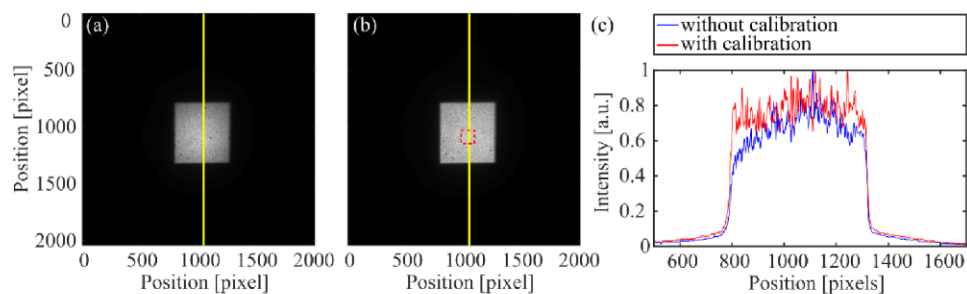


Fig. 4. The averaged intensity of 40 images calculated (a) by the standard GS algorithm and (b) by the modified GS algorithm. The region for the evaluation of the speckle contrast is indicated by the red dashed rectangle. (c) The intensity profiles along the yellow lines are indicated in (a) and (b). Pixel size, 65 nm.

To evaluate the speckles of the resulting image in combination with the modified GS algorithm, the speckle contrast (SC) was used and is defined as [16]:

$$SC = \sigma_s / \langle I \rangle,$$

where σ_s , is the standard deviation of the intensity in the region of the desired pattern, $\langle I \rangle$ is the mean intensity in the same region. We evaluated the speckle contrast in the region of interest indicated as a red dashed rectangle in the desired illumination pattern as shown in Fig. 4(b) by applying 1, 5, 10, 20, 30 and 40 phase masks on the SLM. Our experimental results showed a significant reduction of speckles by displaying multiple phase masks using the time averaging method as shown in Fig. 5. The SC was reduced from 47.59% when only one phase mask was applied to the SLM to 8.09% when 40 images were averaged. Using the time-averaging method, a lower SC can be achieved by displaying a larger number of phase patterns. The SC can be reduced to 3% when 1000 phase masks are displayed on the SLM during image acquisition [16]. Because the SC difference between displaying 30 and 40 phase masks on the SLM is about 1%, 30 phase masks were used in the following experiments to reduce computational time and it was still sufficient for the measurements.

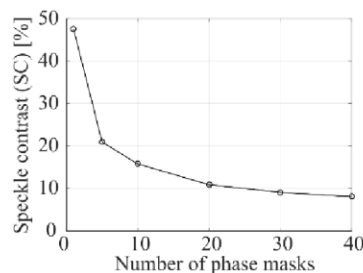


Fig. 5. Experimental results of speckle reduction by the time-averaging method.

To evaluate the influence of Gaussian and flat-top illumination on a biological sample, HeLa cell nuclei were stained with the nucleic acid dye SytoxOrange (Thermo Fisher). The samples were embedded in Dulbecco's Phosphate Buffered Saline (DPBS, Sigma Aldrich) while imaging. A nucleus was chosen and placed in the center of the field of view and excited by the 561 nm laser. The laser was set to low output power to prevent photobleaching, and a band-pass filter ET600/50 (Chroma Technology) was chosen to separate the fluorescence emission of SytoxOrange from the laser beam. Figure 6(a) shows the image of the nucleus under Gaussian illumination. The fluorescent intensity in the center of the nucleus is higher than at the edge. In contrast to the same nucleus illuminated by a flat-top irradiance distribution shown in Fig. 6(b), the image showed much weaker intensity dependence between the center

and the edge of the nucleus. In each image, the mean value of the background was subtracted as a set-off. Two normalized intensity profiles along two perpendicular axes are shown in Fig. 6(c). The intensity profiles indicate an underestimation of fluorescence signals in the nuclear structure when the nucleus was illuminated by a Gaussian beam. The quantitative evaluation of the intensity differences by using two illumination methods for the same nucleus revealed up to 26% and 25% intensity differences along the long axis and the short axis, respectively. Therefore, it may be essential to illuminate the sample with flat-top illumination in order to ensure a correct intensity-based quantitative evaluation of nuclear structures.

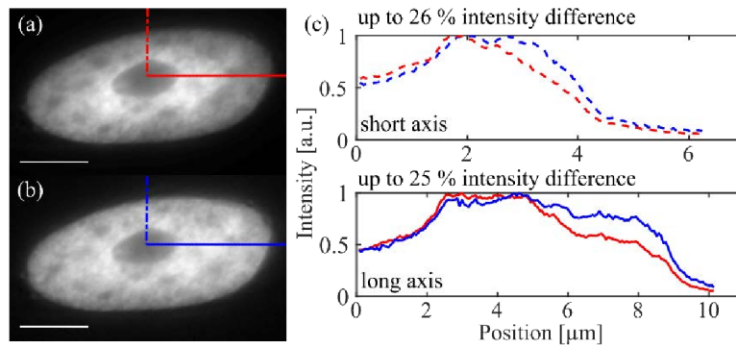


Fig. 6. Imaging of a HeLa cell nucleus by (a) Gaussian illumination and (b) flat-top illumination. (c) The normalized intensity profiles through the cell nucleus in two perpendicular directions (red: Gaussian illumination profiles, blue: flat-top illumination profiles). Scale bar, 5 μm .

The intensity transition is shown between the inside and the outside of the desired illumination region. One half of a nucleus was covered by a ROI indicated by a green rectangle in Figs. 7(a) and 7(b). For a better comparison, the whole nucleus is shown in Fig. 7(a). The mean value of the background in each image was subtracted. Figure 7(c) compares the normalized intensity profiles indicated by a red and a blue line in Figs. 7(a) and 7(b), respectively. A smooth transition of the intensity profile outside of the ROI can be observed. This can be contributed to out-of-focus fluorescence of the cell nucleus due to its extended depth. Furthermore, the low illumination intensity background as discussed in the beginning of this section, leads to a slight additional excitation of fluorophores outside the ROI.

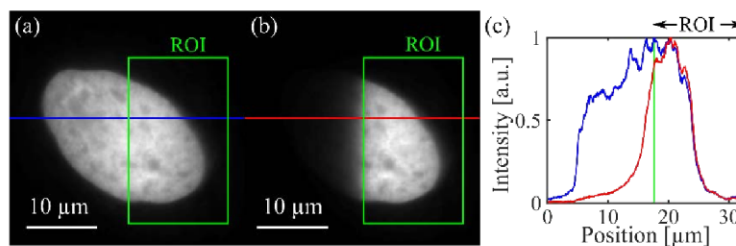


Fig. 7. HeLa cell nucleus images by illuminating (a) the whole cell nucleus and (b) the half of the nucleus. The illumination ROI is indicated by a green rectangle. (c) Normalized fluorescence intensity profiles through the center of the image of (a) and (b) indicated by a blue line (Fig. 7a) and a red line (Fig. 7b), respectively.

3.2 Super-resolution imaging by patterned illumination single molecule localization microscopy (piSMLM)

In the piSMLM setup, arbitrary patterns were generated with a phase-only SLM. In combination with the modified GS algorithm, light was efficiently redistributed. This leads to low power losses because the power was mostly independent of the size of the illumination pattern. The irradiance in the sample was simply increased by decreasing the size of the illumination pattern. This is very advantageous in SMLM applications using appropriate high

irradiance. In contrast, in the case of a DMD, which acts as an amplitude modulator, the transmitted power depends linearly on the size of the illumination area.

By illuminating the sample with a 561 nm laser, the measured dependency between total laser power in the sample and the size of the ROI was plotted as shown in Fig. 8. The results show that the laser power stays nearly constant for different ROI sizes. Irradiance between 1 and 5 kW/cm² could be sufficiently achieved for SMLM experiments at a laser output power of 200 mW. A slight decrease of the laser power in the sample can be seen when a larger ROI was defined. This may be due to a larger contribution of lower frequencies which were removed by the zeroth order blocker.

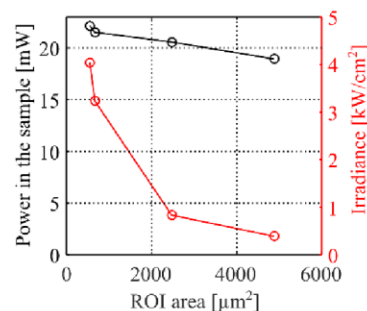


Fig. 8. Plot of laser power versus ROI area and the corresponding irradiance.

We demonstrated the patterned illumination technique for SMLM by imaging cell nuclei based on a recently described super-resolution microscopy method - fluctuation binding-activated localization microscopy (fBALM) [20]. HeLa cell nuclei were stained with DNA intercalator fluorophores - SytoxOrange (Thermo Fisher) and the samples were embedded in Dulbecco's Phosphate Buffered Saline (DPBS, Sigma Aldrich) for wide-field imaging. Two nuclei with elliptical shape were positioned in the center of the field of view and exposed to a low laser power with flat-top illumination to prevent photobleaching. The conventional wide-field image of the two nuclei is shown in Fig. 9(a).

For the fBALM experiment, the buffer was exchanged with the imaging buffer, enzymatic oxygen scavenging, to switch spatially DNA dye molecules between on and off states [20]. The nucleus on the right side was selected to acquire a super-resolution image and the desired target intensity pattern was defined according to the shape of this nucleus. Thirty phase masks were calculated based on the modified GS algorithm. The selected nucleus was exposed to an estimated irradiance of about 1 kW/cm² and 20,000 frames were imaged by setting the exposure time to 50 ms. Switching all 30 phase patterns within 50 ms exposure is not possible with the SLM because of the limited frame rate of the device of 60 Hz. Instead, a speckle free reconstructed super-resolution image can be obtained in SMLM, when the 30 phase patterns are sequentially displayed at equal time duration during the whole image acquisition process. Therefore, the 30 calculated phase masks were sequentially displayed on the SLM switching to the next phase mask every 34 s during the image acquisition.

Each illumination pattern shows laser speckles, which leads to a variation of excitation irradiance in the ROI in every single frame. The number of emitted photons may differ resulting in diverse localization precisions, depending on the local illumination irradiance [5]. In case of Gaussian illumination, the localization precision is field-dependent. In contrast, piSMLM exhibits a stochastic distribution of the localization precision in the illuminated area without field dependency. By filtering out the localized molecules with low precision, artifacts in the reconstruction image can be minimized. The stack of images was processed in ThunderSTORM [21]; the reconstructed super-resolution image is shown in Fig. 9(b).

We compared the wide-field image of the two nuclei and the super-resolution image of the nucleus. Since the selected nucleus was under the laser exposure, more than one million blinking dye molecules bound to DNA were localized and the signals were accumulated to

complete a super-resolution image of the nuclear DNA distribution with an average localization precision of $14.2 \text{ nm} \pm 5.6 \text{ nm}$. Although the left nucleus was not included in the ROI, it was illuminated with a low irradiance as discussed in the section 3.1, sufficient enough to induce a few undesired blinking events due to spatially transient DNA binding mechanism of SytoxOrange based on fBALM [22]. Therefore, a few molecules on the periphery close to the ROI were detected. As shown in Fig. 9(c), the intensity profile of the conventional fluorescence image (Fig. 9(a)) shows relatively smooth SytoxOrange fluorescence transitions in the nucleus, whereas the super-resolution image based on the fBALM method (Fig. 9(b)) reveals high and sharp intensity transitions of the nuclear structure as shown in Fig. 9(d), as expected from the underlying nuclear nanostructure [20,22].

Imaging nuclear structures requires typically at least 20,000 frames to obtain enough DNA molecules for the reconstruction of a super-resolution nuclear image. The total acquisition time is about 1,000 s with a camera exposure time of 50 ms. Hence, it is sufficient to display the calculated 30 phase patterns on the SLM sequentially by switching phase patterns every several seconds. To achieve higher switching frame rates of milliseconds, the synchronization between the SLM and the computer hardware would be necessary. For instance, the speed of the graphics card, which transforms the digital information across the DVI interface to the SLM, the response time of the liquid crystals in the SLM and the implementation of a C++ interface may be optimized. By combining the above mentioned methods, the speed of the switching phase patterns can potentially improve to less than 1 millisecond [23].

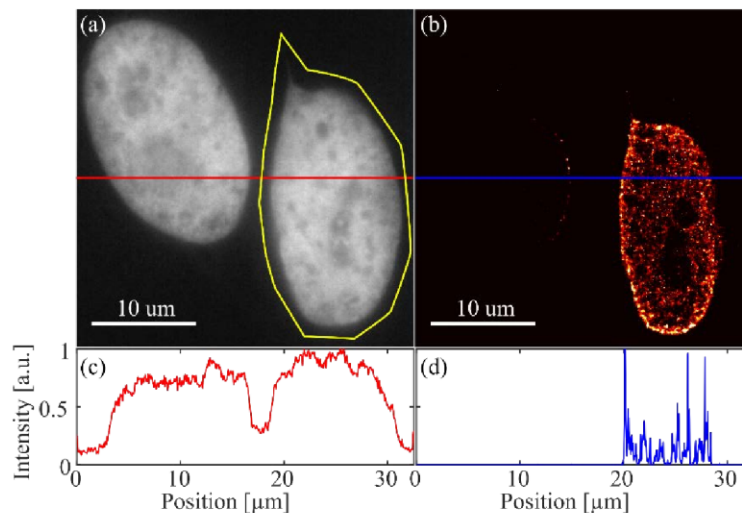


Fig. 9. HeLa cell nuclei images from piSLM: (a) Conventional wide-field image of two nuclei. The yellow contour line indicates the ROI for light exposure. (b) Super-resolution image of the selected nucleus (right). For a quantitative estimate, the normalized intensity profiles of the conventional wide-field image (c, red) and of the super-resolution fBALM image (d, blue) through the center of the field of view are shown.

3.3 Sample and switching buffer preparation

HeLa cells were cultured in a 25 ml culture flask filled with Dulbecco's Modified Eagle's Medium (DMEM, Thermo Fisher) supplemented with 10% fetal bovine serum (FBS, Thermo Fisher), 1% Penicillin Streptomycin (Pen Strep, Thermo Fisher) and 1% L-Glutamine (Thermo Fisher) in a cell culture incubator ($37 \text{ }^\circ\text{C}$, 5% CO_2). They were plated at low confluency on a 35 mm chamber (ibidi) and grown overnight. Cells were fixed with pre-warm ($37 \text{ }^\circ\text{C}$) 4% Formaldehyde (Sigma-Aldrich, 15 min) and washed three times with Dulbecco's Phosphate Buffered Saline (DPBS, Sigma-Aldrich). Afterwards, they were treated with 0.5% Triton X-100 in DPBS (10 min), washed three times with DPBS (5 min) and incubated at $37 \text{ }^\circ\text{C}$ with

1:1000 RNase A cocktail (Thermo Fisher) in DPBS overnight. Subsequently, cells were washed with DPBS and nuclei were stained with 0.05 μM SytoxOrange in DPBS (Thermo Fisher; 30 min).

A typical imaging buffer with an enzymatic oxygen scavenging system was prepared for fBALM. The buffer contains 10% glucose (Sigma-Aldrich), 5 mg/ml glucose oxidase from *Aspergillus niger* (Sigma-Aldrich), 500 $\mu\text{g/ml}$ catalase from bovine liver (Sigma-Aldrich) in DPBS.

4. Conclusion

We demonstrated patterned illumination single molecule localization microscopy (piSMLM) based on computer-generated holography. In contrast to the methods which the illumination is restricted in the field of view [7–10], piSMLM allows users to define arbitrarily shaped illumination regions at any desired position of interest. For example, defining the ROI covering a single cell nucleus allows concentrating all available laser light to the regions of interest instead of spreading it over the entire field of view. Therefore, higher excitation irradiance can be achieved in the ROIs and bleaching of surrounding areas can be avoided. By using the modified GS algorithm in combination with the time-averaging method, problems such as laser speckles and non-uniform illumination were eliminated simply by software implementations without additional optical components. The optical design by superimposing the phase of a Fresnel lens with the SLM phase patterned leads to an excellent separation of the desired patterned and the zeroth diffraction order to form a high contrast illumination area in the focal plane of the objective lens.

We demonstrated our method by imaging cell nuclei to compare flat-top illumination with commonly used Gaussian illumination. When illuminating by a Gaussian laser beam, apparently lower DNA densities on the periphery of the nucleus compared to the center of the nucleus were obtained. In contrast, when exciting with the flat-top illumination, no clear DNA density gradients could be observed. Therefore, it is advantageous to use flat-top illumination for an improved quantitative evaluation of intensity-based images. We demonstrated the potential of the patterned illumination technique with a flat-top irradiance distribution in combination with user-defined ROIs for SMLM. We can achieve high irradiance by defining smaller sizes of ROIs, because of the optical design of the piSMLM setup. As an example, a nucleus was arbitrarily selected and imaged with sufficient irradiance to acquire a super-resolution image with high localization precision.

The patterned illumination technique can be used for many types of microscopes, and it is not restricted to SMLM. For example, the generation of a square flat-top illumination can extend the field of view without edge artifacts for high-throughput microscopy. This microscopy method typically relies on tiling and stitching of multiple fields and the stitched images commonly show distinct dark borders, which degrade the image quality. The patterned illumination technique provides important tools to remove such an artifact without error-prone flat-field correction algorithm [24]. Other applications such as optogenetic applications or fluorescence recovery after photobleaching (FRAP) will also benefit from the freedom of defining single or multiple ROIs arbitrarily for light stimulation [25,26].

Funding

International PhD Programme on Gene Regulation, Epigenetics & Genome Stability, Mainz, Germany; TRR 166 Receptor Light, TP A04; the Leibniz science campus Infecto-Optics, project HotAim.

Acknowledgement

The authors thank Prof. Huang-Ming Chen and Prof. Cheng-Huan Chen (National Chiao Tung University, Taiwan) for discussions about the SLM device; the German Cancer Research

Center for providing the SLM device as a loan; and Dr. Xiaomin Liu, Dr. Márton Gelléri, Dr. Sandra Ritz, Dr. Mária Hanulová and David Ho for proof reading the manuscript.

References

1. K. Lidke, B. Rieger, T. Jovin, and R. Heintzmann, "Superresolution by localization of quantum dots using blinking statistics," *Opt. Express* **13**(18), 7052–7062 (2005).
2. E. Betzig, G. H. Patterson, R. Sougrat, O. W. Lindwasser, S. Olenych, J. S. Bonifacino, M. W. Davidson, J. Lippincott-Schwartz, and H. F. Hess, "Imaging intracellular fluorescent proteins at nanometer resolution," *Science* **313**(5793), 1642–1645 (2006).
3. M. J. Rust, M. Bates, and X. Zhuang, "Stochastic optical reconstruction microscopy (STORM) provides sub-diffraction-limit image resolution," *Nat. Methods* **3**(10), 793–795 (2006).
4. P. Lemmer, M. Gunkel, D. Baddeley, R. Kaufmann, A. Urich, Y. Weiland, J. Reymann, P. Müller, M. Hausmann, and C. Cremer, "SPDM: light microscopy with single-molecule resolution at the nanoscale," *Appl. Phys. B* **93**(1), 1–12 (2008).
5. R. E. Thompson, D. R. Larson, and W. W. Webb, "Precise nanometer localization analysis for individual fluorescent probes," *Biophys. J.* **82**(5), 2775–2783 (2002).
6. A. Burgert, S. Letschert, S. Doose, and M. Sauer, "Artifacts in single-molecule localization microscopy," *Histochem. Cell Biol.* **144**(2), 123–131 (2015).
7. K. M. Douglass, C. Sieben, A. Archetti, A. Lambert, and S. Manley, "Super-resolution imaging of multiple cells by optimised flat-field epi-illumination," *Nat. Photonics* **10**(11), 705–708 (2016).
8. J. Deschamps, A. Rowald, and J. Ries, "Efficient homogeneous illumination and optical sectioning for quantitative single-molecule localization microscopy," *Opt. Express* **24**(24), 28080–28090 (2016).
9. I. Khaw, B. Croop, J. Tang, A. Möhl, U. Fuchs, and K. Y. Han, "Flat-field illumination for quantitative fluorescence imaging," *Opt. Express* **26**(12), 15276–15288 (2018).
10. C. J. Rowlands, F. Ströhl, P. P. V. Ramirez, K. M. Scherer, and C. F. Kaminski, "Flat-field super-resolution localization microscopy with a low-cost refractive beam-shaping element," *Sci. Rep.* **8**(1), 5630 (2018).
11. R. W. Gerchberg and W. O. Saxton, "A practical algorithm for the determination of phase from image and diffraction plane pictures," *Optik (Stuttg.)* **35**(2), 237–246 (1972).
12. L. Valiya Peedikakkal, V. Steventon, A. Furley, and A. J. Cadby, "Development of targeted STORM for super resolution imaging of biological samples using digital micro-mirror device," *Opt. Commun.* **404**, 18–22 (2017).
13. V. Nikolenko, D. S. Peterka, R. Araya, A. Woodruff, and R. Yuste, "Spatial light modulator microscopy," *Cold Spring Harb. Protoc.* **2013**(12), 1132–1141 (2013).
14. Y. Takaki and M. Yokouchi, "Speckle-free and grayscale hologram reconstruction using time-multiplexing technique," *Opt. Express* **19**(8), 7567–7579 (2011).
15. W.-F. Hsu and C.-F. Yeh, "Speckle suppression in holographic projection displays using temporal integration of speckle images from diffractive optical elements," *Appl. Opt.* **50**(34), H50–H55 (2011).
16. J. W. Goodman, "Some fundamental properties of speckle," *J. Opt. Soc. Am.* **66**(11), 1145–1150 (1976).
17. A. Jesacher, S. Bernet, and M. Ritsch-Marte, "Broadband suppression of the zero diffraction order of an SLM using its extended phase modulation range," *Opt. Express* **22**(14), 17590–17599 (2014).
18. P. Pozzi, D. Gandolfi, M. Tognolina, G. Chirico, J. Mapelli, and E. D'Angelo, "High-throughput spatial light modulation two-photon microscopy for fast functional imaging," *Neurophotonics* **2**(1), 015005 (2015).
19. J. R. Fienup, "Phase retrieval algorithms: a comparison," *Appl. Opt.* **21**(15), 2758–2769 (1982).
20. A. Szczurek, L. Klewes, J. Xing, A. Gourram, U. Birk, H. Knecht, J. W. Dobrucki, S. Mai, and C. Cremer, "Imaging chromatin nanostructure with binding-activated localization microscopy based on DNA structure fluctuations," *Nucleic Acids Res.* **45**(8), e56 (2017).
21. M. Ovesný, P. Křížek, J. Borkovec, Z. Švindrych, and G. M. Hagen, "ThunderSTORM: a comprehensive ImageJ plug-in for PALM and STORM data analysis and super-resolution imaging," *Bioinformatics* **30**(16), 2389–2390 (2014).
22. A. Szczurek, U. Birk, H. Knecht, J. Dobrucki, S. Mai, and C. Cremer, "Super-resolution binding activated localization microscopy through reversible change of DNA conformation," *Nucleus* **9**(1), 182–189 (2018).
23. R. Förster, H.-W. Lu-Walther, A. Jost, M. Kielhorn, K. Wicker, and R. Heintzmann, "Simple structured illumination microscope setup with high acquisition speed by using a spatial light modulator," *Opt. Express* **22**(17), 20663–20677 (2014).
24. J. Chalfoun, M. Majurski, T. Blattner, K. Bhadriraju, W. Keyrouz, P. Bajcsy, and M. Brady, "MIST: Accurate and Scalable Microscopy Image Stitching Tool with Stage Modeling and Error Minimization," *Sci. Rep.* **7**(1), 4988 (2017).
25. L. Valon, A. Marín-Llauradó, T. Wyatt, G. Charras, and X. Trepat, "Optogenetic control of cellular forces and mechanotransduction," *Nat. Commun.* **8**, 14396 (2017).
26. C. Nakada, K. Ritchie, Y. Oba, M. Nakamura, Y. Hotta, R. Iino, R. S. Kasai, K. Yamaguchi, T. Fujiwara, and A. Kusumi, "Accumulation of anchored proteins forms membrane diffusion barriers during neuronal polarization," *Nat. Cell Biol.* **5**(7), 626–632 (2003).

Publication 3

[SC3] Nanographenes: ultrastable, switchable, and bright probes for super-resolution microscopy

Xiaomin Liu[†], Shih-Ya Chen[†], Qiang Chen, Xuelin Yao, Márton Gelléri, Sandra Ritz, Sachin Kumar, Christoph Cremer, Katharina Landfester, Klaus Müllen, Sapun Parekh, Akimitsu Narita, and Mischa Bonn

[†] Authors contribute this work equally

Angew. Chem. Int. Ed., 59(1), 496 – 502 (2020)

<https://doi.org/10.1002/anie.201909220>

Author	Shih-Ya Chen [†]
Conceptual research design	
Plan of research activities	x
Data collection	x
Data analyses and interpretation	x
Manuscript writing	x
Suggested publication equivalence value (Shared first authorship)	1.0

This paper is published by Wiley-VCH Verlag GmbH & Co. KGaA. under the terms of the Creative Commons [Attribution 4.0 License](#). No reprinted permission is required.

Super-Resolution Imaging

International Edition: DOI: 10.1002/anie.201909220
German Edition: DOI: 10.1002/ange.201909220

Nanographenes: Ultrastable, Switchable, and Bright Probes for Super-Resolution Microscopy

Xiaomin Liu^{+,*}, Shih-Ya Chen⁺, Qiang Chen, Xuelin Yao, Márton Gelléri, Sandra Ritz, Sachin Kumar, Christoph Cremer, Katharina Landfester, Klaus Müllen, Sapun H. Parekh, Akimitsu Narita, and Mischa Bonn^{*}

Abstract: Super-resolution fluorescence microscopy has enabled important breakthroughs in biology and materials science. Implementations such as single-molecule localization microscopy (SMLM) and minimal emission fluxes (MIN-FLUX) microscopy in the localization mode exploit fluorophores that blink, i.e., switch on and off, stochastically. Here, we introduce nanographenes, namely large polycyclic aromatic hydrocarbons that can also be regarded as atomically precise graphene quantum dots, as a new class of fluorophores for super-resolution fluorescence microscopy. Nanographenes exhibit outstanding photophysical properties: intrinsic blinking even in air, excellent fluorescence recovery, and stability over several months. As a proof of concept for super-resolution applications, we use nanographenes in SMLM to generate 3D super-resolution images of silica nanocracks. Our findings open the door for the widespread application of nanographenes in super-resolution fluorescence microscopy.

Introduction

Super-resolution fluorescence microscopy has enabled visualizing structures with a resolution substantially better than that prescribed by the physics of diffraction-limited conventional microscopy.^[1,2] Several important approaches to super-resolution fluorescence microscopy rely on fluorophores switching between bright, emissive (on) and dark

(off) states stochastically when they are continuously excited by light. This phenomenon underlies single-molecule localization microscopy (SMLM), for example, stochastic optical reconstruction microscopy (STORM),^[3] photoactivated localization microscopy (PALM),^[4] and minimal emission fluxes (MINFLUX) microscopy in the localization mode.^[5] Presently, four classes of photoswitchable fluorophores are used in such applications: small-molecule organic dyes,^[6,7] photoactivatable/switchable fluorescent proteins,^[8,9] inorganic quantum dots (QDs),^[10–12] and carbon dots (CDs).^[13–16] Each class of fluorophores has its strengths and weaknesses from either a photophysical or application perspective.^[17] Briefly, organic dyes, such as Alexa 647, the gold standard in SMLM, are small molecules with excellent blinking properties like high photon numbers and low on-off duty cycles. However, their photophysical properties are strongly environmentally (buffer) dependent, restricting their use for super-resolution imaging to specific environments, and the imaging buffer typically has a limited chemical reaction lifetime (less than several hours) after preparation. Photoactivatable/switchable fluorescent proteins have exquisite target molecule specificity but have the issue of low photon numbers resulting in a lower localization precision compared to organic dyes.^[18] QDs are very photostable and bright, but their large size (≈ 10 nm) and high on-off duty cycle^[10] limit their function as reliable minimally invasive probes. Also, the toxicity of QDs contain-

[*] Dr. X. Liu^{+,*}, Q. Chen, X. Yao, Dr. S. Kumar, Prof. Dr. K. Landfester, Prof. Dr. K. Müllen, Prof. Dr. S. H. Parekh, Prof. Dr. A. Narita, Prof. Dr. M. Bonn
Max Planck Institute for Polymer Research
Ackermannweg 10, 55128 Mainz (Germany)
E-mail: liuxiaomin@mpip-mainz.mpg.de
b Bonn@mpip-mainz.mpg.de
S. Chen^{+,*}, Dr. M. Gelléri, Dr. S. Ritz, Prof. Dr. C. Cremer
Institute of Molecular Biology gGmbH (IMB)
Mainz (Germany)
Prof. Dr. C. Cremer
Department of Physics, University of Mainz (JGU)
Mainz (Germany)
and
Institute for Pharmacy and Molecular Biotechnology (IPMB)
and Kirchhoff Institute for Physics (KIP)
University of Heidelberg
Heidelberg (Germany)
Prof. Dr. K. Müllen
Institute of Physical Chemistry
Johannes Gutenberg-University Mainz
Mainz (Germany)

Dr. S. Kumar, Prof. Dr. S. H. Parekh
Department of Biomedical Engineering
University of Texas at Austin
Austin, TX (USA)
Prof. Dr. A. Narita
Organic and Carbon Nanomaterials Unit
Okinawa Institute of Science and Technology Graduate University
Okinawa (Japan)

[†] These authors contributed equally to this work.

[††] co-first authors

Supporting information and the ORCID identification number for one of the authors of this article can be found under:
<https://doi.org/10.1002/anie.201909220>

© 2019 The Authors. Published by Wiley-VCH Verlag GmbH & Co. KGaA. This is an open access article under the terms of the Creative Commons Attribution Non-Commercial License, which permits use, distribution and reproduction in any medium, provided the original work is properly cited, and is not used for commercial purposes.

ing heavy metal atoms may restrict their applicability in biomedicine.^[19] CDs have environment-independent blinking properties and are smaller than QDs; however, the undefined/mixed chemical structures not only induce broader fluorescence absorption and emission spectra but also make target-specific binding difficult.

Graphene quantum dots (GQDs) are nanoscale graphene fragments with well-defined, quantized energy levels and have recently been proposed as an environmentally friendly alternative to CDs and QDs.^[20] GQDs are, in principle, superior for microscopy imaging due to their small size (typically < 10 nm) and low toxicity. The synthetic approaches to GQDs can be classified in general as top-down or bottom-up approaches. The top-down synthesis method uses physical or chemical techniques to “cleave” graphene^[20] or other carbon allotropes such as C₆₀ fullerene^[21] and double-walled carbon nanotubes.^[22] Such methods produce GQDs varying in size and chemical structure, similar to CDs, which results in heterogeneous CD-like photophysical properties. The nanographenes employed in this work are molecularly defined GQDs with a monodisperse character, that is, a precise chemical structure and elemental composition, which are more specifically called (nano)graphene molecules.^[23,24] They are obtained by a bottom-up synthesis method which is stepwise derivatization from small organic molecules as starting materials. This method, based on synthetic organic chemistry, not only permits creating nanographenes with well-defined absorption and emission spectra defined by their precise chemical structures, but also enables the introduction of various functional groups^[20,25] similarly to organic dyes, e.g., for binding to specific ligands or reactions with specific target molecules. The spectral (absorption and emission) properties of nanographenes can be tailored by engineering the shapes and edge structures with the extension of carbons.^[26] These advantages pave the way to develop nanographenes as a new series of fluorophores for optical imaging. While stable fluorescence, i.e., nonblinking emission from nanographenes has been demonstrated,^[27–30] this stable, nonblinking, fluorescence has precluded the application of nanographenes from SMLM applications.

Results and Discussion

Here, we demonstrate that, in contrast to previous reports,^[27–30] nanographenes show outstanding blinking behavior, combining many of the superior photophysical properties of existing chromophores; they are very small and display blinking independent of the (buffer or air) environment, making them ideal candidates for SMLM. This discovery can be traced to improved nanographene synthesis and better control over the nanographene aggregation behavior. We show that a broad portfolio of nanographenes, for which the chemical structures, and hence absorption and emission spectra, can be precisely tuned, exhibit near-ideal properties as a new class of probes for super-resolution microscopy allowing multiplexing and 3D SMLM.

In this work, we characterize the properties of four types of graphene molecules (**GM**): **DBOV-Mes**, **GM-C60**, **GM-**

C78, and **GM-C96** as blinking probes, benchmarked against Alexa 647, a widely used organic fluorophore in SMLM. These properties include 1) size, 2) absorption and emission spectra, 3) duty cycle (fraction of time a molecule resides in its fluorescent state), and 4) photon number (detected photons per switching event). Figure 1a,b shows the chemical structures and spectra of **DBOV-Mes**, dibenzo[*hi,sr*]ovalene (**DBOV**) with two mesityl (**Mes**) groups,^[31,32] and **GM-C60**^[33] with alkyl side chains. **DBOV-Mes (GM-C38)** and **GM-C60** consist of 38 and 60 sp²-hybridized carbons in their aromatic cores, both with an approximate size of 1 to 2 nm. The chemical structures and spectra of **GM-C78**, **GM-C96**, and Alexa 647 are shown in the Supporting Information, Figures S1 and S2. Table 1 shows general fluorescent characterizations of nanographenes in an organic solvent and Alexa 647 in an aqueous solvent. All of the measured nanographenes exhibit well-defined absorption and emission spectra with different emission wavelengths. In particular, **DBOV-Mes** has very narrow absorption and emission spectra comparable to those of commonly used organic dyes, e.g., Alexa 647, making this nanographene ideal for multicolor imaging.

As mentioned above, Alexa 647 and other organic dyes maintain proper blinking properties in a special blinking buffer. Here we used a standard buffer containing an enzymatic oxygen scavenger system with glucose oxidase and a primary thiol (cysteamine, MEA).^[6] Most often due to oxidation reactions or side reactions, these imaging buffers degrade over time, and blinking conditions are maintained only for a few hours.^[18] We measured the blinking properties of nanographenes in different environments (i.e., without any blinking buffer) and compared it to Alexa 647 under the optimized conditions (Table 2 and Figures S3–10). As a straightforward measurement to demonstrate the blinking performance of nanographenes in different environments, based on the observation of blinking events, we quantified the duty cycles and the average photon numbers per blinking event for nanographenes in air, in Dulbecco's phosphate-buffered saline (DPBS) buffer, or embedded in a polystyrene (PS) film. As shown by the representative dataset shown in Figure 1c, nanographene **GM-C60** exhibits intrinsic blinking when exposed to air. Figure 1d,e shows the duty cycle and the mean photon number per switching event of **GM-C60** as compared to the properties of Alexa 647. Figure 1f and Table 2 show that **DBOV-Mes** and **GM-C60** in each environment have average photon numbers per blinking event about 1.3-fold higher than those of Alexa 647 in the optimized blinking buffer while maintaining comparable duty cycles and blinking times. This result demonstrates the versatility of nanographene fluorophores compared to small dye molecules; they retain the required properties for SMLM: good blinking in ambient conditions and no special buffer chemistry is needed. Regarding the blinking mechanism of nanographenes, their blinking behavior in different environments indicates a mechanism different from that of traditional organic dyes,^[34] semiconductor quantum dots,^[35,36] and carbon nanodots.^[16,37] Elucidating the blinking mechanism of nanographenes is the topic of ongoing research.

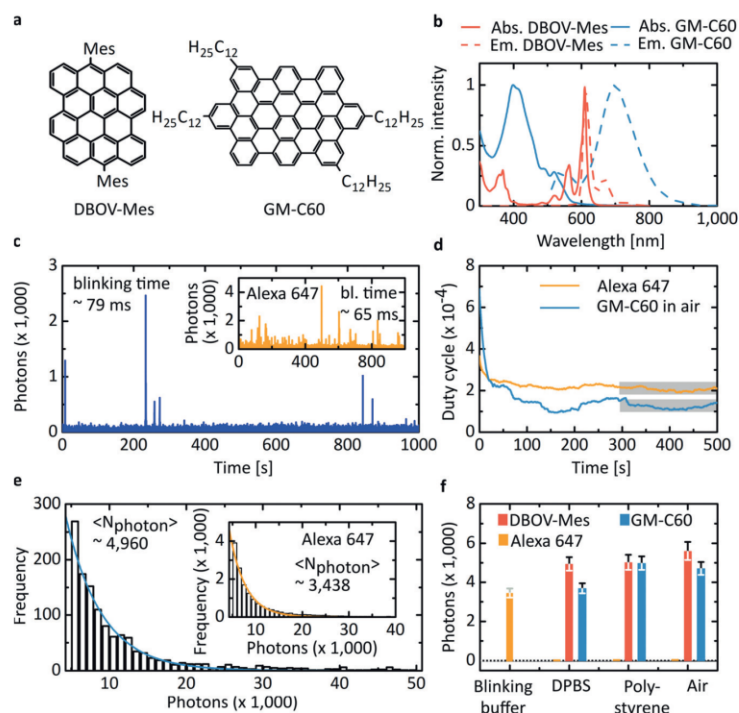


Figure 1. Fluorescence and blinking properties of nanographenes. a) Chemical structures of selected nanographenes, **DBOV-Mes** (**GM-C38**) and **GM-C60**. b) Absorption (solid lines) and emission spectra (dotted lines) of **DBOV-Mes** (red) and **GM-C60** (blue). c) Representative single-molecule fluorescence time trace of **GM-C60** measured in air and of Alexa 647 (inset) in a standard blinking buffer containing thiol (MEA, 10 mM) and an oxygen-scavenging system [(glucose oxidase with catalase (GLOX))]. d) On-off duty cycle (fraction of time a molecule resides in its fluorescent state) of **GM-C60** (blue) and Alexa 647 (orange), calculated from single-molecule fluorescence time traces. The equilibrium duty cycle was calculated within the time window 300–500 s (gray box). e) Histogram of detected photons per switching event and single-exponential fit of **GM-C60** and Alexa 647 (inset). Mean photon numbers were determined by the exponential fit. f) Mean photons detected per switching event for Alexa 647 (orange) in the blinking buffer, **DBOV-Mes** (red) and **GM-C60** (blue) in DPBS, embedded in PS film, and in air, respectively. For Alexa 647, no blinking events could be visualized without the blinking buffer. Error bars are the 95% confidence interval of the fit. Detailed quantitative analysis of Alexa 647 in the blinking buffer, **DBOV-Mes**, and **GM-C60** in different environments and other types of nanographenes embedded in PS film can be found in the Supporting Information, Section 1.

In addition to the excellent blinking properties, we further investigated the photo- and chemical stability of nanogra-

phenes **DBOV-Mes** and **GM-C60** by quantifying the photon number per switching event. Figure 2a,b shows the measured mean photons per blinking event of **DBOV-Mes** and **GM-C60** in air and in PS film for freshly prepared samples and samples stored over several months. The blinking properties of both **DBOV-Mes** and **GM-C60** were unchanged over several months. Also, the long-term stability of **DBOV-Mes** was assessed by measuring the absorption spectrum of **DBOV-Mes** dissolved in toluene over six months. We found no changes in the absorption spectrum of the **DOB**V-Mes solution, as shown in Figure S11, indicating low aggregation tendency in organic solvents and high stability of **DBOV-Mes**.

As shown previously,^[6,18] the fluorescence emission from some organic dyes, including Alexa 647, can be recovered from a dark (off) state back to the on state with a pulse of ultraviolet or blue light. We performed a similar recovery experiment on nanographenes by first using continuous excitation (532 nm) radiation to send most of the nanographenes to a dark state and then measuring the fraction of molecules that recovered following low irradiance of illumination from a 405 nm laser. Figure 2c shows three raw images from left to right acquired at the beginning of the measurement, after 16 min of continuous illumination with a 532 nm laser, and after a short pulse (≈ 1.5 s) of 405 nm illumination, respectively. To quantify the fluorescence recovery by 405 nm laser, the number of detected blinking events was analyzed in a time trace of more than 30 min. As shown in Figure 2d, the number of detected blinking events from nanographenes decreased with time over 16 min (20000 frames) from the beginning of the experiment. In the following 15 min, an

Table 1: Fluorescence properties of different nanographenes and Alexa 647 in solution.

Dye	Excitation max. [nm]	Emission max. [nm]	FWHM of excitation spectrum [nm]	FWHM of emission spectrum [nm]	Extinction [$M^{-1} cm^{-1}$]	Quantum yield	Brightness [$M^{-1} cm^{-1}$]
Alexa 647	650 ^[a]	665 ^[a]	38 ^[b]	35 ^[b]	239 000 ^[a]	0.33 ^[a]	78 870
DBOV-Mes (GM-C38)	610	614	15	22	70 000	0.79	55 300
GM-C60	412	701	84	220	22 000	0.1	2200
GM-C78	— ^[c]	513	— ^[c]	80	54 000	0.02	1080
GM-C96	491	650	83	141	61 000	0.01	610

[a] Spectral maxima, extinction coefficient, and quantum yield of Alexa 647 from Ref. [9]. [b] Full width at half maximum (FWHM) of the excitation and emission spectra of Alexa 647 from the dye manufacturer. [c] Peak wavelength and FWHM of **GM-C78** excitation spectrum not available due to the wavelength limitation of the spectrometer. The fluorescence properties of nanographenes were measured in toluene solution.

Table 2: Summary of blinking properties of different nanographenes and Alexa 647.

Dye	Alexa 647	DBOV-Mes (GM-C38)			GM-C60		GM-C78	GM-C96
Environment	blinking buffer ^[a]	DPBS buffer	air	poly-styrene	DPBS buffer	air	poly-styrene	poly-styrene
Detected photons per switching event	3438	4918	5570	4902	3673	4960	4690	5740
Duty cycle [$\times 10^{-4}$]	2.1	1.3	4.7	8	5.3	1.2	3.2	2.7
Blinking time [ms]	65	87	108	54	75	79	96	83

[a] Blinking properties of Alexa 647 measured in the presence of an enzymatic oxygen-scavenging system [glucose oxidase with catalase (GLOX)] and a primary thiol (MEA, 10 mM). Two representatives of nanographenes, **DBOV-Mes** and **GM-C60**, were measured in three different environments: air, DPBS, and embedded in PS, while the other two nanographenes, **GM-C78** and **GM-C96**, were measured only in a PS film.

additional recovery irradiation (405 nm laser) was administered for 1–2 seconds and was applied on every ≈ 1000 frames. The number of blinking events clearly shows that a substantial number of nanographenes were switched back

into the on state following each 405 nm irradiation. Although both Alexa 647 and **DBOV-Mes** can be transferred into a reversible off state and stochastically activated, the reversible nature of Alexa 647 remains only when it is freshly prepared blinking buffer. On the contrary, the **DBOV-Mes** sample, in air, maintains its blinking behavior even 125 days after preparation, as demonstrated in Figure 2d. From a practical point of view, such reversible activation of the photorecovery property of **DBOV-Mes**, even in air, strongly broadens the potential applications of nanographenes in super-resolution microscopy.

As a proof-of-concept for super-resolution microscopy using nanographenes, we prepared nanoscale crevices in glass and imaged them with 3D-SMLM. Afterward, the resulting 3D SMLM image was compared with atomic force microscopy (AFM). Figure 3a shows a schematic of the procedure of depositing nanographenes onto the surface of coverslips and into crevices used for 3D SMLM and AFM imaging. The coverslip was initially examined by conventional brightfield microscopy (Figure S12a) and fluorescence microscopy (Figure S12b). For SMLM, a 2D time series stack of images was acquired, and the raw images were processed to localize nanographenes in 3D within the sample. For 3D localization we first calibrated the microscopy system (Figures S13 and S14), and the **DBOV-Mes** molecules were localized over an axial (z) interval of ± 300 nm with an average localization precision of 17.2 nm. A detailed description of the 3D localization and a direct image comparison between conventional microscopy and the 3D SMLM method can be found in the Supporting Information, Section 2. The molecular localizations were sub-

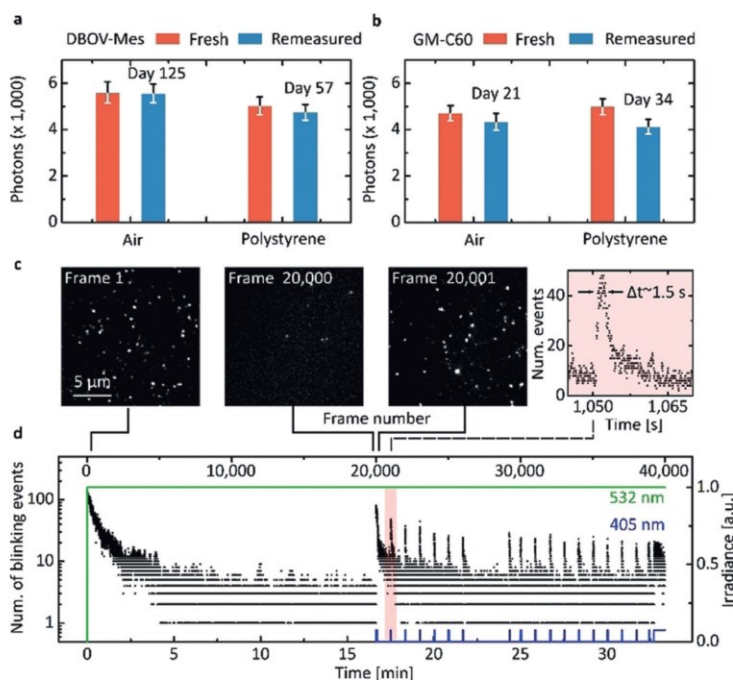


Figure 2. Environmental stability and photorecovery of the nanographenes **DBOV-Mes** and **GM-C60**. a, b) Comparison of the mean number of photons detected per switching event for **DBOV-Mes** and **GM-C60** in air and PS film directly after sample preparation and then remeasured after the waiting time indicated in the legend. Note: The sample of **GM-C60** in air was kept under ambient conditions and not shielded from light before remeasurement. All other samples were stored in a dark environment at room temperature. c) Representative fluorescence images at three selected frames: 1, 20000, and 20001. d) Number of detected blinking events per image frame versus the frame number (time). The first and second images in (c) were acquired more than 16 minutes (20000 frames) apart under continuous 4 kWcm^{-2} excitation with 532 nm (green line). Starting from frame 20001, an additional 405 nm excitation (blue line) with 0.30 kWcm^{-2} was administered for 1–1.65 seconds and this was repeated around every 1000 frames. The number of nanographenes residing in the on state could be repetitively increased by the sample regeneration using the 405 nm excitation. Inset (in pink): an example of fluorescence recovery after exposure to 405 nm laser for around 1.5 seconds. The measured nanographene sample of **DBOV-Mes** in air shown in Figure 2c,d was recorded 125 days after preparation.

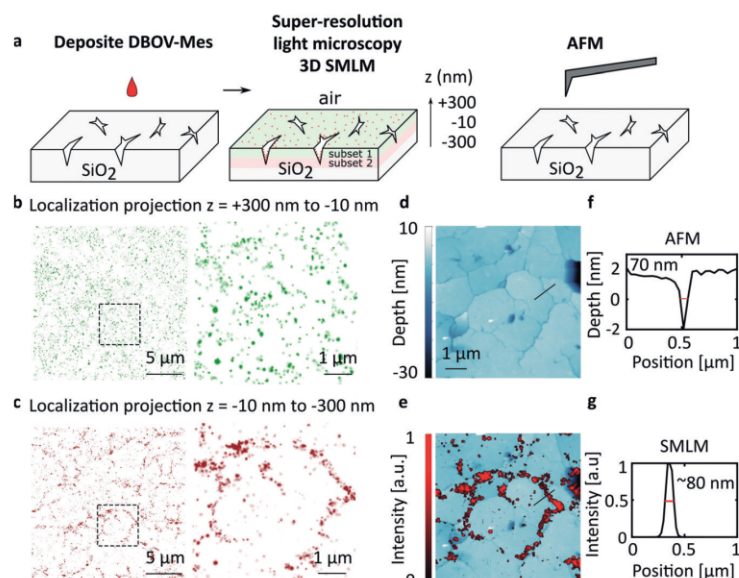


Figure 3. 3D super-resolution microscopy images of nanometer-sized crevices in a glass substrate. a) Imaging procedure for the “etched” coverslips showing crevice features and subsets of molecules localized on (shaded green) or right below (shaded red) the macroscopic (planar) glass surface. After deposition of nanographenes (DBOV-Mes) on the coverslips (left), the structure was imaged using 3D SMLM (middle) and AFM (right). The resulting blinking localization of 3D SMLM was classified into two subsets, which indicate the distribution of nanographenes close to (green) and right below (red) the glass–air interface in the cracks. b) For the intensity projection along the z -axis between 300 and -10 nm (subset 1) above the “etched” structure, a relatively random spatial distribution of nanographenes was observed. c) For the region between -10 and -300 nm (subset 2), the spatial structure of crevices is apparent. d) AFM reveals the surface structure in the region of interest in (b) and (c). e) Overlay of the SMLM image in (c) and AFM image in (d) shows strong overlapping features after image registration. f, g) Line profiles from AFM (d) and SMLM (c) images show an FWHM about ≈ 70 nm and ≈ 80 nm, respectively.

divided into two categories based on the bimodal distribution of localization numbers as a function of axial distance (Figure S14). An intensity projection of the first subset for the z positions from $+300$ to -10 nm (Figure 3b) shows a relatively homogeneous distribution of nanographenes on the glass surface (not deep into the crevices), as expected. In contrast, the intensity projection from the second subset from $z = -10$ nm to -300 nm (Figure 3c) shows a pattern of nanographenes that is considerably more heterogeneous, as though they are located within the etched, subsurface crevices of the cracks.

As a comparison, AFM was used to scan the substructure of the cracks in the same regions shown in Figure 3b,c. The AFM image reveals a flat surface with numerous cracks (Figure 3d). A larger field of view using the topological scan of AFM in the same region can be found in the Supporting Information, Section 3, Figure S15. After image registration (Figure 3e) of the AFM image and the SMLM image from $z = -10$ nm to -300 nm, the two high-resolution images show highly correlated features at crack locations (Figure 3e), demonstrating that the nanographene localizations in the second subset indeed reveal the substructure of crevices. As

shown in the indicated line profiles in Figure 3d,e, the surface profile of the AFM image (Figure 3f) and the intensity profile based on SMLM (Figure 3g) have a similar full width at half maximum (FWHM) of the “crack” of 70 nm and 80 nm, respectively.

Although various techniques have been developed to resolve nanostructures, e.g., X-ray microscopy,^[38] AFM,^[39] and electron microscopy (EM),^[40] these approaches have limitations regarding their applicability. The combination using exceptionally stable and intrinsically blinking nanographenes in 3D SMLM allows visualizing nanostructures in greater depth compared to AFM, where the geometrical restriction of the tip can cause problems, or methods like EM tomography, which requires complete sample destruction.

Conclusion

In summary, nanographenes with atomically defined chemical structures exhibit ideal properties for various super-resolution microscopy methods due to their environmentally independent blinking behavior, large photon numbers, good stability, and well-defined excitation and emission spectra. In our case, the highly pure synthetic production and sample preparation allowed us to discover these properties, which stand in contrast to the general knowledge

that nanographenes are constant fluorescent emitters. Atomically precise nanographenes blink in various environments and have high photon numbers per blinking event and low duty cycles in comparison to Alexa 647, the current gold standard small-molecule dye. Moreover, the nanographene dyes exhibit extremely high sample stability of more than 1000-fold longer than Alexa 647. The nanoscale structural imaging of etched cracks in glass demonstrates the potential of nanographenes in super-resolution fluorescence microscopy for applications in materials science. Also, the exquisite chemical control and blinking environment-independent properties of nanographenes offer a great opportunity to investigate blinking mechanisms, which is challenging for organic dyes due to complex buffer dependence and the relatively minimal shelf-life of buffer solutions.^[6] Moreover, specific functional side groups can be incorporated at peripheral positions of the nanographenes, for example, hydrophilic groups to enhance the water solubility and binding functionality for protein targeting making nanographenes very promising dyes for bioimaging applications.

Experimental Section

Microscopy

3D SMLM was performed with a SR GSD 3D (Leica) equipped with four lasers: 488 nm (300 mW), 532 nm (500 mW), and 642 nm (500 mW) for excitation, and 405 nm (30 mW) for fluorescence reactivation. An HCX PL APO 160 × 1.43 NA Oil CORR-TIRF (Leica) objective and the total internal reflection (TIRF) mode were used for single-molecule blinking measurements and for super-resolution imaging. For all measurements of nanographenes, the 532 nm laser and the emission bandpass filter (550–650 nm/449–451 nm) were used. For the measurements using Alexa 647, the 642 nm laser and the emission bandpass filter (660–760 nm) was used. The microscope was equipped with a back-illuminated EMCCD camera (iXonDU-897, Andor). The resulting images have a pixel size of 100 nm. The detailed description of the setup can be found in the Supporting Information, Section 4.1.

Atomic force microscopy (AFM, Dimension FastScan, Bruker) was done in the tapping mode in air. A standard V-shaped silicon nitride cantilever which has a spring constant of 26 N m^{-1} with a pyramidal tip from Bruker AFM probes (OTESPA-R3) was mounted. The tip has on average a height of $15 \mu\text{m}$ and a radius of curvature of around 10 nm with a vertex angle of 35° and 18° . Further information about the AFM can be found in the Supporting Information, Section 4.2. AFM images were acquired with a 0.5 Hz line rate, and images with $512 \text{ pixels} \times 512 \text{ pixels}$ were acquired.

Experiments for Blinking Properties of Single Nanographenes and Alexa 647

For evaluation of the blinking properties including photon per switching event and on-off duty cycle, nanographene samples were prepared in different embedding media including air, DPBS, and polystyrene. For comparison, additional samples with Alexa 647 were prepared in an oxygen-scavenging system. Detailed information can be found in the Supporting Information, Section 5.

Multiple series of 20000 frames were recorded for every nanographene variant. Nanographenes were excited continuously during imaging with the appropriate wavelength. Images were acquired at an exposure time of 50 ms and an EM gain of 100.

To extract single-molecule time traces, first a maximum intensity projection of the recorded time series was generated. Molecules then were localized in the maximum-intensity projection image, returning the positions of all molecules visible throughout the recorded time series. Single-molecule time traces were then extracted as background-corrected intensities at these positions over all recorded frames. Photon counts and blinking times were determined by localization of single-molecule positions in all frames and merging into blinking events. Resulting histograms of photons per blinking event and blinking duration were fit with a single-exponential function. The reported mean values and errors were extracted from the respective fits. For the detailed description, see the Supporting Information, Section 6.

To investigate the photorecovery characteristics of nanographenes, 40000 frames were acquired with an exposure time of 50 ms and an EM gain of 100. At the first 20000 frames, images were acquired by continuous laser irradiation at 532 nm with an irradiance of 4 kW cm^{-2} . While acquiring images from frame 20000 to frame 40000, additionally the 405 nm laser with an intensity of 0.30 kW cm^{-2} was administered for 1–1.65 seconds and this was repeated around every 1000 frames. The images were processed and localizations were determined for analysis.

Experiments for Imaging 3D Crevice Structures

A mild chemical treatment was used to etch nanoscale “cracks” on the surface of a borosilicate coverslip (ibidi, Gridded glass coverslips Grid-50). For fluorescence imaging, $5 \mu\text{L}$ (1 nm) nanographene in toluene was applied on the coverslip. The detailed sample preparation is described in the Supporting Information, Section 7. For super-resolution imaging of the 3D crevices on the coverslips, the

TIRF mode was used to excite the samples with an intensity of 10 kW cm^{-2} at a laser wavelength of 532 nm. 40000 frames with an exposure time of 50 ms and an EM gain of 100 were acquired and processed to determine the 3D localization. AFM images of the same region were acquired, and the resulting image is shown in Figure S15a. The complete overlay image of AFM and SMLM after image registration is shown in Figure S15b for comparison.

Acknowledgements

We acknowledge Max Planck Society and the Human Frontiers in Science Program (RGP0045/2018) for financial support, and the Microscopy Core Facility at IMB for use of the Leica GSD super-resolution microscope. S.-Y.C. acknowledges the international PhD programme on Gene Regulation, Epigenetics & Genome Stability (Mainz, Germany). X.Y. is grateful for the scholarship from China Council Scholarship (CSC). We thank M. Müller and M. Kappl for nanostructure fabrication; L. Driessen for gold film coating on glass; G. Hermann for gold etching; X. Ling for glass cleaning. We thank P. Han, F. Geyer, Y. Yao, and R. Berger for insightful discussions.

Conflict of interest

X. Liu, A. Narita, S. Parekh, Q. Chen, C. Cremer, K. Landfester, K. Müllen, and M. Bonn are listed as inventors on a patent application (application no. 18199451.8 – EPO) and A. Narita, Q. Chen, K. Müllen, X. Liu, S. Parekh, and M. Bonn are listed as inventors on a patent application (application no. 18199447.6 – EPO) related to the work presented in this manuscript. All other authors have nothing to disclose.

Keywords: blinking · chromophores · fluorescence · nanographenes · super-resolution imaging

How to cite: *Angew. Chem. Int. Ed.* **2020**, *59*, 496–502
Angew. Chem. **2020**, *132*, 504–510

- [1] L. Schermelleh, A. Ferrand, T. Huser, C. Eggeling, M. Sauer, O. Biehlmaier, G. P. C. Drummen, *Nat. Cell Biol.* **2019**, *21*, 72–84.
- [2] S. Pujals, N. Feiner-Gracia, P. Delcanale, I. Voets, L. Albertazzi, *Nat. Rev. Chem.* **2019**, *3*, 68–84.
- [3] M. J. Rust, M. Bates, X. Zhuang, *Nat. Methods* **2006**, *3*, 793–796.
- [4] E. Betzig, G. H. Patterson, R. Sougrat, O. W. Lindwasser, S. Olenych, J. S. Bonifacino, M. W. Davidson, J. Lippincott-Schwartz, H. F. Hess, *Science* **2006**, *313*, 1642–1645.
- [5] F. Balzarotti, Y. Eilers, K. C. Gwosch, A. H. Gynnä, V. Westphal, F. D. Stefani, J. Elf, S. W. Hell, *Science* **2017**, *355*, 606–612.
- [6] G. T. Dempsey, J. C. Vaughan, K. H. Chen, M. Bates, X. Zhuang, *Nat. Methods* **2011**, *8*, 1027–1036.
- [7] L. Nahidiazar, A. V. Agronskaia, J. Broertjes, B. van den Broek, K. Jalink, *PLoS One* **2016**, *11*, e0158884.
- [8] R. M. Dickson, A. B. Cubitt, R. Y. Tsien, W. E. Moerner, *Nature* **1997**, *388*, 355–358.
- [9] J. Lippincott-Schwartz, G. H. Patterson, *Trends Cell Biol.* **2009**, *19*, 555–565.
- [10] M. Kuno, D. P. Fromm, H. F. Hamann, A. Gallagher, D. J. Nesbitt, *J. Chem. Phys.* **2000**, *112*, 3117–3120.

- [11] K. A. Lidke, B. Rieger, T. M. Jovin, R. Heintzmann, *Opt. Express* **2005**, *13*, 7052.
- [12] P. Hoyer, T. Staudt, J. Engelhardt, S. W. Hell, *Nano Lett.* **2011**, *11*, 245–250.
- [13] N. C. Verma, S. Khan, C. K. Nandi, *Methods Appl. Fluoresc.* **2016**, *4*, 044006.
- [14] B. Zhi, Y. Cui, S. Wang, B. P. Frank, D. N. Williams, R. P. Brown, E. S. Melby, R. J. Hamers, Z. Rosenzweig, D. H. Fairbrother, et al., *ACS Nano* **2018**, *12*, 5741–5752.
- [15] H. He, X. Liu, S. Li, X. Wang, Q. Wang, J. Li, J. Wang, H. Ren, B. Ge, S. Wang, et al., *Anal. Chem.* **2017**, *89*, 11831–11838.
- [16] A. M. Chizhik, S. Stein, M. O. Dekaliuk, C. Battle, W. Li, A. Huss, M. Platen, I. A. T. Schaap, I. Gregor, A. P. Demchenko, et al., *Nano Lett.* **2016**, *16*, 237–242.
- [17] D. Jin, P. Xi, B. Wang, L. Zhang, J. Enderlein, A. M. van Oijen, *Nat. Methods* **2018**, *15*, 415–423.
- [18] S. van de Linde, A. Löscherger, T. Klein, M. Heidbreder, S. Wolter, M. Heilemann, M. Sauer, *Nat. Protoc.* **2011**, *6*, 991–1009.
- [19] U. Resch-Genger, M. Grabolle, S. Cavaliere-Jaricot, R. Nitschke, T. Nann, *Nat. Methods* **2008**, *5*, 763–775.
- [20] L. Li, G. Wu, G. Yang, J. Peng, J. Zhao, J.-J. Zhu, *Nanoscale* **2013**, *5*, 4015.
- [21] G. Chen, Z. Zhuo, K. Ni, N. Y. Kim, Y. Zhao, Z. Chen, B. Xiang, L. Yang, Q. Zhang, Z. Lee, et al., *Small* **2015**, *11*, 5296–5304.
- [22] F. Li, L. Kou, W. Chen, C. Wu, T. Guo, *NPG Asia Mater.* **2013**, *5*, e60–e60.
- [23] X.-Y. Wang, A. Narita, K. Müllen, *Nat. Rev. Chem.* **2017**, *2*, 0100.
- [24] A. Narita, X.-Y. Wang, X. Feng, K. Müllen, *Chem. Soc. Rev.* **2015**, *44*, 6616–6643.
- [25] Q. Chen, D. Wang, M. Baumgarten, D. Schollmeyer, K. Müllen, A. Narita, *Chem. Asian J.* **2019**, *14*, 1703–1707.
- [26] Z. Ji, E. Dervishi, S. K. Doorn, M. Sykora, *J. Phys. Chem. Lett.* **2019**, *10*, 953–959.
- [27] M. Thakur, A. Mewada, S. Pandey, M. Bhorl, K. Singh, M. Sharon, M. Sharon, *Mater. Sci. Eng. C* **2016**, *67*, 468–477.
- [28] X. T. Zheng, A. Ananthanarayanan, K. Q. Luo, P. Chen, *Small* **2015**, *11*, 1620–1636.
- [29] H. Sun, L. Wu, W. Wei, X. Qu, *Mater. Today* **2013**, *16*, 433–442.
- [30] S. Zhao, J. Lavie, L. Rondin, L. Orcin-Chaix, C. Diederichs, P. Roussignol, Y. Chassagneux, C. Voisin, K. Müllen, A. Narita, et al., *Nat. Commun.* **2018**, *9*, 3470.
- [31] G. M. Paternò, Q. Chen, X.-Y. Wang, J. Liu, S. G. Motti, A. Petrozza, X. Feng, G. Lanzani, K. Müllen, A. Narita, et al., *Angew. Chem. Int. Ed.* **2017**, *56*, 6753–6757; *Angew. Chem.* **2017**, *129*, 6857–6861.
- [32] D. M. Coles, Q. Chen, L. C. Flatten, J. M. Smith, K. Müllen, A. Narita, D. G. Lidzey, *Nano Lett.* **2017**, *17*, 5521–5525.
- [33] V. S. Iyer, K. Yoshimura, V. Enkelmann, R. Epsch, J. P. Rabe, K. Müllen, *Angew. Chem. Int. Ed.* **1998**, *37*, 2696–2699; *Angew. Chem.* **1998**, *110*, 2843–2846.
- [34] J. Vogelsang, C. Steinhauer, C. Forthmann, I. H. Stein, B. Person-Skegro, T. Cordes, P. Tinnefeld, *ChemPhysChem* **2010**, *11*, 2475–2490.
- [35] M. Nirmal, B. O. Dabbousi, M. G. Bawendi, J. J. Macklin, J. K. Trautman, T. D. Harris, L. E. Brus, *Nature* **1996**, *383*, 802–804.
- [36] C. Galland, Y. Ghosh, A. Steinbrück, M. Sykora, J. A. Hollingsworth, V. I. Klimov, H. Htoon, *Nature* **2011**, *479*, 203–207.
- [37] S. Khan, W. Li, N. Karedla, J. Thiart, I. Gregor, A. M. Chizhik, J. Enderlein, C. K. Nandi, A. I. Chizhik, *J. Phys. Chem. Lett.* **2017**, *8*, 5751–5757.
- [38] A. Sakdinawat, D. Attwood, *Nat. Photonics* **2010**, *4*, 840–848.
- [39] F. J. Giessibl, *Rev. Mod. Phys.* **2003**, *75*, 949–983.
- [40] D. B. Williams, C. B. Carter, *Transmission Electron Microscopy*, Springer US, Boston, **1996**, pp. 3–17.

Manuscript received: July 24, 2019

Accepted manuscript online: October 28, 2019

Version of record online: November 26, 2019

Supporting Information

Nanographenes: Ultrastable, Switchable, and Bright Probes for Super-Resolution Microscopy

Xiaomin Liu[†], Shih-Ya Chen[†], Qiang Chen, Xuelin Yao, Márton Gelléri, Sandra Ritz, Sachin Kumar, Christoph Cremer, Katharina Landfester, Klaus Müllen, Sapun H. Parekh, Akimitsu Narita, and Mischa Bonn**

ange_201909220_sm_miscellaneous_information.pdf

Table of Contents

1. Fluorescence and blinking characterization of nanographenes and Alexa 647	S3
2. Light microscopy imaging of crevice 3D structure in a coverslip	S11
3. Topological scan of the crevice structures based on AFM	S13
4. Experimental setup	S14
5. Sample preparation for single molecule blinking	S14
6. Analysis of single molecule blinking data	S15
7. Sample preparation for crevices on a coverslip	S15

SUPPORTING INFORMATION

1. Fluorescence and blinking characterization of nanographenes and Alexa647

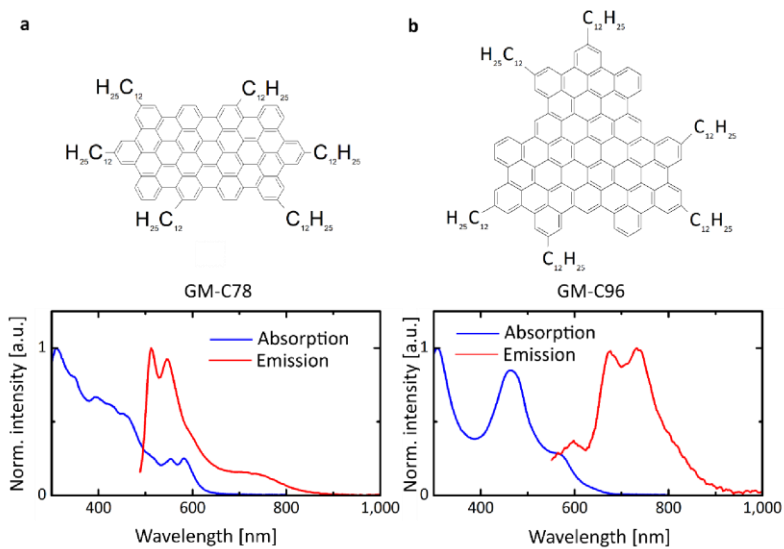
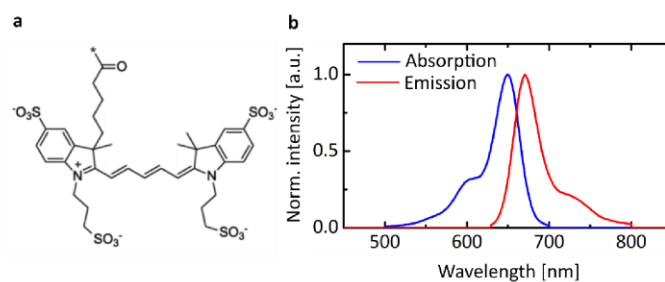
Fig S1. Chemical structure and spectra of nanographene GM-C78 and GM-C96^[1,2].

Fig S2. Chemical structure and spectra of Alexa647.

SUPPORTING INFORMATION

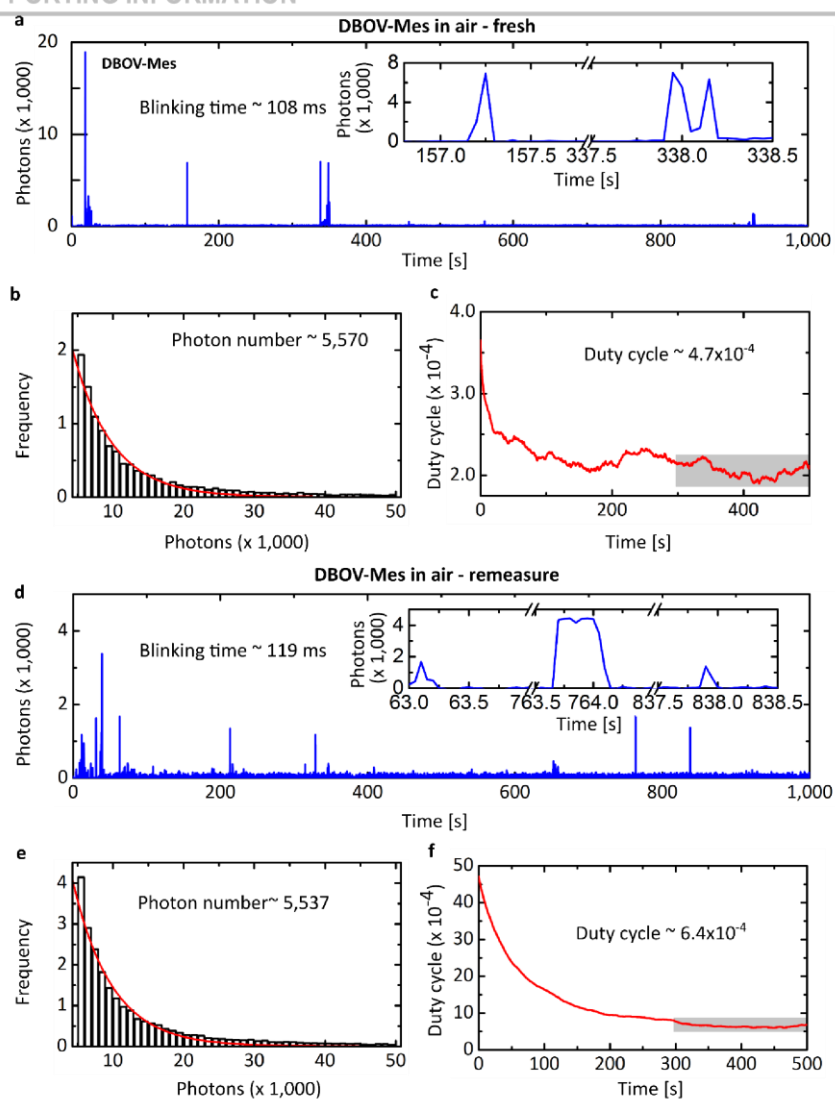


Figure S3. Characterization of DBOV-Mes in air. (a,d) Example of single-molecule fluorescence time trace. Inset: zoom-in on individual switching events. (b,e) Histogram of detected photons per switching event and single exponential fit. (c,f) On-off duty cycle of **DBOV-Mes**. On-off duty cycles were calculated within a window of 200 s (300 – 500 s). (a,b,c) were measured with a fresh sample and (d,e,f) were measured 125 days after sample preparation.

SUPPORTING INFORMATION

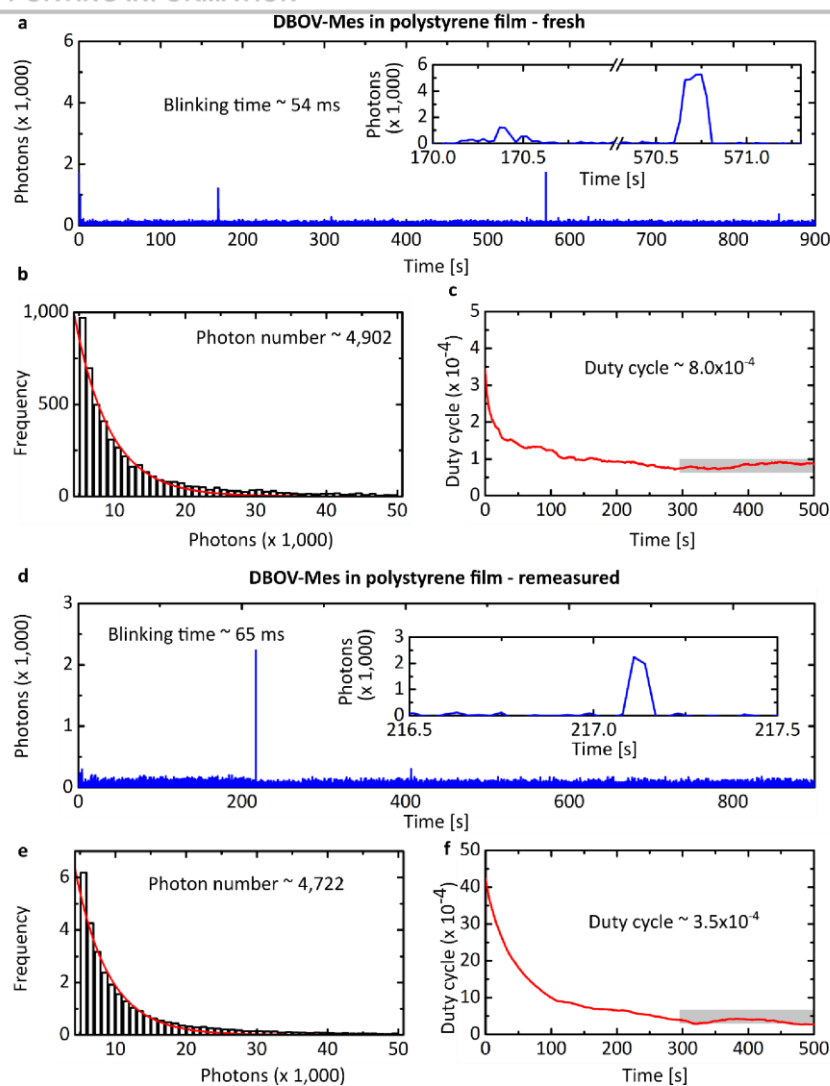


Figure S4. Characterization of DBOV-Mes in polystyrene. (a,d) Example of single-molecule fluorescence time trace. Inset: zoom-in on individual switching events. (b,e) Histogram of detected photons per switching event and single exponential fit. (c,f) On-off duty cycle of **DBOV-Mes**. On-off duty cycles were calculated within a window of 200 s (300 – 500 s). (a,b,c) were measured with a fresh sample and (d,e,f) were measured 57 days after sample preparation.

SUPPORTING INFORMATION

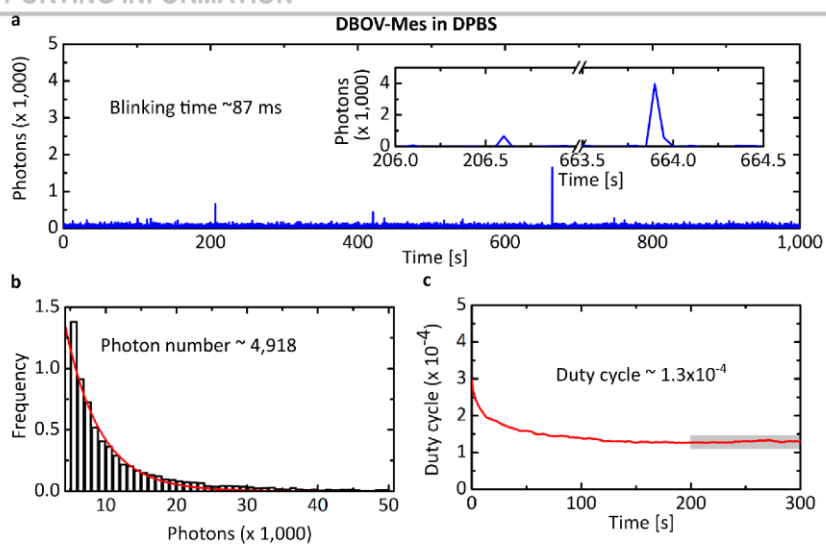


Figure S5. Characterization of DBOV-Mes in DPBS. (a) Example of single-molecule fluorescence time trace. Inset: zoom-in on individual switching events. (b) Histogram of detected photons per switching event and single exponential fit. (c) On-off duty cycle of DBOV-Mes. On-off duty cycles were calculated within a window of 100 s (200 – 300 s).

SUPPORTING INFORMATION

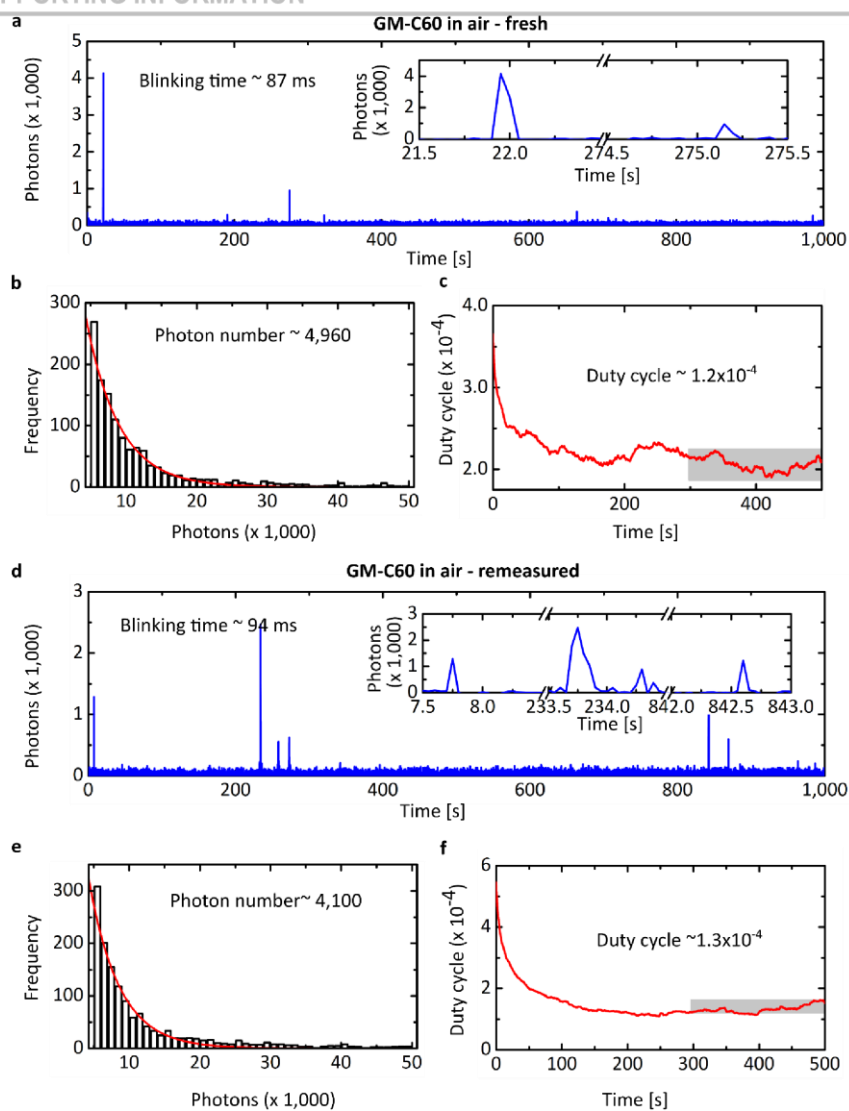


Figure S6. Characterization of GM-C60 in air. (a,d) Example of single-molecule fluorescence time trace. Inset: zoom-in on individual switching events. (b,e) Histogram of detected photons per switching event and single exponential fit. (e,f) On-off duty cycle of GM-C60. On-off duty cycles were calculated within a window of 200 s (300 – 500 s). (a,b,c) were measured with fresh sample and (d,e,f) were measured 21 days after sample preparation.

SUPPORTING INFORMATION

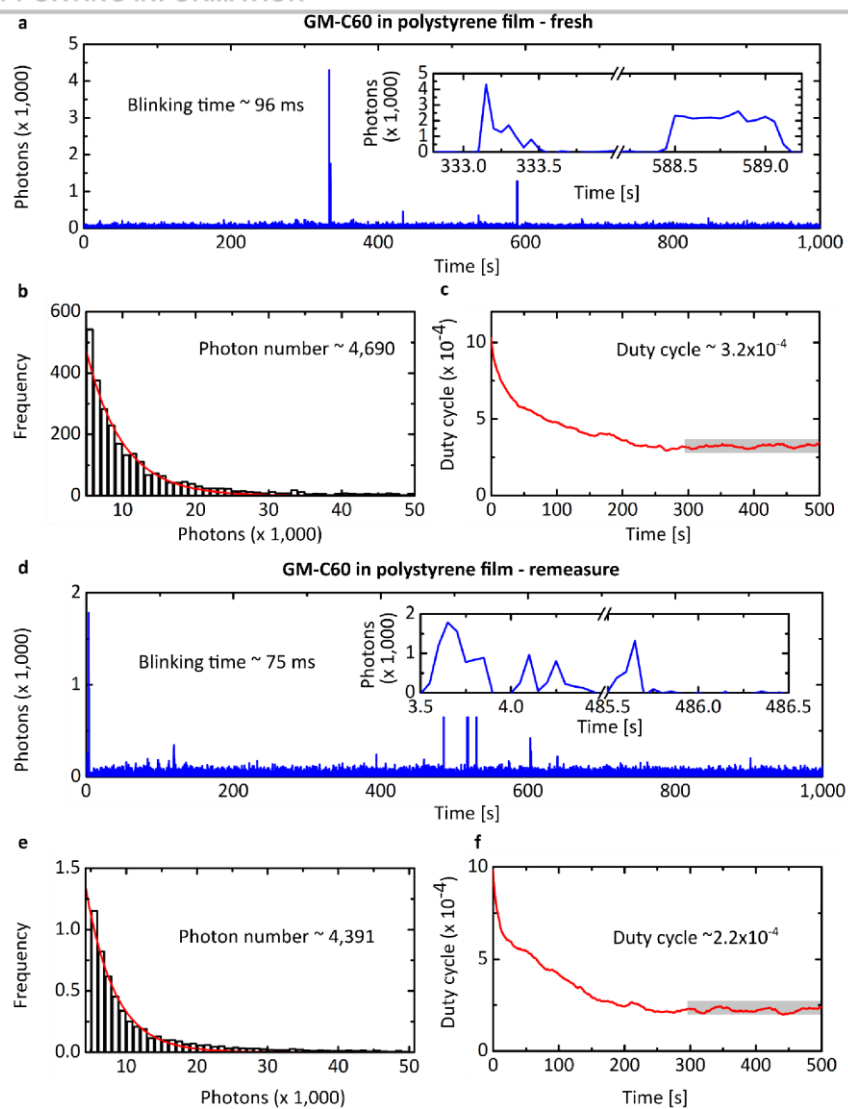


Figure S7. Characterization of GM-C60 embedded in a polystyrene film. (a,d) Example of single-molecule fluorescence time trace. Inset: zoom-in on individual switching events. (b,e) Histogram of detected photons per switching event and single exponential fit. (c,f) On-off duty cycle of GM-C60. On-off duty cycles were calculated within a window of 200 s (300 – 500 s). (a,b,c) were measured with a fresh sample and (d,e,f) were measured 34 days after sample preparation.

SUPPORTING INFORMATION

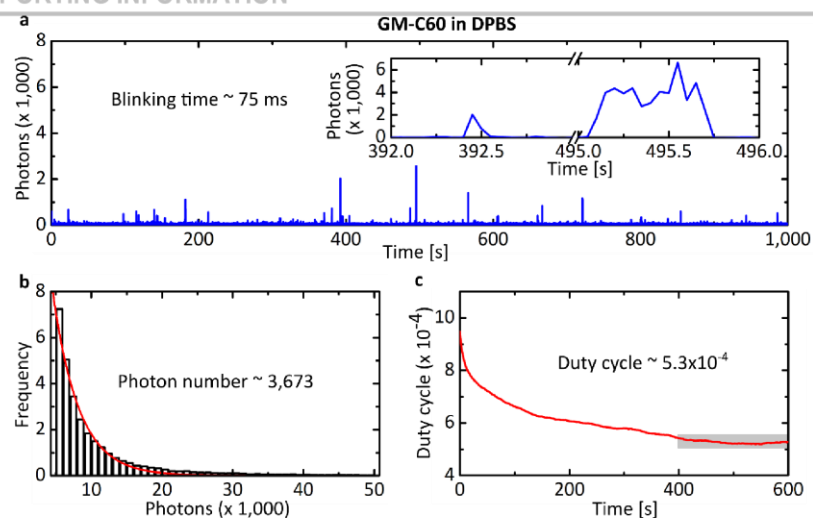


Figure S8. Characterization of GM-C60 in DPBS. (a) Example of single-molecule fluorescence time trace. Inset: zoom-in on individual switching events. (b) Histogram of detected photons per switching event and single exponential fit. (c) On-off duty cycle of **GM-C60**. On-off duty cycles were calculated within a window of 200 s (400 – 600 s).

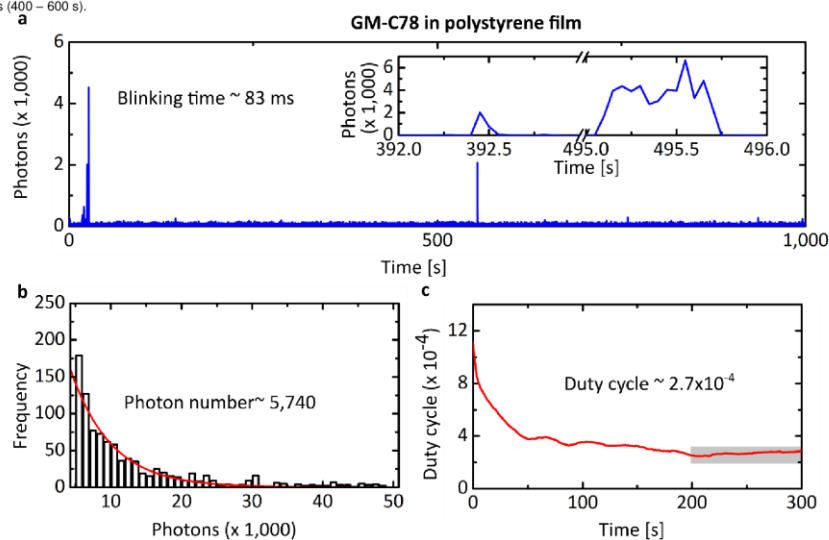


Figure S9. Characterization of GM-C78 embedded in a polystyrene film. (a) Example of single-molecule fluorescence time trace. Inset: zoom-in on individual switching events. (b) Histogram of detected photons per switching event and single exponential fit. (c) On-off duty cycle of **GM-C78**. On-off duty cycles were calculated within a window of 100 s (200 – 300 s).

SUPPORTING INFORMATION

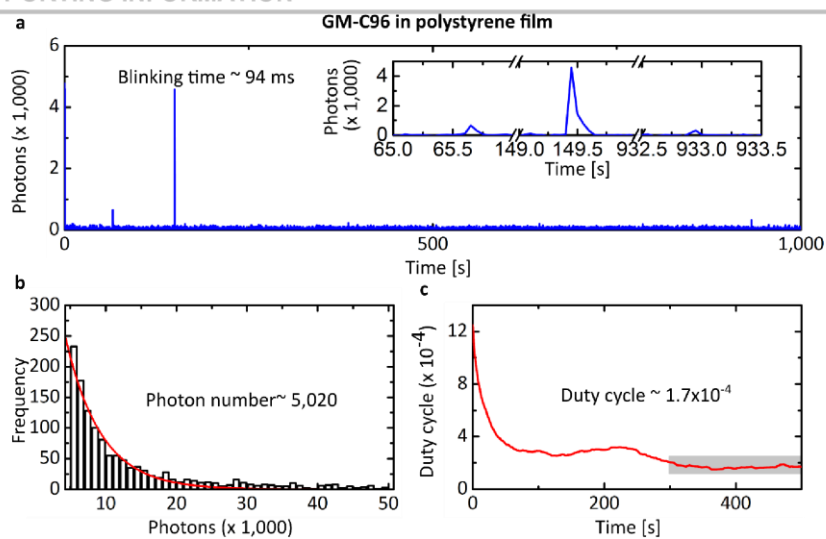


Figure S10. Characterization of GM-C96 in polystyrene. (a) Example of single-molecule fluorescence time trace. Inset: zoom-in on individual switching events. (b) Histogram of detected photons per switching event and single exponential fit. (c) On-off duty cycle of GM-C96. On-off duty cycles were calculated within a window of 200 s (300 – 500 s).

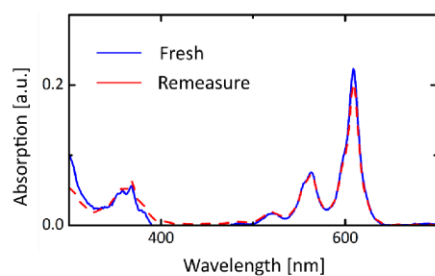


Figure S11. Solution stability of DBOV-Mes in Toluene. The absorption spectra of freshly prepared solution (solid blue line) and after 203 days stored in dark room temperature (dotted red line). The concentration of DBOV-Mes under test is $1 \mu\text{M}$.

SUPPORTING INFORMATION

2. Light microscopy imaging of 3D crevice structures on coverslips

Conventional light microscopy images of the crevices on the treated coverslip based on transmission light microscopy and fluorescence microscopy are shown in Fig. S12 a and b, respectively. The inset shows the ROI for super-resolution imaging and the ROI indicated in a yellow rectangle was used as a comparison as shown in Fig. S15.

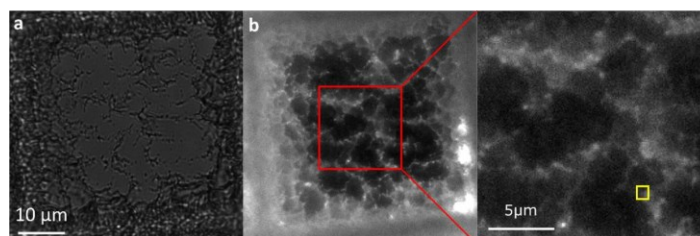


Figure S12. Conventional light microscopy images of "cracks" on the NaOH treated coverslip. (a) The bright-field image and (b) the fluorescence image show irregular "cracks" on the surface of the coverslip. The red rectangle demarcates the region of interest (ROI) for super-resolution imaging. The ROI indicated by a yellow rectangle is compared with the super-resolution image, as shown in Figure S15.

To determine localization of molecules in 3D, a cylindrical lens was inserted in the detection beam path and the point spread function (PSF) was engineered gradually to an elliptical shape. We performed the calibration measurement prior to the super-resolution image acquisition^[3].

A fluorescent bead solution (TetraSpeck 100 nm, ThermoFisher) was prepared by a 1:1000 dilution in dH₂O. A drop of 200 μ l from the diluted beads solution was applied to a μ -Dish 35 mm (ibidi, Germany). After 5 to 6 hours, water evaporated, and the fluorescent beads were immobilized on the bottom of the dish. After applying 500 μ l dH₂O in the dish, the fluorescent beads sample was used for calibration.

The fluorescent bead sample was placed in the SR GSD 3D and stabilized for half an hour. After focusing, the fluorescence beads were visible as diffraction-limited spots. Five fluorescent beads were selected and placed at the center of the field of view. A stack of images with 800 nm (-400nm to +400nm) travel range was defined with 10 nm step size and recorded. The acquired image stack was processed using ThunderSTORM^[4]. By Gaussian fitting of the fluorescent intensity for each fluorescent bead in all frames, the width of the fluorescent beads at the corresponding axial (z) position was obtained. The resulting 3D calibration curves are shown in Fig. S13(a). To select the high precision region, the residuals of the calibration curves were analyzed as shown in Fig. S13(b). The residual of the calibration shows a better precision in the relative axial (z) position between -300 nm and 300 nm; whereas, lower precision is found outside of the -300 nm to +300 nm range. The standard deviation of the calibration curves are 21 nm for the width in the x direction (W_x) and 27 nm for the width in the y direction (W_y).

Fig. S15(b) shows a comparison image of the crevice structure using a conventional microscopy method (wide-field) and the super-resolution method (3D SMLM) at a z-plane of the ROI shown in Fig. S12(b). A separation of 75 nm of the intensity profile can be seen at the transverse plane of the crevice, presenting a higher-resolution image compared with the conventional image.

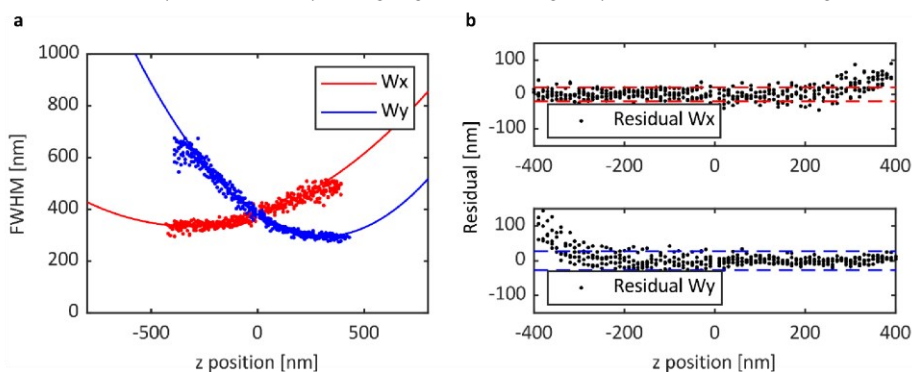


Figure S13. (a) Calibration curves: W_x and W_y represent the FWHM as a function of z obtained from fluorescence beads. (b) The width residuals of W_x and W_y. The ROI indicated in red as shown in Fig. S12 (b) was selected for SMLM imaging. The resulting 3D localizations were analyzed by choosing the high precision

SUPPORTING INFORMATION

region in the axial (z) direction between ± 300 nm. The corresponding histogram is shown in Fig. S14. The localizations were classified into two subsets: the first subset includes the localizations between $z = +300$ nm and -10 nm which are close to the surface of the coverslip shown in the green region; the second subset represents the localizations between $z = -10$ nm and -300 nm detected deeper in the cracks of the coverslips shown in the red region.

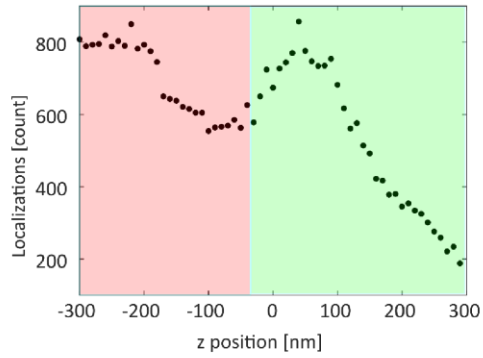


Figure S14. Histogram of localizations in axial (z) position. Detected localizations above the crevice structure are shown in the green region ($z = +300$ nm and -10 nm) and within the crevices shown in the red region ($z = -10$ nm and -300 nm).

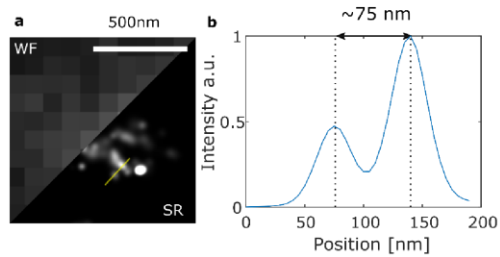


Figure S15. The comparison images of the crevice between the conventional widefield image (WF) and the super-resolution image (SR) at a z -position. (a) Widefield image (WF) and super-resolution image (SR); (b) an intensity profile of the super-resolution image indicated using a yellow line shown in the SR image of (a). The separation of the peak intensities is 75 nm.

SUPPORTING INFORMATION

3. Topological scan of the crack structures based on AFM

Using transmission light, the region of the crevices shown in Fig. S12 was identified and then scanned by the AFM. The resulting AFM image (Fig. S16(a)) shows irregular cracks. After image registration, a good agreement of the crevice structures image by AFM and image by SMLM can be seen in the overlay image shown in Fig. S16(b).

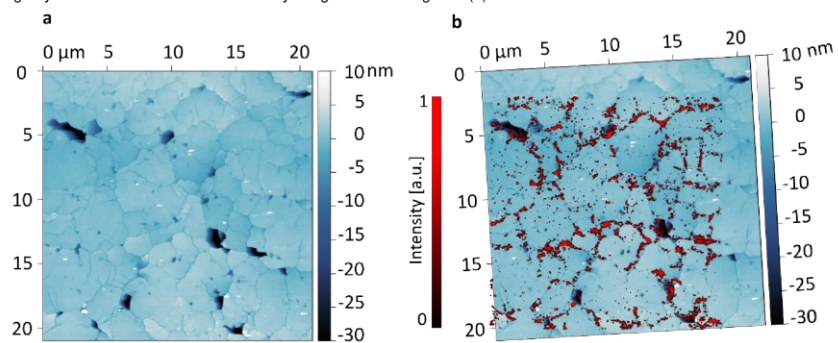


Figure S16. The overlay of high-resolution microscopy images. (a) Topological scan of the crack structures based on AFM. (b) Overlay of AFM and SMLM image after image registration.

SUPPORTING INFORMATION

4. Experimental setup**4.1 Single-molecule localization microscopy**

All light microscopy measurements were performed using the SR GSD microscope (Leica) equipped with four lasers: 488 nm (300 mW), 532 nm (500 mW), 642 nm (500 mW), and 405 nm (30 mW) for fluorescence reactivation. The 405 nm laser was selected as the back-pumping wavelength for fluorescence recovery.

The specification of the filter cubes are: for the 488 nm laser, the excitation filter (483 nm - 493 nm/400 nm - 410 nm), the dichroic beamsplitter (496 nm) and the emission filter (505 nm - 605 nm/449 nm - 451 nm); for the 532 nm laser, the excitation filter (527 nm - 537 nm/400 nm - 410 nm), the dichroic beamsplitter (527 nm - 537 nm/400 nm - 410 nm), the emission filter (550 nm - 650 nm/449 nm - 451 nm); for the 642 nm laser, the excitation filter (637 nm - 647 nm/400 nm - 410 nm), the dichroic beamsplitter (649 nm), the emission filter (660 nm - 760 nm).

The objective lens HCX PL APO 160x 1.43 NA Oil CORR-TIRF was selected for single molecule measurements and super-resolution imaging.

The microscope was equipped with an EMCCD camera (iXonDU-897, Andor). The camera settings were 10 MHz at 14 bit and a pre-amplification of 5.1. For super-resolution imaging, the camera exposure time was set to 50 ms and an EM gain of 100 was used. The pixel size of the image was 100 nm.

4.2 Atomic force microscopy (AFM)

An atomic force microscope (AFM, Dimension FastScan, Bruker) was used with tapping mode in air. A standard V-shaped silicon nitride cantilever with a pyramidal tip from Bruker AFM probes (OPTESA-R3) was mounted. The average height of the tip was 15 μm and the radius of curvature was around 10 nm with a vertex angle of 35° and 18°. The scan rate was 0.5 Hz and the image size was 512 pixels x 512 pixels.

5. Sample preparation for single molecule blinking**5.1 Coverslip cleaning**

For Alexa647, the coverslips (#1.5 high precision) were salinized for 1 h using 0.05% dichlorodimethylsilane in trichloroethylene (while sonicating). The coated coverslips were then firstly washed three times in a sonicating methanol bath and were then rinsed three times with Mili-Q water and finally dried with nitrogen flow.

For nanographenes, the coverslips were cleaned (30 min) in an ultrasonic bath containing soap water. Afterward, they were washed with Mili-Q water and dried under nitrogen flow. The coverslips were cleaned by oxygen-plasma cleaner (250 W, 5 minutes).

5.2 Preparation of Alexa647 single molecule samples

For reference measurements, 6 μl (10 pM) GFP-Booster Alexa Fluor® 647 was applied on a prepared coverslip and covered with a cleaned slide. After 2 hours, the slide was removed and the coverslip was washed extensively for 20 times with Mili-Q water.

The prepared sample with single molecules Alexa647 was embedded in 8 μl imaging buffer. The buffer contained Tris (pH 8.0, 50mM), NaCl (10mM), and an oxygen scavenging system (0.5 mg/ml glucose oxidase (Sigma-Aldrich), 40 $\mu\text{g/ml}$ catalase (Sigma-Aldrich), 10% (w/v) glucose and MEA (10 mM))⁵¹. The sample was sealed with nail polisher on a slide.

5.3 Preparation of nanographene single molecule samples

Nanographene powder was dispersed in toluene and then diluted to 10 μM , 10 nM, 1 nM, 0.1 nM or 10 pM. The solutions were stored at room temperature and were protected from light.

Nanographene samples were then prepared according to their imaging environments.

Nanographenes embedded in polystyrene (PS) film:

Polystyrene (0.08 mg/ml) was mixed 1:1 (v/v) with the nanographene solution. 1 μl (10 pM) of the nanographene-PS solution was spin-coated on the cleaned coverslip. The coverslip was firstly spun at 2,000 rpm for 20 s and then at 4,000 rpm for 40 s. The sample was dried on a hot plate by heating to 90°C for 1 h. The prepared glass coverslip was taped to a slide.

Nanographenes in Dulbecco's Phosphate Buffered Saline (DPBS):

The coverslips (#1.5 high precision) were treated with Trimethoxy(2-phenylethyl)silane in a vacuum desiccator for 1.5 h. 8 μl (10 pM) of the nanographene solution was applied on the prepared coverslip and covered with a cleaned slide. After toluene has volatilized completely, the slide was removed. The coverslip was washed extensively around 20 times with Mili-Q water. 8 μl PBS was added on the coverslip, covered with a cleaned slide and then sealed with nail polish.

Nanographenes in air:

10 μl of the nanographene solution (10 pM) was added on a cleaned coverslip and then covered by a glass slide. After toluene has volatilized completely, the coverslip was taped on a slide.

SUPPORTING INFORMATION

6. Data analysis for single molecule blinking

Fluorescence intensity traces were extracted by first generating a maximum intensity projection of the recorded frames. Fluorescence signals in this projection were localized using the Thunderstorm-plugin in Fiji^{4,6}.

We then calculated the intensity trace for each localization throughout all frames of the raw data as the total background corrected intensity in a 7 x 7 ROI around the localized coordinates. The local background for every localization in every frame was calculated within a 17 x 17 ROI. Pixel values bigger than 5 times the standard deviation within this ROI were excluded from background calculation as they were considered as fluorescence signal. Calculated total intensities within the ROIs were then plotted for every frame.

Calculation of photons per blinking event was done by localization of the nanographenes in every frame of the recorded imaging data. Localizations were then filtered according to the expected width of the signals. Localizations appearing in consecutive frames were then merged. To account for low photon yields that might lead to missed detections, we allowed one dark frame between two detections for merging. As spatial constraint we used a maximum distance of 80 nm, a rather large radius was chosen to allow localizations with low photon counts to be still properly merged.

The histogram of photon counts was then generated and fitted by a monoexponential function. Reported mean values are derived from the fit. Error bars indicate the 95% confidence interval of the fit.

The mean blinking duration was extracted from the same localization data. The mean value was derived from a single exponential fit. Error bars are the 95% confidence intervals of the fit.

The duty cycle is the fraction of time a molecule resides in its fluorescent (on) state and was calculated according to⁵.

7. Sample preparation for crevices on a coverslip

A mild "etching" method was used to induce nanoscale cracks on the coverslip¹⁷.

A borosilicate coverslip (ibidi, gridded glass coverslips grid-50) was firstly cleaned in an ultrasonic bath containing soap water. Afterward, it was cleaned with a UV-Ozone cleaner for 30 min and treated with sodium hydroxide solution 4 M at room temperature for 24 h. Then the coverslip was washed with water, acetone, and toluene and further cleaned by plasma cleaning. The "crack" structures were fluorescent "labeled" by applying a drop of 5 μ l DBOV-Mes (1 nM) onto the coverslip.

References

- [1] M. G. Schwab, A. Narita, Y. Hernandez, T. Balandina, K. S. Mali, S. De Feyter, X. Feng, K. Müllen, *J. Am. Chem. Soc.* **2012**, *134*, 18169–18172.
- [2] Ž. Tomović, M. D. Watson, K. Müllen, *Angew. Chemie Int. Ed.* **2004**, *43*, 755–758.
- [3] B. Huang, W. Wang, M. Bates, X. Zhuang, *Science (80-.)*. **2008**, *319*, 810–813.
- [4] M. Ovesný, P. Křížek, J. Borkovec, Z. Švindrych, G. M. Hagen, *Bioinformatics* **2014**, *30*, 2389–2390.
- [5] G. T. Dempsey, J. C. Vaughan, K. H. Chen, M. Bates, X. Zhuang, *Nat. Methods* **2011**, *8*, 1027–1036.
- [6] J. Schindelin, I. Arganda-Carreras, E. Frise, V. Kaynig, M. Longair, T. Pietzsch, S. Preibisch, C. Rueden, S. Saalfeld, B. Schmid, et al., *Nat. Methods* **2012**, *9*, 676.
- [7] C. C. . DAVISON, *Nature* **1974**, *247*, 103.

Author Contributions

X. Liu, M. Bonn, S. Parekh, C. Cremer conceived the project with suggestion of A. Narita to use nanographenes. X. Liu and S.-Y. Chen performed experiments with help from S. Ritz and Q. Chen. Q. Chen and X. Yao synthesized and provided nanographenes under supervision by K. Müllen and A. Narita. X. Liu, S.-Y. Chen, M. Gelléri and Q. Chen analyzed fluorescence and blinking properties. S. Kumar performed AFM experiments. S.-Y. Chen analyzed SMLM and AFM images. X. Liu and S.-Y. Chen wrote the manuscript with input from all authors.

Selbständigkeitserklärung

Ich erkläre, dass ich die vorliegende Arbeit selbständig und unter Verwendung der angegebenen Hilfsmittel, persönlichen Mitteilungen und Quellen angefertigt habe.

Datum

Ort

Unterschrift

Shih-Ya Chen

Erklärungen

Erklärung zu den Eigenanteilen der Promovendin/des Promovenden sowie der weiteren Doktorandinnen/Doktoranden als Co-Autorinnen/-Autoren an den Publikationen und Zweitpublikationsrechten bei einer kumulativen Dissertation

Für alle in dieser kumulativen Dissertation verwendeten Manuskripte liegen die notwendigen Genehmigungen der Verlage („Reprint permissions“) für die Zweitpublikation vor.

Die Co-Autorinnen/-Autoren der in dieser kumulativen Dissertation verwendeten Manuskripte sind sowohl über die Nutzung, als auch über die oben angegebenen Eigenanteile der weiteren Doktorandinnen/Doktoranden als Co-Autorinnen/-Autoren an den Publikationen und Zweitpublikationsrechten bei einer kumulativen Dissertation informiert und stimmen dem zu.

Die Anteile der Promovendin/des Promovenden sowie der weiteren Doktorandinnen/Doktoranden als Co-Autorinnen/Co-Autoren an den Publikationen und Zweitpublikationsrechten bei einer kumulativen Dissertation sind in der Anlage aufgeführt.

Datum

Ort

Unterschrift

Shih-Ya Chen

Einverständniserklärung des Betreuers

Ich bin mit der Abfassung der Dissertation als publikationsbasierte Dissertation, d.h. kumulativ, einverstanden und bestätige die vorstehenden Angaben.

	Datum	Ort	Unterschrift
Betreuer	_____	_____	_____
Betreuer	_____	_____	_____

Reference

1. A. Jablonski, "Efficiency of anti-stokes fluorescence in dyes," *Nature* **131**, 839–840 (1933).
2. L. J. R., *Principles of Fluorescence Spectroscopy* (Springer US, 2006), Vol. 10.
3. G. G. Stokes, "XXX. On the change of refrangibility of light," *Philos. Trans. R. Soc. London* **142**, 463–562 (1852).
4. "Alexa Fluor 647," <https://www.thermofisher.com/de/de/home/life-science/cell-analysis/fluorophores/alexa-fluor-647.html>.
5. "Chroma Technology," <https://www.chroma.com/spectra-viewer>.
6. E. Betzig, G. H. Patterson, R. Sougrat, O. W. Lindwasser, S. Olenych, J. S. Bonifacino, M. W. Davidson, J. Lippincott-Schwartz, and H. F. Hess, "Imaging intracellular fluorescent proteins at nanometer resolution," *Science* **313**, 1642–1645 (2006).
7. W. E. Moerner and L. Kador, "Optical detection and spectroscopy of single molecules in a solid," *Phys. Rev. Lett.* **62**, 2535–2538 (1989).
8. S. T. Hess, T. P. K. Girirajan, and M. D. Mason, "Ultra-high resolution imaging by fluorescence photoactivation localization microscopy," *Biophys. J.* **91**, 4258–4272 (2006).
9. M. J. Rust, M. Bates, and X. Zhuang, "Sub-diffraction-limit imaging by stochastic optical reconstruction microscopy (STORM)," *Nat. Methods* **3**, 793–796 (2006).
10. M. Gunkel, F. Erdel, K. Rippe, P. Lemmer, R. Kaufmann, C. Hörmann, R. Amberger, and C. Cremer, "Dual color localization microscopy of cellular nanostructures," *Biotechnol. J.* **4**, 927–938 (2009).
11. R. Jungmann, C. Steinhauer, M. Scheible, A. Kuzyk, P. Tinnefeld, and F. C. Simmel, "Single-molecule kinetics and super-resolution microscopy by fluorescence imaging of transient binding on DNA origami," *Nano Lett.* **10**, 4756–4761 (2010).
12. C. Cremer and B. R. Masters, "Resolution enhancement techniques in microscopy," *Eur. Phys. J. H* **38**, 281–344 (2013).
13. P. Tinnefeld, C. Eggeling, and S. W. Hell, *Far-Field Optical Nanoscopy*, Springer Series on Fluorescence (Springer Berlin Heidelberg, 2015), Vol. 14.
14. G. H. Patterson and J. Lippincott-Schwartz, "A photoactivatable GFP for selective photolabeling of proteins and cells," *Science* **297**, 1873–1877 (2002).
15. J. Lippincott-Schwartz and G. H. Patterson, "Photoactivatable fluorescent proteins for diffraction-limited and super-resolution imaging," *Trends Cell Biol.* **19**, 555–565 (2009).
16. R. Ando, H. Hama, M. Yamamoto-hino, H. Mizuno, and A. Miyawaki, "An optical marker based on the UV-induced green- to-red photoconversion of a fluorescent protein," *Proc. Natl. Acad. Sci.* **99**, 12651–12656 (2002).
17. A. . Fallis, *Immunocytochemical Methods and Protocols - 3rd Ed.* (2013), Vol. 53.
18. M. J. Rust, M. Bates, and X. Zhuang, "Sub-diffraction-limit imaging by stochastic optical reconstruction microscopy (STORM)," *Nat. Methods* **3**, 793–795 (2006).
19. S. van de Linde, A. Löschberger, T. Klein, M. Heidbreder, S. Wolter, M. Heilemann, and M. Sauer, "Direct stochastic optical reconstruction microscopy with standard fluorescent probes," *Nat. Protoc.* **6**, 991–1009 (2011).
20. J. Vogelsang, R. Kasper, C. Steinhauer, B. Person, M. Heilemann, M. Sauer, and P. Tinnefeld, "A reducing and oxidizing system minimizes photobleaching and blinking

- of fluorescent dyes," *Angew. Chemie Int. Ed.* **47**, 5465–5469 (2008).
21. M. Heilemann, E. Margeat, R. Kasper, M. Sauer, and P. Tinnefeld, "Carbocyanine dyes as efficient reversible single-molecule optical switch," *J. Am. Chem. Soc.* **127**, 3801–3806 (2005).
 22. M. Heilemann, S. van de Linde, M. Schüttpelz, R. Kasper, B. Seefeldt, A. Mukherjee, P. Tinnefeld, and M. Sauer, "Subdiffraction-resolution fluorescence imaging with conventional fluorescent probes," *Angew. Chemie Int. Ed.* **47**, 6172–6176 (2008).
 23. J. R. Lakowicz and G. Weber, "Quenching of fluorescence by oxygen. A probe for structural fluctuations in macromolecules," *Biochemistry* **12**, 4161–4170 (1973).
 24. S. van de Linde, I. Krstić, T. Prisner, S. Doose, M. Heilemann, and M. Sauer, "Photoinduced formation of reversible dye radicals and their impact on super-resolution imaging," *Photochem. Photobiol. Sci.* **10**, 499–506 (2011).
 25. X. Shi, J. Lim, and T. Ha, "Acidification of the oxygen scavenging system in single-molecule fluorescence studies: In situ sensing with a ratiometric dual-emission probe," *Anal. Chem.* **82**, 6132–6138 (2010).
 26. M. Swoboda, J. Henig, H.-M. Cheng, D. Brugger, D. Haltrich, N. Plumeré, and M. Schlierf, "Enzymatic oxygen scavenging for photostability without pH drop in single-molecule experiments," *ACS Nano* **6**, 6364–6369 (2012).
 27. G. T. Dempsey, J. C. Vaughan, K. H. Chen, M. Bates, and X. Zhuang, "Evaluation of fluorophores for optimal performance in localization-based super-resolution imaging," *Nat. Methods* **8**, 1027–1036 (2011).
 28. L. Nahidiazar, A. V. Agronskaia, J. Broertjes, B. Den Van Broek, and K. Jalink, "Optimizing imaging conditions for demanding multi-color super resolution localization microscopy," *PLoS One* **11**, 1–18 (2016).
 29. N. Olivier, D. Keller, V. S. Rajan, P. Gönczy, and S. Manley, "Simple buffers for 3D STORM microscopy," *Biomed. Opt. Express* **4**, 885 (2013).
 30. P. Lemmer, M. Gunkel, D. Baddeley, R. Kaufmann, A. Urich, Y. Weiland, J. Reymann, P. Müller, M. Hausmann, and C. Cremer, "SPDM: light microscopy with single-molecule resolution at the nanoscale," *Appl. Phys. B* **93**, 1–12 (2008).
 31. J. Watson and F. Crick, "Molecular structure of deoxypentose," *Nature* **171**, 738–740 (1953).
 32. J. M. Berg, J. L. Tymoczko, and L. Stryer, *Biochemistry* (W.H. Freeman and Company, 2012).
 33. A. T. Annunziato, "DNA packaging: nucleosomes and chromatin," *Nat. Educ.* **1**, (2008).
 34. A. Németh and G. Längst, "Chromatin higher order structure : Opening up chromatin for transcription," *Briefings Funct. Genomics Proteomics* **2**, 334–343 (2004).
 35. D. E. Olins and A. L. Olins, "Chromatin history: our view from the bridge," *Nat. Rev. Mol. Cell Biol.* **4**, 809–814 (2003).
 36. H. Tanabe, F. A. Habermann, I. Solovei, M. Cremer, and T. Cremer, "Non-random radial arrangements of interphase chromosome territories: Evolutionary considerations and functional implications," *Mutat. Res.* **504**, 37–45 (2002).
 37. H. Albiez, M. Cremer, C. Tiberi, L. Vecchio, L. Schermelleh, S. Dittrich, K. Küpper, B. Joffe, T. Thormeyer, J. von Hase, S. Yang, K. Rohr, H. Leonhardt, I. Solovei, C. Cremer, S. Fakan, and T. Cremer, "Chromatin domains and the interchromatin compartment form structurally defined and functionally interacting nuclear networks," *Chromosom. Res.* **14**, 707–733 (2006).
 38. B. Alberts, *Molecular Biology of the Cell* (2002).

39. T. Cremer and C. Cremer, "Chromosome territories, nuclear architecture and gene regulation in mammalian cells," *Nat. Rev. Genet.* **2**, 292–301 (2001).
40. T. Cremer, M. Cremer, B. Hübner, H. Strickfaden, D. Smeets, J. Popken, M. Sterr, Y. Markaki, K. Rippe, and C. Cremer, "The 4D nucleome: Evidence for a dynamic nuclear landscape based on co-aligned active and inactive nuclear compartments," *FEBS Lett.* **589**, 2931–2943 (2015).
41. K. J. Meaburn and T. Misteli, "Chromosome territories," *Nature* **445**, 379–381 (2007).
42. P. N. Lewis, W. J. Lukiw, U. Boni, and D. R. Crapper McLachlan, "Changes in chromatin structure associated with Alzheimer's disease," *J. Neurochem.* **37**, 1193–1202 (1981).
43. A. J. Parry and M. Narita, "Old cells, new tricks: chromatin structure in senescence," *Mamm. Genome* **27**, 320–331 (2016).
44. I. Sur and J. Taipale, "The role of enhancers in cancer," *Nat. Rev. Cancer* **16**, 483–493 (2016).
45. I. Kirmes, A. Szczurek, K. Prakash, I. Charapitsa, C. Heiser, M. Musheev, F. Schock, K. Fornalczyk, D. Ma, U. Birk, C. Cremer, and G. Reid, "A transient ischemic environment induces reversible compaction of chromatin," *Genome Biol.* **16**, 1–19 (2015).
46. I. Johnson and M. T. Z. Spence, *The Molecular Probes Handbook*, 11th ed. (Life Technologies Corporation, 2010).
47. B. Chazotte, "Labeling nuclear DNA using DAPI," *Cold Spring Harb Protoc* 80–83 (2011).
48. B. Chazotte, "Labeling nuclear DNA with Hoechst 33342," *Cold Spring Harb Protoc* 83–86 (2011).
49. D. H. Paik and T. T. Perkins, "Dynamics and multiple stable binding modes of DNA intercalators revealed by single-molecule force spectroscopy," *Angew. Chemie Int. Ed.* **51**, 1811–1815 (2012).
50. C. Carlsson, A. Larsson, M. Jonsson, B. Albinsson, and B. Norden, "Optical and photophysical properties of the oxazole yellow DNA probes YO and YOYO," *J. Phys. Chem.* **98**, 10313–10321 (1994).
51. A. Larsson, C. Carlsson, M. Jonsson, and B. Albinsson, "Characterization of the binding of the fluorescent dyes YO and YOYO to DNA by polarized light spectroscopy," *J. Am. Chem. Soc.* **116**, 8459–8465 (1994).
52. Thermo Fisher, *The Molecular Probes Handbook: A Guide to Fluorescent Probes and Labeling Technologie* (2010).
53. C. T. Wittwer, L. Zhou, V. E. Dujols, J. A. Holden, and C. Willmore-Payne, "WO2006121423A2," (2006).
54. X. Yan, R. C. Habbersett, J. M. Cordek, J. P. Nolan, T. M. Yoshida, J. H. Jett, and B. L. Marrone, "Development of a mechanism-based, DNA staining protocol using SYTOX Orange nucleic acid stain and DNA fragment sizing flow cytometry," *Anal. Biochem.* **286**, 138–148 (2000).
55. A. T. Szczurek, K. Prakash, H.-K. Lee, D. J. Żurek-Biesiada, G. Best, M. Hagmann, J. W. Dobrucki, C. Cremer, and U. Birk, "Single molecule localization microscopy of the distribution of chromatin using Hoechst and DAPI fluorescent probes," *Nucleus* **5**, 331–340 (2014).
56. C. Flors, "DNA and chromatin imaging with super-resolution fluorescence microscopy based on single-molecule localization," *Biopolymers* **95**, 290–297 (2011).
57. I. Schoen, J. Ries, E. Klotzsch, H. Ewers, and V. Vogel, "Binding-activated localization

- microscopy of DNA structures," *Nano Lett.* **11**, 4008–4011 (2011).
58. A. Szczurek, L. Klewes, J. Xing, A. Gourram, U. Birk, H. Knecht, J. W. Dobrucki, S. Mai, and C. Cremer, "Imaging chromatin nanostructure with binding-activated localization microscopy based on DNA structure fluctuations," *Nucleic Acids Res.* **45**, (2017).
 59. V. L. Singer, L. J. Jones, S. T. Yue, and R. P. Haugland, "Characterization of PicoGreen reagent and development of a fluorescence-based solution assay for double-stranded DNA quantitation," *Anal. Biochem.* **249**, 228–238 (1997).
 60. G. Cosa, K.-S. Focsaneanu, J. R. N. McLean, J. P. McNamee, and J. C. Scaiano, "Photophysical properties of fluorescent DNA-dyes bound to single- and double-stranded DNA in aqueous buffered solution," *Photochem. Photobiol.* **73**, 585 (2001).
 61. X. Yan, R. C. Habbersett, T. M. Yoshida, J. P. Nolan, J. H. Jett, and B. L. Marrone, "Probing the kinetics of SYTOX Orange stain binding to double-stranded DNA with implications for DNA analysis," *Anal. Chem.* **77**, 3554–3562 (2005).
 62. A. Szczurek, U. Birk, H. Knecht, J. Dobrucki, S. Mai, and C. Cremer, "Super-resolution binding activated localization microscopy through reversible change of dna conformation," *Nucleus* **9**, 182–189 (2018).
 63. A. Ernst, "Beiträge zur Theorie des Mikroskops und der mikroskopischen Wahrnehmung," *Arch. für Mikroskopische Anat.* **9**, 418–440 (1873).
 64. M. Born, E. Wolf, A. B. Bhatia, P. C. Clemmow, D. Gabor, A. R. Stokes, A. M. Taylor, P. A. Wayman, and W. L. Wilcock, *Principles of Optics* (Cambridge University Press, 1999).
 65. H. Kirshner, F. Aguet, D. Sage, and M. Unser, "3-D PSF fitting for fluorescence microscopy: Implementation and localization application," *J. Microsc.* **249**, 13–25 (2013).
 66. Lord Rayleigh, "XX. On the equilibrium of liquid conducting masses charged with electricity," *London, Edinburgh, Dublin Philos. Mag. J. Sci.* **14**, 184–186 (1882).
 67. R. E. Thompson, D. R. Larson, and W. W. Webb, "Precise nanometer localization analysis for individual fluorescent probes," *Biophys. J.* **82**, 2775–2783 (2002).
 68. N. Chenouard, I. Smal, F. de Chaumont, M. Maška, I. F. Sbalzarini, Y. Gong, J. Cardinale, C. Carthel, S. Coraluppi, M. Winter, A. R. Cohen, W. J. Godinez, K. Rohr, Y. Kalaidzidis, L. Liang, J. Duncan, H. Shen, Y. Xu, K. E. G. Magnusson, J. Jaldén, H. M. Blau, P. Paul-Gilloteaux, P. Roudot, C. Kervrann, F. Waharte, J.-Y. Tinevez, S. L. Shorte, J. Willemsse, K. Celler, G. P. van Wezel, H.-W. Dan, Y.-S. Tsai, C. O. de Solórzano, J.-C. Olivo-Marin, and E. Meijering, "Objective comparison of particle tracking methods," *Nat. Methods* **11**, 281–289 (2014).
 69. F. Dumas, N. Destainville, C. Millot, A. Lopez, D. Dean, and L. Salomé, "Confined diffusion without fences of a g-protein-coupled receptor as revealed by single particle tracking," *Biophys. J.* **84**, 356–366 (2003).
 70. C. S. Smith, N. Joseph, B. Rieger, and K. A. Lidke, "Fast, single-molecule localization that achieves theoretically minimum uncertainty," *Nat. Methods* **7**, 373–375 (2010).
 71. K. I. Mortensen, L. S. Churchman, J. A. Spudich, and H. Flyvbjerg, "Optimized localization analysis for single-molecule tracking and super-resolution microscopy," *Nat. Methods* **7**, 377–381 (2010).
 72. G. T. Dempsey, J. C. Vaughan, K. H. Chen, M. Bates, and X. Zhuang, "Evaluation of fluorophores for optimal performance in localization-based super-resolution imaging," *Nat. Methods* **8**, 1027–1040 (2011).
 73. E. Betzig, "Proposed method for molecular optical imaging," *Opt. Lett.* **20**, 237 (1995).
 74. C. Cremer, P. Edelmann, H. Bornfleth, G. Kreth, H. Muench, H. Luz, and M.

- Hausmann, "Principles of spectral precision distance confocal microscopy for the analysis of molecular nuclear structure," in *Handbook of Computer Vision and Applications* (Academic Press San Diego, 1999), Vol. 3, pp. 839–858.
75. J. Fölling, M. Bossi, H. Bock, R. Medda, C. A. Wurm, B. Hein, S. Jakobs, C. Eggeling, and S. W. Hell, "Fluorescence nanoscopy by ground-state depletion and single-molecule return," *Nat. Methods* **5**, 943–945 (2008).
 76. N. C. Shaner, M. Z. Lin, M. R. McKeown, P. A. Steinbach, K. L. Hazelwood, M. W. Davidson, and R. Y. Tsien, "Improving the photostability of bright monomeric orange and red fluorescent proteins," *Nat. Methods* **5**, 545–551 (2008).
 77. C. E. Shannon, "Communication in the presence of noise," *Proc. IRE* **37**, 10–21 (1949).
 78. T. Holm, T. Klein, A. Löschberger, T. Klamp, G. Wiebusch, S. van de Linde, and M. Sauer, "A blueprint for cost-efficient localization microscopy," *ChemPhysChem* **15**, 651–654 (2014).
 79. K. M. Douglass, C. Sieben, A. Archetti, A. Lambert, and S. Manley, "Super-resolution imaging of multiple cells by optimized flat-field epi-illumination," *Nat. Photonics* **10**, 705–708 (2016).
 80. H. Kirshner, D. Sage, and M. Unser, "3D PSF models for fluorescence microscopy in ImageJ," in *Proceedings of the Twelfth International Conference on Methods and Applications of Fluorescence Spectroscopy* (2011), p. 154.
 81. B. Richards and E. Wolf, "Electromagnetic diffraction in optical systems, II. Structure of the image field in an aplanatic system," *Proc. R. Soc. London. Ser. A. Math. Phys. Sci.* **253**, 358–379 (1959).
 82. B. Huang, W. Wang, M. Bates, and X. Zhuang, "Three-dimensional super-resolution imaging by stochastic optical reconstruction microscopy," *Science* **319**, 810–813 (2008).
 83. H. P. Kao and A. S. Verkman, "Tracking of single fluorescent particles in three dimensions: use of cylindrical optics to encode particle position," *Biophys. J.* **67**, 1291–1300 (1994).
 84. S. R. P. Pavani, M. A. Thompson, J. S. Biteen, S. J. Lord, N. Liu, R. J. Twieg, R. Piestun, and W. E. Moerner, "Three-dimensional, single-molecule fluorescence imaging beyond the diffraction limit by using a double-helix point spread function," *Proc. Natl. Acad. Sci.* **106**, 2995–2999 (2009).
 85. M. J. Mlodzianoski, M. F. Juette, G. L. Beane, and J. Bewersdorf, "Experimental characterization of 3D localization techniques for particle-tracking and super-resolution microscopy," *Opt. Express* **17**, 8264 (2009).
 86. A. Aristov, B. Lelandais, E. Rensen, and C. Zimmer, "ZOLA-3D allows flexible 3D localization microscopy over an adjustable axial range," *Nat. Commun.* **9**, 2409 (2018).
 87. M. Ovesný, P. Křížek, J. Borkovec, Z. Švindrych, and G. M. Hagen, "ThunderSTORM: a comprehensive ImageJ plug-in for PALM and STORM data analysis and super-resolution imaging," *Bioinformatics* **30**, 2389–2390 (2014).
 88. J. W. Goodman, "Some fundamental properties of speckle*," *J. Opt. Soc. Am.* **66**, 1145 (1976).
 89. J. B. Pawley, *Handbook of Biological Confocal Microscopy* (Springer, 2006).
 90. R. A. Meyer and A. Brunsting, "Light scattering from nucleated biological cells," *Biophys. J.* **15**, 191–203 (1975).
 91. M. Guizar-Sicairos, S. T. Thurman, and J. R. Fienup, "Efficient subpixel image registration algorithms," *Opt. Lett.* **33**, 156–158 (2008).
 92. V. D., "Microdisplays: liquid crystal on silicon," *Nat. Photonics* **4**, 752–754 (2010).
 93. Z. Zhang, Z. You, and D. Chu, "Fundamentals of phase-only liquid crystal on silicon

- (LCOS) devices," *Light Sci. Appl.* **3**, e213–e213 (2014).
94. B. E. A. Saleh and M. C. Teich, *Fundamentals of Photonics* (1991), Vol. 5.
 95. C. Maurer, A. Jesacher, S. Bernet, and M. Ritsch-Marte, "What spatial light modulators can do for optical microscopy," *Laser Photonics Rev.* **5**, 81–101 (2011).
 96. R. W. Gerchberg and W. O. Saxton, "A practical algorithm for the determination of phase from image and diffraction plane pictures," *Optik (Stuttg.)* **35**, 237–246 (1972).
 97. Y. Takaki and M. Yokouchi, "Speckle-free and grayscale hologram reconstruction using time-multiplexing technique," *Opt. Express* **19**, 7567 (2011).
 98. W.-F. Hsu and C.-F. Yeh, "Speckle suppression in holographic projection displays using temporal integration of speckle images from diffractive optical elements," *Appl. Opt.* **50**, H50–H55 (2011).
 99. K. M. Douglass, C. Sieben, A. Archetti, A. Lambert, and S. Manley, "Super-resolution imaging of multiple cells by optimized flat-field epi-illumination," *Nat. Photonics* **10**, 705–708 (2016).
 100. S. L. Wolfe, *Molecular and Cellular Biology* (1993).
 101. M. Ester, H. Kriegel, J. Sander, and X. Xu, "A density-based algorithm for discovering clusters in large spatial databases with noise," in *2nd International Conference on Knowledge Discovery and Data Mining* (AAAI Press, 1996), pp. 226–231.
 102. H. D. Ou, S. Phan, T. J. Deerinck, A. Thor, M. H. Ellisman, and C. C. O’Shea, "ChromEMT: Visualizing 3D chromatin structure and compaction in interphase and mitotic cells," *Science (80-.)* **357**, (2017).
 103. K. Fang, X. Chen, X. Li, Y. Shen, J. Sun, D. M. Czajkowsky, and Z. Shao, "Super-resolution imaging of individual human subchromosomal regions in situ reveals nanoscopic building blocks of higher-order structure," *ACS Nano* **12**, 4909–4918 (2018).
 104. M. Cremer and T. Cremer, "Nuclear compartmentalization, dynamics, and function of regulatory DNA sequences," *Genes Chromosom. Cancer* **58**, 427–436 (2019).
 105. J. Otterstrom, A. Castells-garcia, C. Vicario, P. A. Gomez-garcia, M. P. Cosma, and M. Lakadamyali, "Super-resolution microscopy reveals how histone tail acetylation affects DNA compaction within nucleosomes in vivo," *Nucleic Acids Res.* **47**, 8470–8484 (2019).
 106. P. Almada, P. M. Pereira, S. Culley, G. Caillol, F. Boroni-Rueda, C. L. Dix, G. Charras, B. Baum, R. F. Laine, C. Letierrier, and R. Henriques, "Automating multimodal microscopy with NanoJ- Fluidics," *Nat. Commun.* **10**, (2019).
 107. A. K. Geim and K. S. Novoselov, "The rise of graphene," *Nat. Mater.* **6**, 183–191 (2007).
 108. A. Fredrik, "The nobel prize in physics 2010," *The royal swedish academy of sciences* (2010).
 109. L. Li, G. Wu, G. Yang, J. Peng, J. Zhao, and J. J. Zhu, "Focusing on luminescent graphene quantum dots: current status and future perspectives," *Nanoscale* **5**, 4015–4039 (2013).
 110. X. T. Zheng, A. Ananthanarayanan, K. Q. Luo, and P. Chen, "Glowing graphene quantum dots and carbon dots: properties, syntheses, and biological applications," *Small* **11**, 1620–1636 (2015).
 111. J. Shen, Y. Zhu, X. Yang, and C. Li, "Graphene quantum dots: Emergent nanolights for bioimaging, sensors, catalysis and photovoltaic devices," *Chem. Commun.* **48**, 3686–3699 (2012).
 112. Z. Ji, E. Dervishi, S. K. Doorn, and M. Sykora, "Size-dependent electronic properties

- of uniform ensembles of strongly confined graphene quantum dots," *J. Phys. Chem. Lett.* **10**, 953–959 (2019).
113. D. M. Coles, Q. Chen, L. C. Flatten, J. M. Smith, K. Müllen, A. Narita, and D. G. Lidzey, "Strong exciton-photon coupling in a nanographene filled microcavity," *Nano Lett.* **17**, 5521–5525 (2017).
 114. V. S. Iyer, K. Yoshimura, V. Enkelmann, R. Epsch, J. P. Rabe, and K. Müllen, "A soluble C60 graphite segment," *Angew. Chem. Int. Ed* **37**, 2696–2699 (1998).
 115. Q. Chen, S. Thoms, S. Stöttinger, D. Schollmeyer, K. Müllen, A. Narita, and T. Basché, "Dibenzo[hi,st]ovalene as highly luminescent nanographene: efficient synthesis via photochemical cyclodehydroiodination, optoelectronic properties, and single-molecule spectroscopy," *J. Am. Chem. Soc.* **141**, 16439–16449 (2019).
 116. H. Sun, L. Wu, W. Wei, and X. Qu, "Recent advances in graphene quantum dots for sensing," *Mater. Today* **16**, 433–442 (2013).
 117. M. Thakur, A. Mewada, S. Pandey, M. Bhoori, K. Singh, M. Sharon, and M. Sharon, "Milk-derived multi-fluorescent graphene quantum dot-based cancer theranostic system," *Mater. Sci. Eng. C* **67**, 468–477 (2016).
 118. M. G. Schwab, A. Narita, Y. Hernandez, T. Balandina, K. S. Mali, S. De Feyter, X. Feng, and K. Müllen, "Structurally defined graphene nanoribbons with high lateral extension," *J. Am. Chem. Soc.* **134**, 18169–18172 (2012).
 119. Ž. Tomović, M. D. Watson, and K. Müllen, "Superphenalene-based columnar liquid crystals," *Angew. Chemie Int. Ed.* **43**, 755–758 (2004).
 120. A. M. Bittel, A. M. Davis, L. Wang, M. A. Nederlof, J. O. Escobedo, R. M. Strongin, and S. L. Gibbs, "Varied length Stokes shift BODIPY-based fluorophores for multicolor microscopy," *Sci. Rep.* **8**, 1–12 (2018).
 121. F. Balzarotti, Y. Eilers, K. C. Gwosch, A. H. Gynnå, V. Westphal, F. D. Stefani, J. Elf, and S. W. Hell, "With minimal photon fluxes," *Science* **355**, 606–612 (2017).
 122. G. M. Paternò, Q. Chen, X.-Y. Wang, J. Liu, S. G. Motti, A. Petrozza, X. Feng, G. Lanzani, K. Müllen, A. Narita, and F. Scotognella, "Synthesis of Dibenzo[hi,st]ovalene and its amplified spontaneous emission in a polystyrene matrix," *Angew. Chemie Int. Ed.* **56**, 6753–6757 (2017).
 123. Q. Chen, D. Wang, M. Baumgarten, D. Schollmeyer, K. Müllen, and A. Narita, "Regioselective bromination and functionalization of Dibenzo[hi,st]ovalene as highly luminescent nanographene with zigzag edges," *Chem. Asian J.* **14**, 1703–1707 (2019).